

<https://doi.org/10.15388/vu.thesis.525>

<https://orcid.org/0000-0003-4894-3414>

VILNIUS UNIVERSITY
CENTER FOR PHYSICAL SCIENCES AND TECHNOLOGY
UAB FEMTIKA

Greta Merkininkaitė

Additive Manufacturing of Inorganic 3D Nanostructures by Combining Laser Lithography and Pyrolysis

DOCTORAL DISSERTATION

Technological Sciences
Materials Engineering (T 008)

VILNIUS 2023

The dissertation was prepared between 2018 and 2023 at Vilnius University in cooperation with UAB Femtika. The research was funded by grant No. D.2018-0698 from the Research Council of Lithuania.

Academic supervisor – Prof. Dr. Simas Šakirzanovas (Vilnius University, Natural Sciences, Chemistry, N 003).

Academic consultant – Prof. Dr. Mangirdas Malinauskas (Vilnius University, Technological Sciences, Materials Engineering, T 008).

This doctoral dissertation will be defended in a public/closed meeting of the Dissertation Defence Panel: Dissertation Defence Panel:

Chairman – Dr. Genrik Mordas (Center for Physical Sciences and Technology, Technological Sciences, Materials Engineering – T 008).

Members:

Prof. Dr. Rimantas Raudonis (Vilnius University, Natural sciences, Chemistry – N 003),

Assoc. Prof. Dr. Jolanta Rousseau (Artois University, Technological Sciences, Materials Engineering – T 008),

Prof. Dr. Tomas Tamulevičius (Kaunas University of Technology, Technological Sciences, Materials Engineering – T 008),

Assoc. Prof. Dr. Linas Vilčiauskas (Vilnius University, Natural sciences, Chemistry – N 003),

The dissertation shall be defended at a public meeting of the Dissertation Defence Panel at 2 p.m. on 29th September 2023 in Kazys Daukšas auditorium (223 aud.) of the Faculty of Chemistry and Geosciences, Vilnius University.

Address: Naugarduko street, 24, LT-03225, Vilnius, Lithuania
Tel. +37052193105; e-mail: info@chgf.vu.lt

The text of this dissertation can be accessed at the libraries of Vilnius University and Center for Physical Sciences and Technology, as well as on the website of Vilnius University:
www.vu.lt/lt/naujienos/ivykiu-kalendorius.

<https://doi.org/10.15388/vu.thesis.525>

<https://orcid.org/0000-0003-4894-3414>

VILNIAUS UNIVERSITETAS
FIZINIŲ IR TECHNOLOGIJOS MOKSLŲ CENTRAS
UAB FEMTIKA

Greta Merkininkaitė

Neorganinių 3D nanodarinių adityvus formavimas jungiant lazerinę litografiją ir pirolizę

DAKTARO DISERTACIJA

Technologijos mokslai
Medžiagų inžinerija (T 008)

VILNIUS 2023

Disertacija rengta 2018 – 2023 metais Vilniaus universitete ir UAB Fentika įmonėje.

Mokslinius tyrimus rėmė Lietuvos mokslo taryba (Nr. D.2018-0698).

Mokslinis vadovas – prof. dr. Simas Šakirzanovas (Vilniaus universitetas, gamtos mokslai, chemija – N 003).

Mokslinis konsultantas – prof. dr. Mangirdas Malinauskas (Vilniaus universitetas, technologijos mokslai, medžiagų inžinerija – T 008).

Gynimo taryba:

Pirmininkas – Dr. Henrik Mordas (Fizinių ir technologijos mokslų centras, technologijos mokslai, medžiagų inžinerija – T 008).

Nariai:

prof. dr. Rimantas Raudonis (Vilniaus universitetas, gamtos mokslai, chemija – N 003),

doc. dr. Jolanta Rousseau (Artois universitetas, technologijos mokslai, medžiagų inžinerija – T 008),

prof. dr. Tomas Tamulevičius (Kauno Technologijos Universitetas, technologijos mokslai, medžiagų inžinerija – T 008),

doc. dr. Linas Vilčiauskas (Vilniaus universitetas, gamtos mokslai, chemija – N 003).

Disertacija ginama viešame Gynimo tarybos posėdyje 2023 m. rugsėjo mėn. 29 d. 14 val. Vilniaus universiteto Chemijos ir geomokslų fakulteto Kazio Daukšo auditorijoje (223 aud.).

Adresas: Naugarduko g. 24, LT-03225, Vilnius, Lietuva

Tel. +37052193105; el. paštas info@chgf.vu.lt.

Disertaciją galima peržiūrėti Vilniaus universiteto ir Fizinių ir technologijos mokslų centro bibliotekose ir VU interneto svetainėje adresu:

www.vu.lt/lt/naujienos/ivykiu-kalendorius.

TABLE OF CONTENTS

Abbreviations	9
INTRODUCTION	10
The aim of the thesis	11
The scientific tasks of the thesis	11
Novelty and importance of the work	12
Statements for defense	13
Contribution of the authors	14
1. LITERATURE OVERVIEW	15
1.1 Physical principles of multiphoton excitation and photopolymerization	16
1.2 Laser 3D lithography setup and strategies	20
1.3 Chemical principles of thresholded photopolymerization	23
1.4 Photoinitiators in laser lithography	25
1.5 Negative photo-resists	27
1.5.1 Acrylates	27
1.5.2 Hydrogels	29
1.5.3 Epoxy	31
1.5.4 Hybrid metal-organic materials and suspensions	32
1.6 Positive photo-resists	37
1.7 Thermal post-processing technique for 3D nanostructures	37
1.8 Trends and technical applications	39
1.8.1 Micro-optics	41
1.8.2 Nano-photonics	41
1.8.3 Micro-fluidics	41
1.8.4 Micro-mechanics	43
1.8.5 Nano-electronics	45
1.8.6 Sub-100 nm challenges: comparison of current achievements	45

1.8.7	Emerging applications	46
1.9	Summary and outlook	48
2.	EXPERIMENTAL	51
2.1	Materials and synthesis methods	51
2.1.1	Synthesis of Si/Zr metalorganic precursors	51
2.1.2	Synthesis of silicon-organic precursors	51
2.2	Characterization	53
2.2.1	Refractive indices measurements	53
2.2.2	FTIR measurements	53
2.2.3	TGA analysis	54
2.2.4	X-ray diffraction analysis	54
2.2.5	SEM and EDS analysis	54
2.2.6	Mechanical properties measurements	54
2.2.7	Densities measurements	54
2.2.8	UV-VIS transmittance measurements	55
2.3	Fabrication setups and parameters	55
2.4	Heat treatment	56
3.	RESULTS AND DISCUSSION	57
3.1	Introduction to high-resolution 3D inorganics fabrication	58
3.1.1	Refractive indices of SiX:ZrY materials	59
3.1.2	Fourier transform infrared spectroscopy analysis	60
3.1.3	Thermogravimetric and volumetric shrinkage analysis of SiX:ZrY materials	61
3.1.4	Investigation of fabrication prospects	63
3.1.5	Quality and composition of structures	65
3.1.6	Study of crystallization processes	66
3.1.7	Study on the resistance to aggressive impact	69
3.1.8	Conclusions on high-resolution 3D inorganics fabrication results	71
3.2	Introduction to manufacturing of 3D hard ceramic structures	76
3.2.1	Ceramic plate fabrication	76
3.2.2	Evaluation of refractive indices	77
3.2.3	Investigation of changes in chemical structure	79
3.2.4	Thermogravimetric analysis	81
3.2.5	Study of crystallization processes	83
3.2.6	3D fabrication prospects	85
3.2.7	Investigation of mechanical properties	88

3.2.8	Technical application in micro-optics	92
3.2.9	Conclusions on manufacturing of 3D hard ceramic structures	93
4.	CONCLUSIONS	95
	LIST OF PUBLICATIONS AND CONFERENCES PARTICIPATION	97
	BIBLIOGRAPHY	103
	APPENDIX	122
	SANTRAUKA	137
	Tyrimų sritis	138
	Tikslas ir uždaviniai	138
	Darbo naujumas	139
	Ginamieji teiginiai	140
	Rezultatų apžvalga	144
	Išvados	145
	PADĖKA	146
	CURRICULUM VITAE	147

ABBREVIATIONS

1PA	one-photon absorption
2PA	two-photon absorption
3D	three-dimensional
3DLL	three-dimensional laser lithography
D	energy dose
I	intensity
λ	wavelength
τ	pulse duration
f	frequency
P_{avg}	average measured laser beam power
ν	scan velocity
AAAPs	α -amino-alkylaceto-phenones
AESO	acrylated epoxidized soy oil
B3FL	2,7-bis((4-(dibutylamino)phenyl)ethynyl)-9H-fluoren-9-one
BSA	bivone serum albumin
CC	Creative Commons
D	donor
DFW	dynamic fabrication window
DH	donor-hydrogen
DIW	extrusion-based direct ink writing
DLP	digital light processing
DLW	laser direct write
DNQ	diazonaphthoquinone
EDS	energy dispersive X-Ray spectroscopy
ESA	excited state absorption
COD	Crystallography Open Database
fs	femtosecond
FTIR	Fourier-transform infrared spectroscopy
FW	fabrication window
GM	Göppert-Mayer units
HA-MA	hyaluronate methacrylate
HAPs	hydroxy-aceto-phenones
HEMA	hydroxyethyl methacrylate
HRIP	high-refractive-index polymers
IJP	inkjet-based printing
ISC	intersystem crossing
YAG	Yttrium Aluminium Garnet
LED	Light-emitting diode
M	monomer
MAA	methacrylic acid

MAPTMS	3-(trimethoxysilyl)propyl methacrylate
MEHQ	hydroquinone monomethyl ether
MEMS	microelectromechanical systems
MMMP	methyl-1-(4-methylthio)phenyl-2-morpholinopropan-1-one
MPI	multiphoton ionization
MPL	multiphoton lithography
MTMS	trimethoxymethylsilane
NA	numerical aperture
NEMS	nanoelectromechanical systems
P2CK	sodium 3,3-(((1E,1E)-(2-oxocyclopentane-1,3-diylidene)bis(methanylylidene))bis(4,1-phenylene))bis(methylazanediy)) dipropanoate
PEGDA	polyethylene glycol diacrylate
PGMEA	propylene glycol monomethyl ether acetate
PI	photoinitiator
R	radical
RI	refractive index
SEM	scanning electron microscope
SL	stereolithography
STED	stimulated emission depletion
TGA	thermogravimetric analysis
TPP/2PP	ultraviolet two-photon polymerization
UV	ultraviolet
VIS	visible
ZPO	zirconium(IV) propoxide

INTRODUCTION

The field of ceramics and ceramic-like materials has attracted considerable attention in engineering due to their exceptional mechanical, chemical, and thermal properties [1]. There is a growing interest in advanced resins and innovative fabrication processes to meet the increasing demand for novel 3D ceramic micro/nano-structures that cannot be achieved using conventional manufacturing technologies. The most precise and versatile technology for fabricating inorganic 3D ceramics is the combination of femtosecond laser-based 3D lithography (3DLL) and thermal treatment [2–4]. This technology is highly suitable for various applications ranging from micromechanics [5] to biomedicine [6], integrated micro-optics [7], and photonics [8]. However, there is still a need for a wider variety of initial materials, further optimization of the composition of starting materials and calcination conditions to fully propagate and enhance this technology.

Extensive research has focused on the production of photoactive suspensions and their effectiveness in fabricating 3D ceramics. Typically, these suspensions consist of finely dispersed ceramic particles within organic resin matrices, such as inks or pastes. The selection of materials for these suspensions includes metal or semimetal oxides, carbides, borides, nitrides, and glass grains, which are appropriately dispersed within organic monomers [9, 10].

The presence of inorganic particles in suspensions can lead to challenges such as agglomeration and sedimentation, resulting in final 3D objects. The chemical differences between organic resins and inorganic particles make it difficult to prepare a stable and transparent solution. When the material lacks transparency, the laser light can scatter or be absorbed, causing a reduction in laser power at the point of polymerization, which introduces poorly controllable fabrication system setup. As a result, irregularities may appear in the final structure. Additionally, structures fabricated from suspensions often undergo significant deformation during the heating process [11].

To overcome these limitations, the development of homogeneous hybrid metal-organic resins is currently underway. These resins aim to combine the advantages of both metal-organic frameworks and organic polymers to address the aforementioned disadvantages. Homogeneous mixtures strive to

enhance stability, improve processability, and achieve desirable mechanical and functional properties in the resulting 3D objects.

In this context, the present dissertation research aims to tackle the challenges of obtaining accurate and hard 3D ceramic objects by exploring new advanced hybrid materials, production processes and application in 3D multi-photon lithography. The study focuses on the synthesis and manufacturing of 3D objects through direct laser printing, as well as the transformation from 3D hybrid polymeric structures to ceramics with unique properties. The characterization and experimental conditions of 3D lithography and heat treatment are also presented. The results demonstrate the achievement of the highest resolution below 60 nm for free-form 3D $\text{SiO}_2/\text{ZrO}_2$ inorganic 3D object and the unique mechanical properties of 3D SiOC , SiC , and $\alpha,\beta\text{-Si}_3\text{N}_4$ ceramics. Ultimately, this thesis contributes significantly to the advancement of methodologies dedicated to manufacturing of ultra-small and robust 3D ceramic objects, with direct relevance to industrial applications.

THE AIM OF THE THESIS

The aim of this thesis was to synthesize a range of metal-organic precursors via the sol-gel method and prepare ceramic 3D micro/nanostructures by combining femtosecond laser lithography and pyrolysis.

THE SCIENTIFIC TASKS OF THE THESIS

In order to fulfill the aim of the dissertation, the following tasks were formulated:

1. To prepare (synthesize) hybrid silicon/zirconium-organic and silicon-organic compounds via sol-gel method.
2. To assess the feasibility of the synthesized materials for femtosecond laser-induced polymerization and to explore the influence of different parameters and materials composition on the overall quality of the produced 3D objects.
3. To examine the effects of pyrolysis/calcination parameters such as temperature, duration, and atmosphere on the deformation, shrinkage, chemical, physical, and mechanical properties of the resultant ceramic 3D micro/nano-objects.

NOVELTY AND IMPORTANCE OF THE WORK

This dissertation was inspired by the challenge of fabricating precise and hard 3D ceramic objects. The research focused on the exploration of novel silicon-organic materials, its manufacturing process, utilization in 3D multi-photon lithography and the transition from 3D hybrid polymeric structures to ceramics with unique properties. A novel approach for direct measuring the crystalline phase of 3D micro-objects using a single crystal X-Ray diffractometer was demonstrated for the first time. The study also achieved a new record for the highest resolution below 60 nm of free-form 3D SiO₂/ZrO₂ inorganic objects.

Furthermore, a novel silicon-organic material was developed, showcasing remarkable advancements in its mechanical properties, specifically tailored for additive manufacturing. The amorphous SiOC, SiC, and α,β -Si₃N₄ ceramics demonstrated negligible deformation or decomposition, however provided for a uniform repetitive decrease in volume, increased hardness upon heating (up to ≈ 15 GPa) and reduced elastic modulus (up to ≈ 105 GPa). These accomplishments (≈ 15 GPa hardness and ≈ 60 nm resolution) have facilitated the commercial applicability of these materials by overcoming significant scientific and engineering challenges, creating new opportunities for industrial applications.

STATEMENTS FOR DEFENSE

1. The sol-gel method is a suitable approach for the efficient synthesis of transparent hybrid silicon and zircon metal-organic compounds for 3D laser photopolymerization. It is possible to control the properties of materials prepared using 3-methacryloxypropyltrimethoxysilane and zirconium propoxide by altering the molar ratio in the range from 9:1 to 5:5.
2. The resolution of 3D-printed ceramic structures depends on the initial photoactive material composition, the laser parameters during photopolymerization and the heating protocol. Hence, it is possible to achieve nano-scale feature size down to 60 nm for 3-methacryloxypropyltrimethoxysilane : zirconium propoxide 9:1 material using fabrication parameters: 300 fs laser pulse duration, 200 kHz repetition rate, 200 $\mu\text{m/s}$ printing velocity, and 64 μW laser power (irradiation 0.22 TW/cm²) followed by annealing at 1000 °C.
3. The crystalline phases of powders and 3D objects with identical compositions exhibit structural variations. Crystalline phases of both the

3D objects and powders vary differently by adjusting the molar ratio of the initial precursor (3-methacryloxypropyltrimethoxysilane : zirconium propoxide) from 9:1 to 5:5 and the heating temperature from 1000 °C to 1400 °C.

4. The sol-gel method is suitable for stable, and transparent advanced silicon-organic materials fabrication for 3D laser lithography. It is possible to control the chemical properties of materials by changing the molar ratio of trimethoxymethylsilane and 3-methacryloxypropyltrimethoxysilane (9:1, 8:2 and 7:3).
5. The mechanical properties of prepared SiOC, SiC, and α,β -Si₃N₄ ceramic objects depend on chemical composition and post-processing conditions. Hence, it is possible to obtain hard 3D ceramic structures (hardness up to ≈ 15 GPa, reduced elastic modulus ≈ 105 GPa) using 8:2 (trimethoxymethylsilane : 3-methacryloxypropyltrimethoxysilane) initial material followed by annealing at 1200 °C temperature under nitrogen atmosphere.

CONTRIBUTION OF THE AUTHORS

Prof. Dr. Simas Šakirzanovas – academic supervisor of the work, led and consulted on Ph.D. studies, provided access to necessary equipment (chemical synthesis laboratory, devices for determining the properties of materials and 3D objects, and heating equipment), and suggested interpretations of presented experimental results. Provided general insights in scientific publications and Ph.D. thesis.

Prof. Dr. Mangirdas Malinauskas – academic consultant of the work, consulted on Ph.D. studies, provided access to necessary equipment (3D fabrication setup), and introduce to physical interpretations for technology. Provided general insights in scientific publications and Ph.D. thesis.

Dr. Darius Gailevičius – consulted on research and experiments, performed laser photopolymerization of woodpiles and scaffolds and provided general insights in scientific publications and Ph.D. thesis.

Dr. Linas Jonušauskas – performed physical interpretations for technology.

Laurynas Staišiūnas – performed measurements of mechanical properties.

Edvinas Aleksandravičius – performed laser photopolymerization of woodpiles and scaffolds.

Rokas Vargalis – performed high-resolution scanning electron microscopy measurements.

1. LITERATURE OVERVIEW

Development of 3D micro-/nano-objects plays a crucial role in the miniaturization of devices, enabling enhanced functionality and integration possibilities in various fields such as photonics, microfluidics, micromechanics, microelectronics, and micro-optics. One prominent technique for fabricating these objects is multi-photon lithography, also known as two-photon polymerization, which utilizes laser direct writing to rapidly prototype 3D structures. Recent progress in this ultrafast laser technique, coupled with advancements in material science, has made routine 3D printing of inorganic structures possible through a combination of mask-less photopolymerization and subsequent thermal post-treatments. These recent achievements hold great promise for technical applications requiring highly resilient structures composed of inert and durable materials capable to withstand harsh environments.

Multi-photon 3D lithography [12] (specifically, two-photon polymerization (TPP) [13]) is already a well-established technique among scientists and is readily available in the industry [14]. Its versatility meets the requirements for a plethora of micro- and nano-scale applications where true 3D structures and high feature definitions are needed [3]. It can be extended to larger dimensions of up to mm-scales (upscaled) with a wide variety of materials to choose from [12, 15].

By definition, the outcome of the photopolymerization process is inherently related to the choice of cross-linkable materials. The materials can be purely organic or organic-inorganic hybrids [16]. This is indeed acceptable to a great extent for prototyping and additive manufacturing of objects applicable in micro-optics, nano-photonics, microfluidics, micromechanics, biomedicine, sensor and diverse templating (master or mask making) [17]. Such devices must feature high performance and durability under harsh conditions.

On the other hand, glasses, ceramics, and crystalline materials possess exceptional properties as technical materials, characterized by high resilience, transparency, and low reactivity. Consequently, technologies have been developed to create inorganic 3D objects that fulfill these requirements. One such technology is based on a combination of photoactive hybrids synthesis (typic-

ally sol-gel), photopolymerization, and high-temperature post-processing.

In the case of metalorganic resists specifically designed for multiphoton polymerization, the application of heat treatment leads to several notable effects. Firstly, there is an increase in the degree of cross-linking and densification, followed by material decomposition, along with geometrical downscaling. Furthermore, at elevated temperatures ($> 1000\text{ }^{\circ}\text{C}$) inorganic glass-ceramic phase transition material phases can be observed followed by the emergence of fully crystalline phases. This simultaneous geometry and material provide the possibility to produce unique devices unachievable using other methods.

Up to now, additive manufacturing of sol-gel materials and fabrication of inorganic objects was limited to the micro-scale. However, recent advances in femtosecond laser material processing enabled the fabrication of features on the nano-scale. With a combination of ultrafast lasers (both, short pulses and high repetition rates) the 3D lithography is becoming a precision additive manufacturing tool with $\sim 100\text{ nm}$ spatial definition (resolution) on demand. Combination with pyrolysis/calcination post-treatment enables reaching extreme scales of sub-100 nm and fabrication of pure inorganic objects. This is a milestone achievement in ultrafast laser nanostructuring and in the following chapters will be discussed in detail of physical-chemical principles, technological realization, examples of novel emerging applications, and a future outlook.

Literature overview is written based on the printed article [A1] (see list of publications): G. Merkininkaite, et. al. „Polymers for Regenerative Medicine Structures Made *via* Multiphoton 3D Lithography: a Review“. International Journal of Polymer Science. Vol. 2019, 3403548, 23, 2019, doi.: 10.1155/2019/3403548, and book chapter [B1] (see list of publications): G. Merkininkaite et al. „Multi-photon 3D lithography for sub- 100 nm additive manufacturing of inorganics“. In: Stoian, R., Bonse, J.(eds) Ultrafast Laser Nanostructuring. Springer Series in Optical Sciences. Vol 239. Springer, Cham. Chapter No. 22, 2023, doi.: 10.1007/978-3-031-14752-422.

1.1 Physical principles of multiphoton excitation and photopolymerization

A non-linear thresholded photo-response of polymeric material is exploited for the laser direct write (DLW) 3D nanopolymerization [15, 17]. The photo-excitation of the organic monomer (prepolymer) molecules can be utilized as a linear or non-linear light-matter interaction *via* one-photon, two-photon and multi-photon absorption mechanisms. Additionally, during exposure avalanche ionization and thermal accumulation, might occur [18]. The interplay between these processes is not trivial.

Although, the technique is being widely used and commercially established, still intensive research effort is being invested to better understand the funda-

mental processes. This is illustrated in some recent prominent review papers on that topic [15, 19]. Furthermore, a decade-long dispute about the dominant mechanisms, which will be discussed below, is still in progress *via* original research dedicated papers [20, 21].

In one-photon absorption, a molecule absorbs a single photon. While two-photon absorption occurs when two lower-energy (compared to single-photon adsorption) photons are absorbed simultaneously. The energy of the absorbed photon (in the case of one photon (1PA)) or two photons (in the case of TPA (further 2PA)) must be equal or higher to the energy difference between the ground state and the excited state of a molecule. Both absorption mechanisms involve the excitation of the photoinitiator molecule from the singlet ground state (S_0) to the excited singlet manifold (S_1) (see Figure 1.1). Subsequently, it relaxes to the lowest S_1 energy state, undergoes intersystem crossing (ISC) to the lowest triplet state, thereby initiating radical generation [19].

However, when dealing with long-lasting triplet states (for example, if the triplet state is lower than the dissociated state or if there exists a potential barrier), the excited state absorption (ESA) from the triplet becomes necessary to generate radicals.

In multiphoton ionization (MPI) (see Figure 1.1), a photoinitiator may not be necessary, as the monomer itself can be photoionized. For short pulse durations (100 fs), direct multiphoton ionization dominates, while for longer pulse durations, it primarily serves as a seeding mechanism for avalanche generation. However, both cases require initiation by multiphoton ionization and large pulse energies. Radicals can be generated through nonresonant reactions *via* photothermal dissociation of photoinitiator or monomer molecules. This photophysical reaction pathway is expected to dominate if the number of laser pulses hitting a voxel is low or if a photoinitiator is absent, resulting in higher required pulse energies compared to two-photon absorption [18].

One-photon absorption has some distinct disadvantages. While collimated light can induce polymerization reaction in the relatively big (up to cm) area with high repeatably [22], achieving true 3D shapes is tricky. The standard way used in stereolithography is stacking 2D layers on top of each other. This leads to the necessity to use supports if free-hanging features are made [23]. Also, resins need to be liquid in order to cast a new layer after the previous one is done. Thus, while one-photon absorption is a powerful tool for manufacturing various structures, there are also some severe limitations.

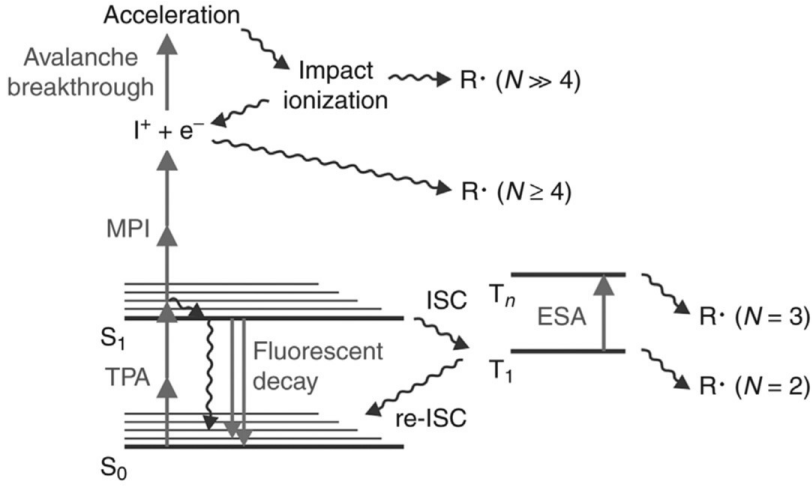


Figure 1.1: A schematic representation of possible two and multi-photon absorption pathways. Reprinted with permission from [18].

In 2PA case, the number of absorbed photons n_p per time t can be calculated using the following equation [A1]:

$$\frac{dn_p}{dt} = \sigma_2 N F^2, \quad (1.1)$$

here σ_2 is 2PA cross-section of a particular material (quantified by Göppert-Mayer units, $\text{GM} = 50^{-50} \text{ cm}^4 \text{ s}$), N is the density of absorbing component and F is photon flux which can be defined as $F = I/h\nu$. Conclusions about what practical considerations should be made when trying to apply 2PA for polymerization can draw from Eq. 1.1. First, the photon absorption rate is proportional to I^2 , making excessive I one of the main considerations. The N should also be sufficient for the reaction. Finally, the material needs to be reactive enough to have high σ_2 . The first requirement is realized using appropriate processing setup, second and third by tuning the material properties. The nonlinearity of the process behind 3D laser lithography is the key to achieving fabricated features below the diffraction limit.

Most often a localized photo-chemical modification (Figure 1.5) can be achieved by optimizing light exposure parameters. Usually, this includes intensity - I [W/cm^2], and corresponding energy dose - D [J] for the specific material to fit within the fabrication window (FW, or a dynamic DFW taking into account the ratio of damage and initiation thresholds). Fine-tuning these values can ensure fine 3D structuring (Figure 1.4). The final object dimensions and resulting resolution will depend on the interplay between laser exposure (I, D), material response (sensitivity, diffusion of reaction), and geometrical

rigidity (architecture) - thus, in turn, will be defined by physical, chemical and engineering thresholds [15]. The routinely observed spatial dimensions of single voxels are down to 100 nm lateral and 300 nm longitudinal dimensions (see Figure 1.2). And the production throughput can reach tens of thousands of individual voxels per second which makes it an extremely efficient precision (in nanoscale) additive manufacturing tool [12, 24].

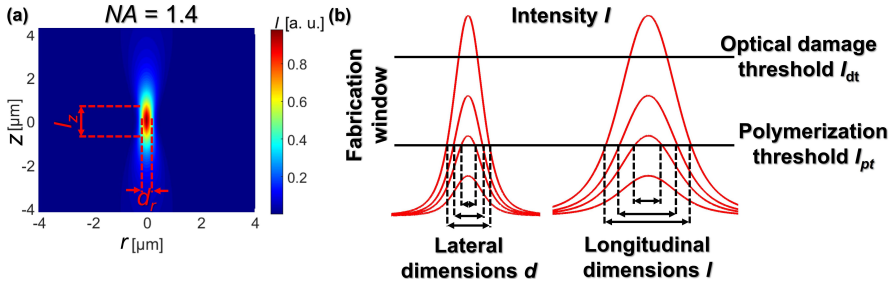


Figure 1.2: Non-linear thresholded photoresponse of a prepolymer confined by the incident light's intensity spatial distribution. (a) - light intensity distribution using NA = 1.4 immersion oil objective. The photo-modified volume is defined by the lateral d_r and axial l_z isointensity region exceeding the non-linear absorption threshold (corresponding to the highest photon density). The *voxel* (volumetric pixel) is elongated along the beam propagation direction following the incident energy density distribution. r and z depict realistic probable dimensions in spatial units while I is normalized. (b) - scaling by intensity tuning: lateral and longitudinal dimensions, respectively. By adjusting the incident laser I fitting within the polymerization threshold (irreversible photomodification) and damage threshold (bubbling, explosions, uncontrolled burning) one can linearly vary the cross-linked volume from sub-wavelength to wavelength dimensions (lateral). The axial dimensions will be enlarged depending on the focussing optics and will follow quadratic dependence on NA. Figure adapted from [15].

However, the most recent development within the MPL community pertains to Professor Wegener's scientific study regarding two-step absorption instead of two-photon absorption [25]. In this research, Professor Wegener and his team have devised a light-sensitive material that employs an actual energy level for electron excitation, as opposed to a virtual level, thereby preserving the quadratic nonlinearity relationship. The achievement is attainable using a continuous-wave laser diode, resulting in a structured pattern with a mere 300 nm period. This technology is undergoing further refinement, with ongoing efforts to achieve elevated printing speeds based on the principles of light sheet microscopy.

1.2 Laser 3D lithography setup and strategies

In order to realize 2PA a special workstation is required. In a very generalized case there are 4 main components in each 3D laser lithography setup: laser source, relay optics, sample positioning and imaging system [Figure 1.3]. Furthermore, choosing correct writing strategies are also extremely important, because they can influence both: mechanical properties of the structure as well as manufacturing throughput. Thus, when considering the capabilities of 3D laser lithography the hardware/software part of the technology should not be overlooked.

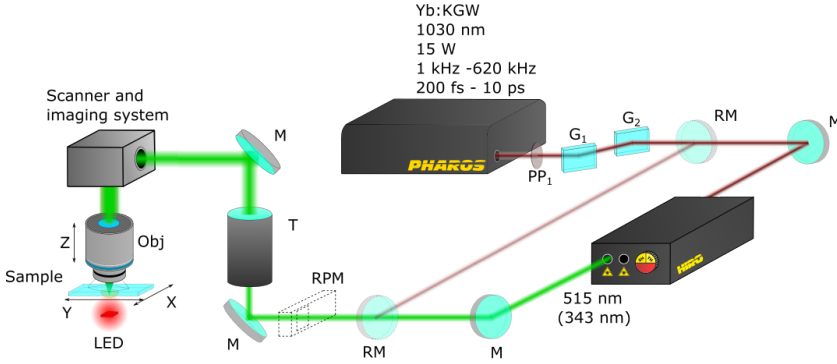


Figure 1.3: Simplified schematics of a 3D laser lithography fabrication setup employing amplified fs laser and harmonic generator. Here PP₁ is a phase plate, G₁ and G₂ are Brewster angle polarizers, M - mirrors, RM - removable mirror, RPM - removable power meter, T - telescope, Obj - objective. Taken from [12].

As discussed previously, 2PA is a nonlinear process requiring high light intensity (I). The peak intensity I in a focused Gaussian beam can be obtained through the following equation [26]:

$$I_0 = \frac{2P}{f\omega_0^2\pi\tau}, \quad (1.2)$$

here P is average laser power, f - laser repetition rate, $\omega_0 = 0.61\text{NA}/\lambda$ is a radius of beam waist and τ is pulse duration. As can be seen, the laser source is responsible for most parameters leading to high I (P , f and τ). For this reason, ultrafast fs laser with high P (up to few hundred mW), reasonable f (which rarely exceeds MHz) and very short τ (tens of fs range) is the best candidate to induce 2PA [27]. Nevertheless, picosecond (ps) [28], nanosecond (ns) [29] and even continuous wave (cw) [30] lasers were used for 3D laser lithography. However, in these cases 2PA is surpassed by thermal effects and

avalanche ionization as a dominant process for inducing polymerization. This resulted in a decrease in fabrication window and/or necessity to use substantial lower translation velocity, thus making ultrafast lasers a primary choice for high-efficiency 3D laser lithography setups. It is interesting to point out that both oscillators and amplified fs laser systems can be used. The latter laser systems are also capable of subtractive laser manufacturing, such as ablation or selective glass etching [31–33]. Thus, a setup with such laser can perform both additive and subtractive laser processing.

The purpose of relay optics is quite straightforward - direct laser light from laser to the sample. However, peculiarities of this operation should not be overlooked. As established in last paragraph, laser should be emitting fs pulses. In the case of oscillators such pulses can be extremely short (sub 100 fs) and, in turn, have relatively broad spectral width. Furthermore, several laser harmonics might be used in one 3D laser lithography setup [12]. Therefore, optics in the setup have to be able to sustain all of the relevant harmonics with respective spectral widths. In addition, optics have to assure that there is a minimal temporal pulse broadening due to de-chirping of the pulse as it passes various optical elements or it is appropriately controlled for the benefit of printing [34, 35]. Alongside spectro-temporal requirements, optical chain also has to assure that there are no spatial disturbances to the beam. Indeed, to achieve maximal possible writing accuracy laser beam has to be as close to Gaussian as possible [36]. Additionally, the beam diameter should match the aperture of focusing optics, introducing the need of a telescope. Finally, an appropriate numerical aperture (NA) objective should be chosen to accommodate needed feature size/throughput compromise. The light intensity in the focal region of Gaussian beam can be defined as [37]:

$$I(r, z) = I_0 \frac{\omega_0^2}{\omega(z)^2} \exp\left(\frac{-2r^2}{\omega(z)^2}\right), \quad (1.3)$$

here r is the distance from the optical axis, z - distance from the focal plane parallel to the optical axis. Because ω_0 depends on NA, by changing the objective one can relatively easy tune the size of the modified volume.

3D laser lithography is realized by moving a focused laser beam in relation to a sample or sample in relation to the laser beam. At the onset of the technology piezoelectric (piezo for simplicity) stages were used [38]. They provide extreme precision down to the sub-nm scale. However, their working area is extremely limited (no more than several hundred μm) and translation velocities are limited. They were also sensitive to physical overloads due to the danger of the piezocrystals cracking. These problems meant that piezostages were gradually phased out from the fields where high-throughput printing was necessary. The two next easily applied options were galvanometric scanners and linear stages. Scanners are superb positioning tool for very high

throughput fabrication due to the minimal inertia [39]. This means that cm/s translation velocities can be achieved even while fabricating very complex shapes. The downside of this approach is the printing area being confined to a working field of an objective which is in order of several hundred μm . If structure dimensions exceeded working area of an objective, it had to be divided into segments which were then printed one-by-one, resulting in stitching between segments [40–43]. Stitches induce optical and mechanical defects which might compromise functionality of the structure. Linear stages do not have this problem and can produce cm-sized structures at high translation velocities (up to cm/s) if the structure is simple and based on straight lines [44–46]. However, due to the high inertia of the stages, distortions might appear in more complex cases also creating a limitation. The solution to these problems is synchronization of galvanometric scanners and linear stages allowing to achieve stitch-free printing with superb quality of complex 3D shapes at high translation velocities [12].

The final component necessary for practical 3D laser lithography setup is integrated imaging system. In the simplest case it is needed to assure that structure is fabricated at appropriate position of the sample and for real time observation of the printing process [45]. At the same time the functionality of imaging system can be expanded to include additional functions, such as autofocus. In general sense, autofocus is needed to find interface between pre-polymer and substrate. It minimizes the workload on the setup operator and enhances repeatability and precision of such operation. Depending on desired result, it can be achieved by using existing imaging hardware and additional image post processing [47], or by introducing more components into the setup [48]. It is important to note that implementation of autofocus is relatively simple in 3D laser lithography case due to fluorescence of most processable polymers. This sharply contrasts with finding interface between two non-fluorescent transparent mediums where more advanced solutions are needed [49].

Such 3D laser lithography fabrication setup is appropriate for sol-gel based materials photopolymerization due to their easy sample handling and exposure trajectory while being in a gel state, as well as mechanical properties to survive the whole process till producing complex 3D object. The typical protocol scheme of 3D inorganics fabrication is depicted in Figure 1.4. It includes DLW, wet chemical development and high-temperature treatment. Finally, the produced structures can serve as templates for various post-processing solutions including plasma etching, metal sputtering, atomic layer deposition and replications. Altogether such a method can be readily exploited for additive manufacturing of inorganic substances at micro and nano-scale dimensions.

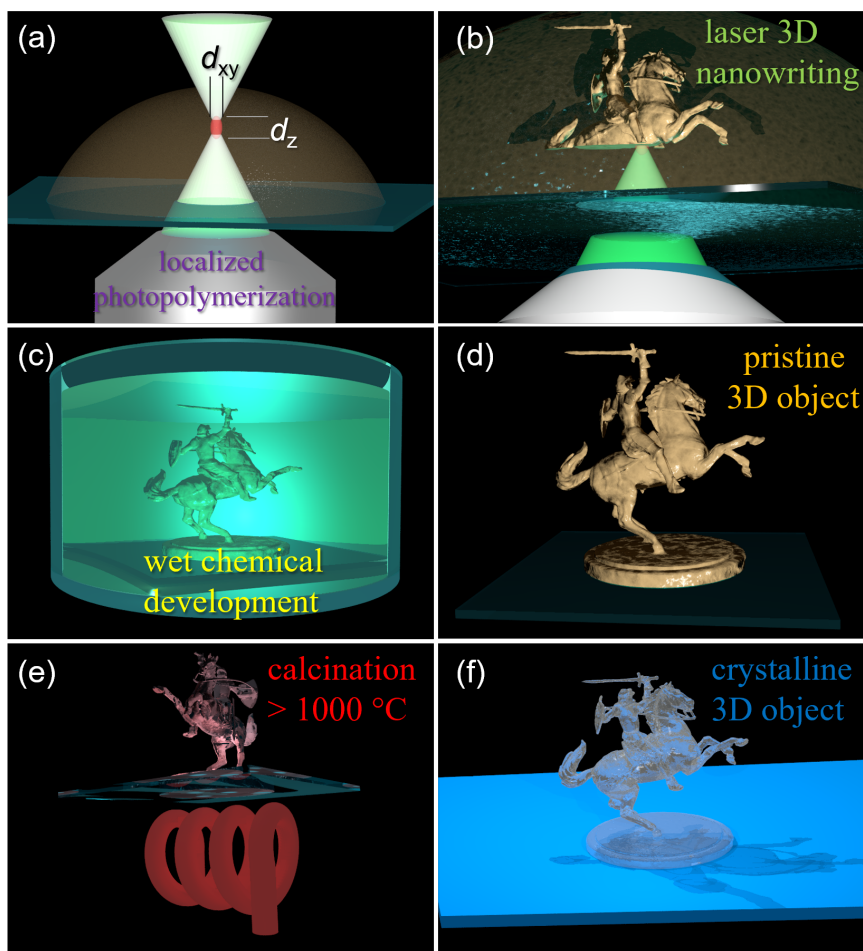


Figure 1.4: Visualization of DLW process and heat treatment. (a) shows the basic building block of the structure – the "voxel" characterized by its transverse and longitudinal dimensions, (b) the process of sequentially scanning the hybrid metal-organic prepolymer and forming the desired structure, (c) the development process to remove the unexposed material, (d) 3D polymeric structure, (e) calcination as a route for ceramic 3D nano-structures production, (f) final crystalline 3D object.

1.3 Chemical principles of thresholded photopolymerization

The main goal of using light in lithography is to induce photocleavage of chemical bond and initiation of photochemical reactions. The photopolymerization process from a chemical perspective is based on the interaction between light radiation with a photoinitiator and monomer. The mechanism of free radical polymerization is shown in Figure 1.5. Free radical polymerization

consists of four fundamental steps: initiation, propagation, chain transfer and termination.

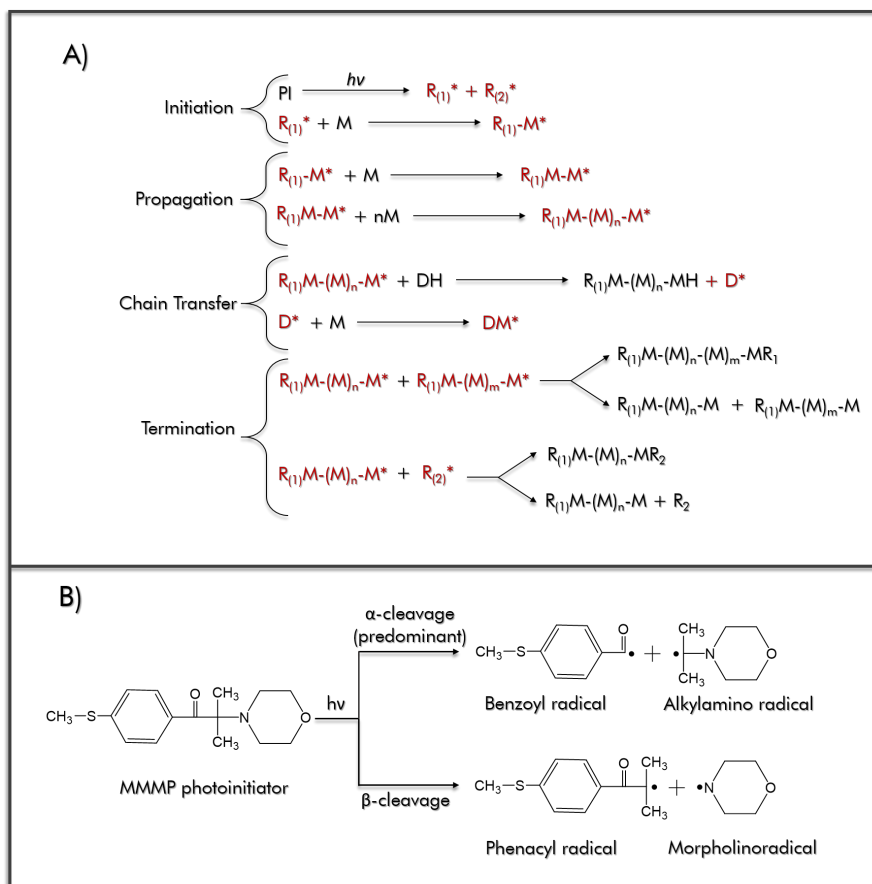


Figure 1.5: A) - steps of the free radical polymerization including initiation, propagation, chain transfer and termination. PI- photoinitiator, M- monomer, D- donor, R- radical. Red markings show the active substance that further participates in the reaction. B) - photocleavage example of methyl-1-(4-methylthio)phenyl-2- morpholinopropan-1-one (MMMP) photoinitiator. Figure reproduced from [50].

Initiation involves the formation of radicals after the absorption of photons as described previously. The most commonly used initiating molecules are photo-degradable aldehydes or ketones. They have a tendency to split into two fragments with unpaired electrons: after photon absorption [51]. In general, cleavage occurs at any weak bond but usually takes place at the α - position of the carbonyl group and less frequently at the β - cleavage Figure 1.5B. Chemical families of such type photoinitiators are hydroxyacetophenones,

benzylketals, benzoin derivatives, α -aminoalkylacetophenones, phosphine oxides, α -haloacetophenones, trichlormethyl-S-triazine and others [50]. Chemical formulas of structures (photoinitiators and monomers) are shown in 1.1 table. Basically, following radicals generation, active species then react with any monomer such as α , β - unsaturated aldehydes/ketones, acrylates, vinyl esters, vinyl sulfones, imidazoles, maleimides, etc. During this process, a free radical of the photoinitiator attacks the double bond of the monomer, and the new radical is formed ($R_{(1)}-M$)*. In this way, chain initiation consists of two described steps (Figure 1.5A), Initiation part).

During propagation, a polymer increases its chain length by the fast and progressive addition of monomers to the growing polymer chain keeping active centers. Ideally, the propagation step would continue until all monomers are consumed. However, pairs of radicals also tend to react with each other, annihilating their activities. Such behavior is called termination and is schematically depicted in Figure 1.5A Termination part.

Short polymer chains can be formed due to a side reaction called chain transfer. This reaction can be caused by a small molecule, such as a chain transfer agent, solvent, initiator, monomer, or polymer, which in the scheme corresponds to DH (Figure 1.5A, Chain Transfer). Chain transfer effect results in the destruction of one radical, but also the creation of another radical in contrast to termination. In many cases, however, a newly created radical is unable to propagate further [52].

1.4 Photoinitiators in laser lithography

Correct choice of PI is imperative for 3D laser lithography. PI's influence on the whole printing process is immense because it determines what laser wavelength should be used and what is the fabrication window. When 3D laser lithography was first used, photopolymers with PIs designed for one UV photon absorption were applied due to being readily available [53, 54]. From the first glance it might seem that adoption of one photon PIs for 2PA should be pretty straightforward by just making sure that fs laser wavelength is half of the absorption peak of the PI. However, interestingly enough, it was shown that sometimes PIs with huge one photon absorption cross-section σ_1 can have very small σ_2 in the range of tens GM [55]. In comparison, σ_2 can go as high as more than a thousand GM [55]. This proves the necessity to create PIs specially designed for 2PA.

2PA-oriented PIs can be realized by using D- π -D, D- π -A, D- π -A- π -D, and A- π -D- π -A type chemical compounds showing large changes of dipole/quadrupole moment upon excitation, with extended conjugation in molecules [56]. Here π is a π -conjugated backbone (for example, vinyl groups in ethynylphenyl, ethynylene or phenyl), D usually represents hydrogen, methoxy, alkylamino,

Table 1.1: Possible photoinitiators and monomers for UV lithography.

Nr.	PI group name	PI structure	Monomer name	Monomer structure
1.	Hydroxy-acetophenones (HAPs)		α, β -unsaturated aldehydes	
2.	Benzylketals		α, β -unsaturated ketones	
3.	Benzophenone		α, β -unsaturated acrylates	
4.	Benzoin derivatives		Vinyl esters	
5.	α -amino-alkylacetophenones (AAAPs)		Imidazoles	
6.	Phosphine oxides		Vinyl sulfones	
7.	α -haloacetophenone		Maleimides	
8.	Trichloromethyl-S-triazine		Epoxides	

such as, dimethylamino, diphenylamino, and dibutylamino groups which act as electron-donors, and A- acceptors (for instance, various cycloketones, ketones, pyridine or pyridinium) (see Figure 1.6) [56–58]. D- π -D and D- π -A- π -D are two of the most commonly used PI systems in 2PA.

Important requirement of PIs is the sufficient two photon absorption cross section value which is most dependent on the chemical structure, hydrophilicity/phobicity and solvent. According to M. Albota et. al, the two photon absorption cross section increases due to the increasing conjugation length of the molecule or the increasing extent of symmetrical charge transfer from the ends of the molecule to the middle, or vice versa [59]. Furthermore, the 2PA cross section value was equal to 176 GM of the hydrophilic PI P2CK (Figure 1.6) under 800 nm excitation in water, while its hydrophobic analogue (B3FL) in chloroform- 466 GM [60]. The hypothesis of such behavior is interpreted by hydrogen bonding between solute and solvent, changes in the PI geometry or aggregation [57].

While PIs are the primary way to induce crosslinking, it was also showed that in some cases polymerization reaction can be induced even without PI present [26, 61, 62]. This potentially eliminates the need to use PI and, thus, optimizes its printing conditions. On the other hand, it reduces the fabrication window, potentially weakens the structure mechanically and creates additional requirements for the light source [26]. This is due to the change in the undergoing light-matter interaction. It was calculated that if PI is not present, avalanche ionization might become a comparable or even greater contributor to chemical bond cleavage than 2PA [63]. However, as avalanche requires time to achieve its full potential, relatively longer pulses in the range of hundreds of fs are necessary.

1.5 Negative photo-resists

A negative photoresist is a type of photoresist in which the portion of the photoresist that is exposed to light becomes insoluble to the photoresist developer. The unexposed portion of the photoresist is dissolved by the photoresist developer. Possible monomers for UV lithography were depicted in 1.1 table. However, there are three main groups of photoresists that are commonly used in a TPP which are discussed below.

1.5.1 Acrylates

Acrylates are one of the most commonly used families of photopolymers in 3D printing due to their high photoactivity and chemical tunability. Historically it was the first polymer structured in 2PP [53]. Acrylates are a family of polymers made from acrylate monomers which are esters. The significant feature of acrylates is that vinyl groups are directly bounded to the carbonyl

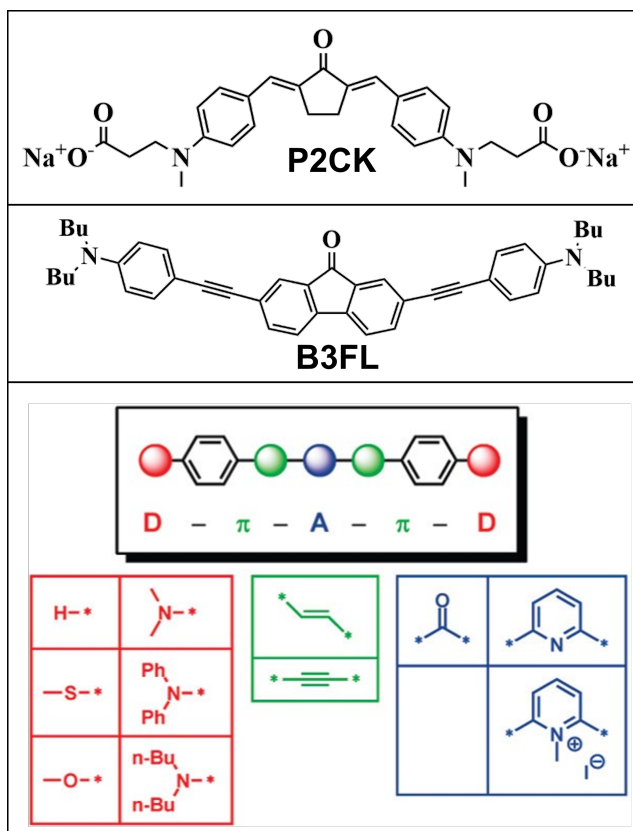


Figure 1.6: Structural formulas of 2PA PIs. Here P2CK is PI soluble in water, while B3FL- soluble in organic solvents [A1]. D- π -A- π -D conjugated system model is depicted below. The figure is adapted from [56, 58].

carbon. These monomers are important due to their bifunctionality. The vinyl group is responsive for polymerization [64]. The carboxylate group carries numerous functionalities providing the ability to modify the composition and chemical structure of acrylates. The polymerization chemistry of acrylates is based on the differences between two vinyl carbon atoms. Vinyl groups possess an abundance of electron density, whereas carboxyl groups exhibit a high level of polarity. Therefore, the carboxyl group in acrylates attracts electrons from the vinyl group, leading to a deficit of electrons in alpha carbon and an excess in beta carbon (see Figure 1.7). This property results in the high activity of acrylates in the free radical polymerization reactions.

Many acrylates with diverse properties can be obtained by altering the groups connected to the alpha carbon and carboxylate. For example, methyl, ethyl or other organic chain having acrylic, methacrylic, cyanoacrylic esters [65].

There are abundant acrylates monomers and oligomers that are photosensitive, such as hydroxypropylacrylate, hexanediol diacrylate, polyester tetra-acrylate, hexaacrylate, oxazolidone acrylate, pentaerythritol triacrylate, urethane acrylate, some fluorinated acrylates, methyl methacrylate and so forth [66]. Many acrylates possess appealing properties depending on their chemical structure, such as high chemical and heat resistance, stability, toughness, favorable stiffness, flexibility, optical clarity [65, 67] or 3DLL forming possibility. It is known that, for instance, in polymethyl methacrylates, the softening point, density, and refractive index decrease while toughness increases as the ester chain lengthens. By changing the ester group from methyl to isobutyl in polymethyl methacrylate, the density can range from 1.19 to 1.02 g/cm³, the refractive index can vary from 1.48 to 1.45, and the softening point can be adjusted from 125 °C to 62 °C [65]. On the other hand, when it is necessary to achieve polymers with specific properties, it is possible to combine other monomers or modifiers through copolymerization reactions. As a result, copolymers [65, 68] and blends, also known as acrylic multipolymers [65] can be obtained. Certain components, such as ethoxylated trimethylolpropane triacrylate, are used to reduce shrinkage during photopolymerization [69]. To enhance the hardness of the polymer, tris(2-hydroxyethyl)isocyanurate should be added [69]. Various modified acrylates have been utilized in 3DLL over the years [70–72]. Overall, acrylate groups play a significant role in the discussed polymers, making acrylate chemistry a fundamental aspect of 3DLL.

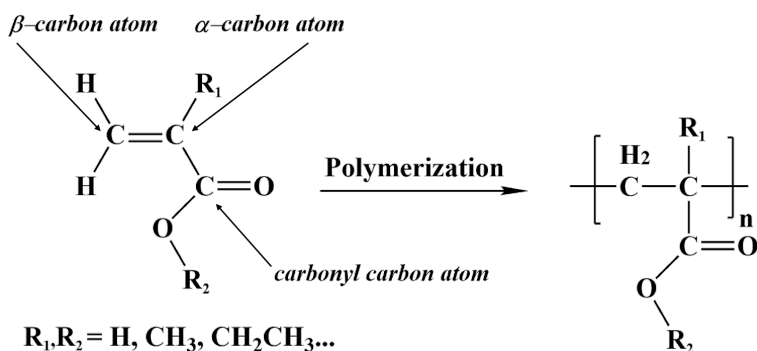


Figure 1.7: Structural formula of acrylates before and after polymerization. Here R_1 and R_2 are organic substituents, n - degree of polymerization. Alpha, beta and carbonyl carbon atoms are shown [A1].

1.5.2 Hydrogels

Hydrogels can be defined as polymeric networks with the capacity to absorb and retain a significant amount of water within their 3D structures. This

unique property is attributed to the chemical structure of the material. The hydrogels are formed by hydrophilic groups which are hydrated in an aqueous medium [73, 74]. Typically, hydrogels are insoluble in aqueous solutions due to their polymeric cross-linking. However, the presence of abundant water molecules within the polymer network, facilitated by hydrogen interactions, enables these materials to swell in aqueous solutions [74]. Therefore, chemically, hydrogels can be characterized by two conditions: the presence of a water-insoluble polymeric chain and the inclusion of hydrophilic functional groups.

The two aforementioned requirements give rise to a wide range of hydrogel precursors. To facilitate the understanding of hydrogels, they can be classified based on several aspects. Firstly, hydrogels can be categorized according to their origin as either natural or synthetic polymers. Additionally, based on polymeric composition, hydrogels can be grouped as homopolymeric, where the basic structure consists of a single type of monomer, copolymer (composed of two or more different monomer species with at least one hydrophilic component) or multipolymeric interpenetrating polymeric hydrogels, which consist of two independent crosslinked polymers. Furthermore, hydrogels can be classified based on their crystallinity, such as amorphous, semicrystalline, or crystalline. Another classification criterion is the electric charge of hydrogels, which allows for grouping them into nonionic, ionic (including both cationic and anionic hydrogels), amphoteric (containing acidic and basic groups), and zwitterionic (including both anionic and cationic groups) hydrogels [74].

However, not all hydrogels can participate in photopolymerization. In 3DLL precursors hydrogels are usually liquid and should immediately respond to irradiation of light. Therefore, PIs which accelerate photopolymerization reactions are necessary. Multifunctional crosslinkers, such as acrylic acid or (meth)acrylates, create links between the polymeric chains. Frequently, monofunctional reactive dilutes are added in order to adjust the viscosity [75]. Photopolymerizable hydrogel precursors could be: HA-MA/acrylamide, modified gelatin, collagen, fibrinogen, fibronectin, concavalin A, lyophilized BSA (bivone serum albumin), PEGDA/HEMA and so forth, together with eligible PIs [75]. One of the most used hydrogels for several decades is PEGDA [76, 77]. Its structural formula is depicted in Figure 1.8. PEGDA consists of polyethylene glycol with two acrylates substituents at the ends of the chain. PEGDA is functionalized by polyacrylic or polymethacrylic acids in order to form crosslinked hydrogels. These compounds have an oxygen atom in a polyethylene glycol part and carboxylic group in an acid part. The hydrogen bond between these groups is formed. This behaviour depends on pH, because the reason for hydrogen bond formation is the protonation of carboxylic group [73]. However, properties of hydrogels can be changed not only by changing pH. Various factors, such as temperature, pressure, solvent composition or ions changes controllable, can influence crosslinking density, hydrophobicity, swelling rate,

permeability, degradability and mechanical strength [75] of gels which are important for 3DLL process and for the applicability of the final product.

The ability to polymerize hydrogels with 3DLL further extends their applicability [75]. Indeed, from most of the currently available materials they offer one of the best analogs for extracellular matrix. Thus, numerous different structures were created out of hydrogels over the years using 3DLL [45, 78–80].

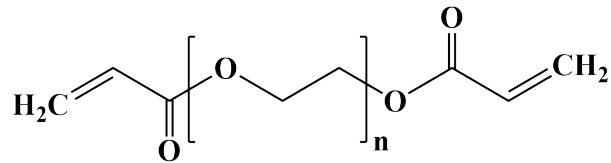


Figure 1.8: Structural formula of polyethylene glycol diacrylate (PEGDA). Here n is a degree of polymerization [A1].

1.5.3 Epoxy

SU-8 is the most popular epoxy-based photoresist, which can be polymerized *via* TPP. SU-8 is unique, as it possesses eight epoxy groups per monomer [81]. It is based on the acid-labile groups and the photo-acid generator [82]. This results in a rather strict processing protocol. First, it is pre-baked to remove the solvent. Subsequently, the material undergoes UV exposure, resulting in the generation of a strong, low concentration acid. One example is the decomposition of PI into hexafluoroantimonic acid, which then protonates epoxides. Such protonated oxonium ions are capable to react with neutral epoxides in cross-linking reactions after irradiation. During this process, acid regenerates resulting in a very strong reaction in exposed areas. This reaction is facilitated by the fact presence of eight epoxy sites on each monomer under typical conditions. [Figure 1.9]. The end result is very well-defined 3D objects that can be relatively big (up to cm) or can have very small features (down to tens of nm [83]).

3DLL processing of SU8 have some interesting features in comparison to standard UV case. First off, exposure and post-bake can be combined into a single processing step [84]. This is possible due to the capability to induce both: nonlinear absorption and subsequent heating during the same laser scanning step. The polymerization kinetics are also somewhat different. Raman spectra reveals that when SU8 is exposed to 800 nm 100 fs 1 kHz Ti:Sapphire the absorption dynamic is different from standard UV case. However, the end result is basically the same as SU8 polymerized with UV radiation and 2PA has nearly identical Raman spectra [85]. Both sub-diffractive structures [86] and mm scale objects [87] were fabricated using 3DLL out of SU8. Due to

relatively good adhesion of SU8 to various functional substrates, structures can be printed directly on them. One of the examples - fiber tips [88]. SU8 consists only of the organic matter, therefore it can also be removed by calcination in ambient atmosphere in rather low temperature of 600 °C, making it a good candidate for the template material for other substances that are hard to shape in 3D directly [89]. This epoxy-based resist is transparent to visible light and highly resistant to traditional solvents, making it suitable for many applications such as microfluidic, photonic and biomedical structures [81].

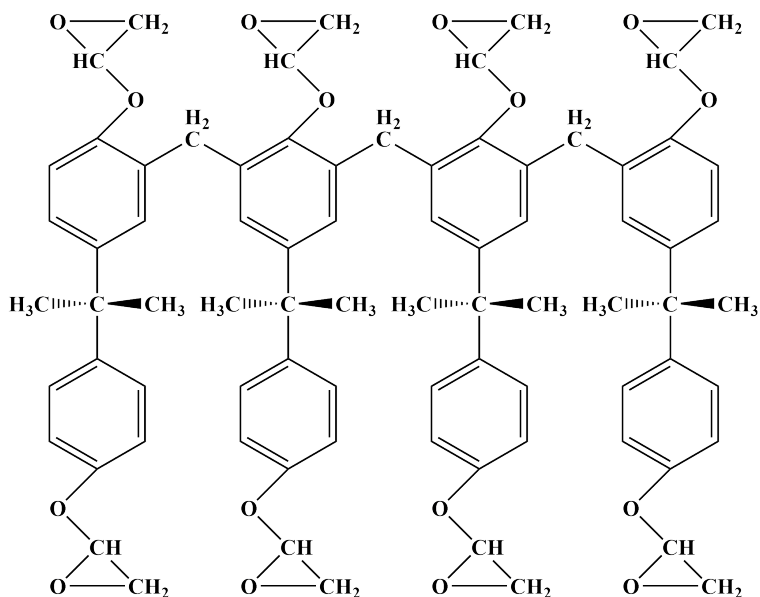


Figure 1.9: Molecular formula of SU8 monomer [A1].

1.5.4 Hybrid metal-organic materials and suspensions

Hybrid metal-organic prepolymers are exceptional materials for 3D laser printing applications. These compounds possess remarkable properties that make them highly suitable for fabrication, including photosensitivity to radiation, transparency, and homogeneity. Moreover, 3D structures manufactured from hybrids can be transformed into glass-ceramic or crystalline materials through heat treatment. These ceramic structures exhibit excellent mechanical, thermal, and chemical properties, making them highly promising as engineering materials.

Most hybrid preceramic polymers are metal-organic compounds derived from silicon, with additional backbone chains consisting of carbon (C), nitrogen, oxygen (O), boron (B), or metal atoms such as Hf, Zr, Al, Ti, Ge, V, Ce, Mo, Sn,

Fe, Co, Ni, Pd, Pt, Cu, Ag, Au, W and etc [90]. The backbone of these polymers is linked to side groups, which are predominantly organic. Common types of side groups include alkyl, vinyl, aryl, epoxy, and various other organic groups that can participate in photopolymerization (Figure 1.10) [91].

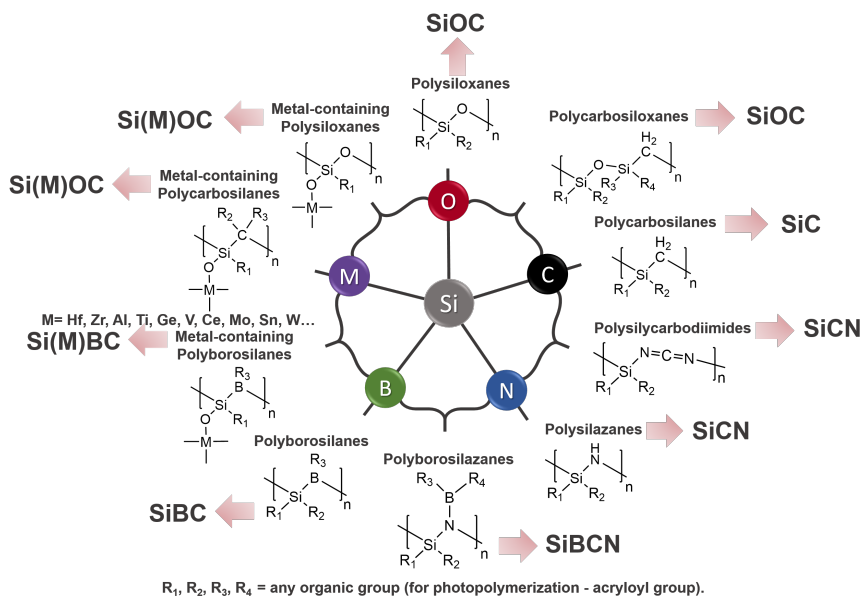


Figure 1.10: Possible common types of silicon-based hybrid organometallic polymers in the Si-Me-O-C-N-B system used as precursors for ceramics [B1].

In addition to homogeneous hybrid materials, suspensions are also utilized to obtain functionally structured ceramics. Generally, suspensions consist of fine ceramic particles dispersed in liquid or semi-liquid systems, serving as a feedstock or metal-organic resins, often in the form of inks or pastes. Suspensions are based on metal or semimetal oxides, carbides, borides, nitrides, glass grains dispersed in organic monomers, such as oxymethylene, olefins, propylene or ethylene, urethanes, amides, ethers, esters, acrylates (Figure 1.10) [92].

However, suspensions present several disadvantages compared to hybrid organometallic monomer resins. Structures made from suspensions have limited resolution due to the particle size and light scattering tendencies. Additionally, it is challenging to maintain stability in a mixture of substances over an extended period. Moreover, structures tend to exhibit disproportionate shrinkage and develop porosity or defects after heat treatment. The following light-based methods used in additive manufacturing for such materials formation are commonly: stereolithography (SL)- digital light processing (DLP) and two-photon polymerization (TPP), along with inkjet-based printing (IJP) and

extrusion-based direct ink writing (DIW) [92], [93]. Indeed, the most promising method for obtaining high resolution 3D ceramics is laser two-photon polymerization of hybrid materials with subsequent pyrolysis [A2].

Laser two-photon polymerization technology offers the advantage of being compatible with a wide range of materials [A1]. The requirements for materials suitable for two-photon polymerization are minimal: they need to be transparent to the laser wavelength and possess the characteristics necessary for multiphoton absorption triggering photopolymerization [94, 95]. To enable the conversion of the produced structures into pure inorganic ceramics through pyrolysis, the chemical composition of the materials must include inorganic components. Such materials can be suspensions containing inorganic nano/micro-particles or hybrid metal-organic prepolymers, as discussed in the previous paragraph and illustrated schematically in Figure 1.10. Among the various synthesis methods, the sol-gel method is the most suitable and extensively studied technique for producing hybrid materials [96].

In brief, the sol-gel process entails preparing a precursor mix (a sol or a solution), which transforms into a more solid-like substance upon evaporation of the solvent and chemical cross-linking of its solid, liquid, or dissolved components [97]. Sols or solutions can often be transformed into ceramics through gel-like intermediates at temperatures that are significantly lower than the ones employed in traditional processing [96]. This occurs because the precursors used are intermixed at a molecular level and can react further to form a network.

In order to enhance comprehension of the synthesis methodology, Figure 1.11 is presented as an example [98]. The sol-gel process begins with the stabilization of metal or semimetal alkoxide by organic molecules. In the case of photocurable metalorganic resist synthesis, organic acid having acryloyl group (for example, methacrylic acid) should be added to produce stable, photo-active precursors, necessary for photopolymerization. Stabilization is carried out slowly adding the organic acid to the alkoxide. After stabilization, hydrolysis is performed. During hydrolysis, water reacts nucleophilically with metal alkoxide to form hydroxide groups through the alkoxy groups contained in the metal alkoxide precursor. Acids or bases are used as catalysts for these reactions. The way the reaction occurs and its kinetic properties are principally influenced by the catalyst, the nature of the alkoxide group and the solvent used. Stabilized and hydrolyzed alkoxides of metals or semi-metals are added dropwise to each other. Typically, the alkoxide of the more active metal is added dropwise to the more passive one, thus forming a liquid solution- sol. The natural phenomenon that follows hydrolysis of alkoxide precursors is condensation (also called polycondensation or inorganic polymerization). In this process, hydroxyl groups react with each other to form oxo bridges (-M-O-M-) in combination with the simultaneous elimination of either a water or alcohol

molecule [98–100]. In the presence of solvents and alcohol formed after hydrolysis, the condensation is accelerated by heating ($\sim 90^\circ\text{C}$). After condensation gels become sufficiently rigid and transparent, so they can be polymerized with appropriate radiation [99]. Additionally, appropriate photoinitiator may be added to the sol.

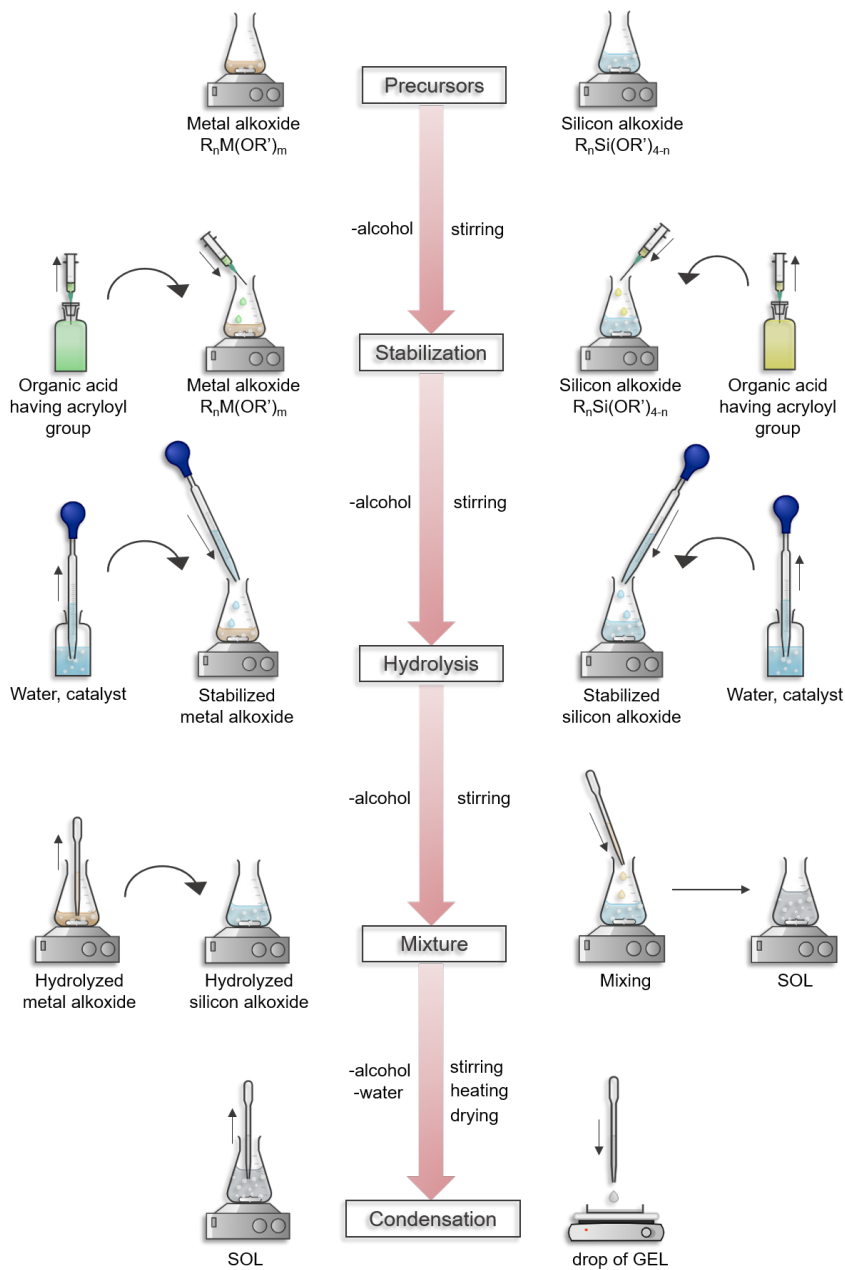


Figure 1.11: Scheme of sol-gel synthesis of silicon-based organometallic prepolymer for laser photopolymerization [B1].

1.6 Positive photo-resists

All photopolymers discussed so far are of so called negative photo-resists. It means that areas which were exposed to the light are crosslinked and remain after the development. However, opposite also can be realised by using so called positive photo-resists. In that case under irradiation exposed regions of photosensitive material are removed by the developing. Typically, positive resists consist of the polymer matrix, photoactive generator, solvent and other additives [101, 102]. The main requirement of such resist is photosensitivity of photoactive generator which is basically called photoacid generator due to its property to produce acid after the light irradiation. The photoactive generators can be divided into two types, first - the ionic, which mostly contain onium salts and upon UV light are able to produce Brønsted acids, while the second type is non-ionic that can generate sulfonic, carboxylic and phosphoric acids. Generally, polymers having tertiary carboxylate, tertiary carbonate, tertiary ether, acetal, hemiacetal ester or other easily protonizable group are used in positive tone resist systems. In that case after the photo-activated acid-catalyzed reactions such polymers are decomposed into poly-carboxylic acids or poly-phenols [101], depending on the initial functional group, and the compounds with smaller molecular weights. Thereafter, polymers having acidic functional groups can easily dissolve in alkaline solvent. The described system is called the amplification resins. The most prevalent type of positive tone photoresist consists of diazonaphthoquinone (DNQ), phenol formaldehyde polymer (Novolac), and propylene glycol monomethyl ether acetate (PGMEA) as a solvent [103–106].

Positive tone resists were applied in 3D laser lithography [107] with primer focus on possibility to use them in microfluidics [108]. However, they are relatively chemically unstable with short shelf life and narrow fabrication window. Thus, in recent years they were used less and less in favour of easier to use and apply negative tone resist.

1.7 Thermal post-processing technique for 3D nanostructures

Typically, hybrid organometallic 3D objects exhibit mechanical properties that are comparable to those of organic structures [109, 110]. However, hybrids possess a distinct advantage - they can undergo a transformation into pure inorganic amorphous, glassy, or crystalline structures [111, 112],[A2]. As a result, the potential applications of such structures expand significantly. In this section, the subsequent steps involved in post-processing 3D hybrid structures in order to achieve either inorganic-amorphous or crystalline structures (refer to Figure 1.12) will be described. To illustrate the processes, we will take the well-known and widely used material SZ2080TM [113].

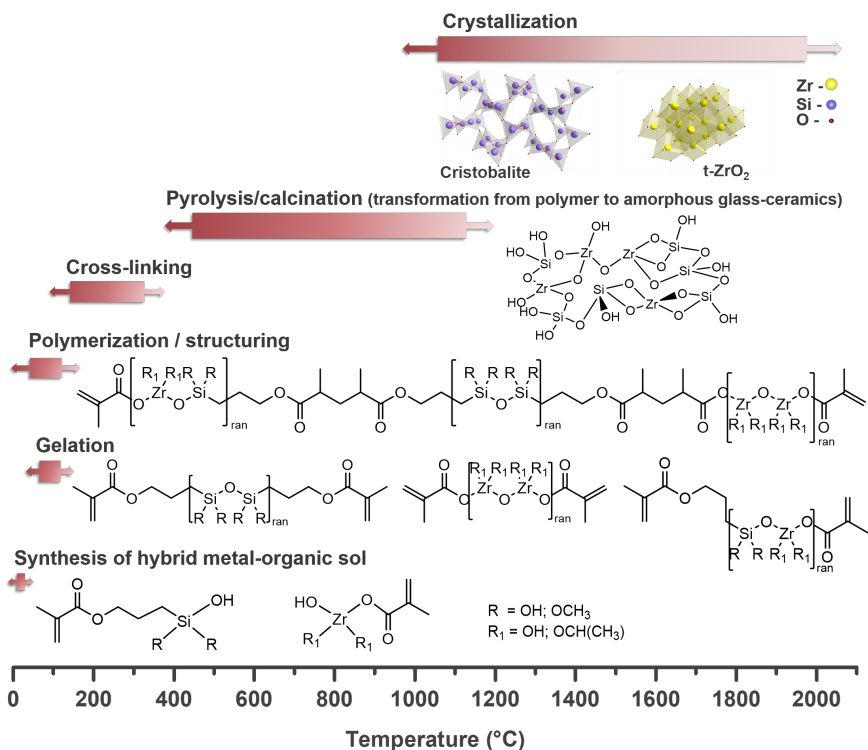


Figure 1.12: Steps from synthesis to crystallization in Si-Zr organometallic system. Chemical structures and crystal lattices were reproduced from [111].

The transition of SZ2080TM from polymer to an amorphous glass-ceramic was investigated and described by Gailevičius et al. [111]. This study was continued by Merkininkaitė et al. [A2]. The results are described in Chapter 3.

In order to preserve the structural integrity of the object following heat treatment, it is essential to carry out the processes of polymerization and cross-linking. Based on the chemical nature of precursors, cross-linking reactions can be initiated in different ways: exposure to light or laser curing (the described case of photopolymerization), thermal treatment (150 °C - 400 °C), electron-beam curing and reactive plasma initiation for cross-linking at low temperatures (<200 °C) [114]. Thermal cross-linking after photopolymerization is the most attractive and best-studied for hybrid metal-organic materials. This technique induces hydrosilylation (Si-H/vinyl groups), transamination (evolution of amines, ammonia or oligomeric silazanes), thermal polymerization (vinyl or allyl groups) and dehydrocoupling (Si-H/Si-H or Si-H/N-H groups) reactions causing the formation of organic/inorganic networks [91, 112] and structure densification.

Pyrolysis is a thermal treatment conducted at temperatures exceeding

400 °C, wherein polymers undergo decomposition, ultimately resulting in the formation of amorphous inorganic compounds. Calcination and crystallization, being high-temperature treatments, initiate subsequent reactions. The properties of 3D objects after heating, including chemical composition, density, defects population, surface morphology, and crystallinity, are not solely influenced by the composition of the initial material. They are additionally affected by factors such as the heating temperature and its ramp rate and holding time, as well as the heating atmosphere, whether it is under overpressure or in a vacuum [115]. During the pyrolysis step, less stable organic compounds decompose resulting in objects initial weight loss up to $\approx 30\%$ [26], and linear shrinkage $\approx 40\%$ [111]. Most of the precursors (individually for each composition) reach amorphous glass/ceramic up to 1100 °C and crystallization begins at higher temperatures (typically from 1200 °C). In an oxidizing atmosphere, organic material is eliminated in the form of CO and CO₂ gas. Therefore, it is crucial to control the rate of temperature increase in order to prevent the formation of porosity in the structure. In this case, the predominant outcome involves the formation of metal or semi-metal oxides as depicted in Figure 1.12. The formation of free carbon, carbides, or nitrides occurs through chemical reactions that take place during the heat treatment process in an inert atmosphere, such as argon (Ar), nitrogen (N₂), or under vacuum conditions [91].

In summary, the optimal conditions for polymer-to-ceramic conversion extensively depend not only on the original precursor composition but also on the atmosphere, heating rate and temperature.

1.8 Trends and technical applications

This section presents the most promising trends and fields of application that derive direct benefits from the distinctive mechanical, optical, and chemical properties exhibited by 3D structures with sub-100 nm scale. These objects assume critical role in facilitating advancements in numerous domains.

Currently, thermal post-treatment is being established as a technique for downscaling or improving the properties of the laser additive manufactured 3D nanostructures. For instance, pyrolysis is applied at 900 °C for production of carbon nanowires, resulting in downscaling the features and converting the compound into a new substance [116]. In another study, a pre-ceramic resin was developed and investigated for its application in two-photon lithography, with the aim of fabricating crack-free objects characterized by bulky and free-form objects [117], yet the systematic feature size (resolution) study was not performed in details, making the results difficult to evaluate or compare.

On the other hand, some inorganic tin oxide ceramics were 3D structured *via* a similar femtosecond laser 3D photolithography technique followed by sintering, it showed a promising route for high resolution additive manufac-

turing. Yet the obtained spatial resolution was $\approx 1 \mu\text{m}$ in linewidth [118]. Another study presents a robust method for additive manufacturing of ductile, ultrastrong silicon oxycarbide (SiOC) ceramics at previously unprecedented scales using two-photon polymerization direct laser writing (TPP-DLW) of a preceramic resin, offering the potential to fabricate engineering systems with feature size $\approx 200 \text{ nm}$ [119].

The latest research towards applications in photonics was focused on creating high refractive index materials, such as TiO_2 . The 300-600 nm spatial resolution was demonstrated [8]. In general, metal oxide ceramics are important in both modern technology and commercial applications. This was demonstrated by applying lithium-cobalt oxide 3D structuring suitable for cathodes into lithium ions batteries [120].

All in all, applications can range from micro-optics to micromechanical systems operated in harsh environments requiring toughness and stability. The technical applications are separated into these sub-topics: micro-optics, nanophotonics, micro-/nano-fluidics, micro-mechanics, and nano-electronics. The following section presents and discusses the significant details of the current milestone achievements.

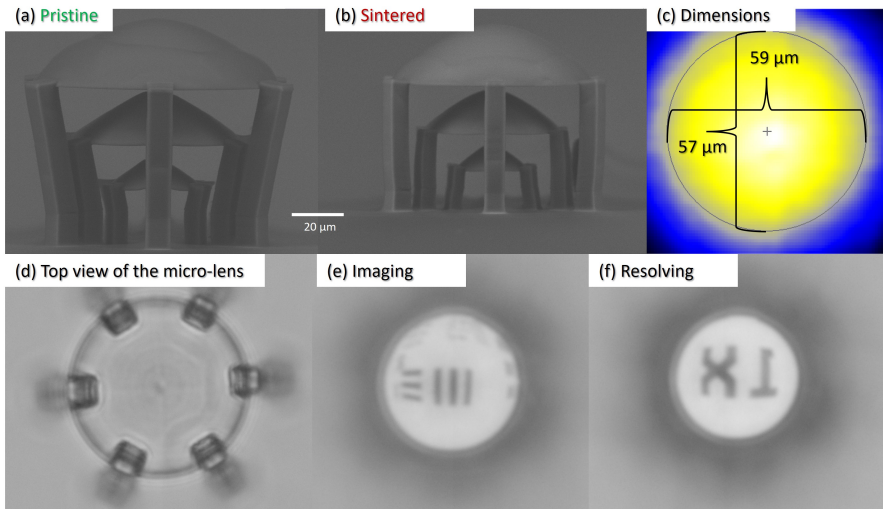


Figure 1.13: An SEM image of micro-optical component stacked of 3 aspheric lenses: (a) pristine and (b) sintered. Geometrical characterization of the single lens diameter by optical profilometer - (c), and its top view under OM (d). Validation of the same calcinated micro-lens imaging and resolving properties using 1951 USAF test target - imaged group 6 element 7 corresponds to the resolution of $4.39 \mu\text{m}$ (228 lp/mm). As shown, the geometrical and material properties such as projected lens shape and optical transparency are preserved for quality functional performance. Figure adapted from [7].

1.8.1 Micro-optics

Recently, a pilot study on laser 3D printing of inorganic free-form micro-optics was experimentally validated [7]. Ultrafast laser nanolithography was employed for structuring hybrid organic-inorganic material SZ2080TM and followed by high-temperature (~ 1000 °C) post-processing. The process allowed production of true 3D architectures and subsequent heat-treatment resulted in material conversion to a transparent inorganic glassy material. Miniature optical elements were produced and characterized. Also, their optical operation was demonstrated. The preliminary measuring indicated the averaged value of refractive index ≈ 1.609 , which matched well with the $n = 1.617$ as reported for non-structured material in literature [121]. Finally, the concept was validated for manufacturing of micro-optical components stacked of 3 aspheric lenses (see Figure 1.13). This is extremely attractive for the implementation of DLW lithography-made glass optics in material processing, remote sensing, and astrophotonics [7].

1.8.2 Nano-photonics

Additive manufacturing at a small scale enables advanced in 3D nano-photonics systems. However, the choice of high-refractive-index materials is limited. Recently was produced process to fabricate complex 3D architectures out of dense titanium dioxide (TiO_2). These objects were characterized by a high refractive index ($n = 2.3$) and nano dimensions, required for nano-phonic devices. The transmission electron microscopy analysis proved this material to be a crystalline rutile (TiO_2) phase. SEM analysis shows grain formation with an average size of 110 nm and $< 1\%$ porosity. Proof-of-concept woodpile 3D architectures with 300–600 nm beam dimensions exhibited a full photonic bandgap centered at 1.8–2.9 μm , as was revealed by Fourier-transform infrared spectroscopy and matching with a plane wave expansion simulations [122]. The complete protocol and resulting structures are shown in Figure 1.14.

1.8.3 Micro-fluidics

Micro-fluidics is another field that is greatly benefiting from the true 3D shaping of glass structures. The fabrication of arbitrary three-dimensional suspended hollow micro-structures in transparent fused silica glass are presented. A micro-fluidic 3D intertwined mixer is shown in Figure 1.15. The reported results were achieved by mixing SiO_2 nanopowder in the organic binder resin instead of sol-gel chemistry derived hybrid photopolymer [123]. Here researchers utilized complex organic polymeric templates created by direct laser writing. The templates were embedded in a SiO_2 nanocomposite material, which was then polymerized and transformed into fused silica glass through

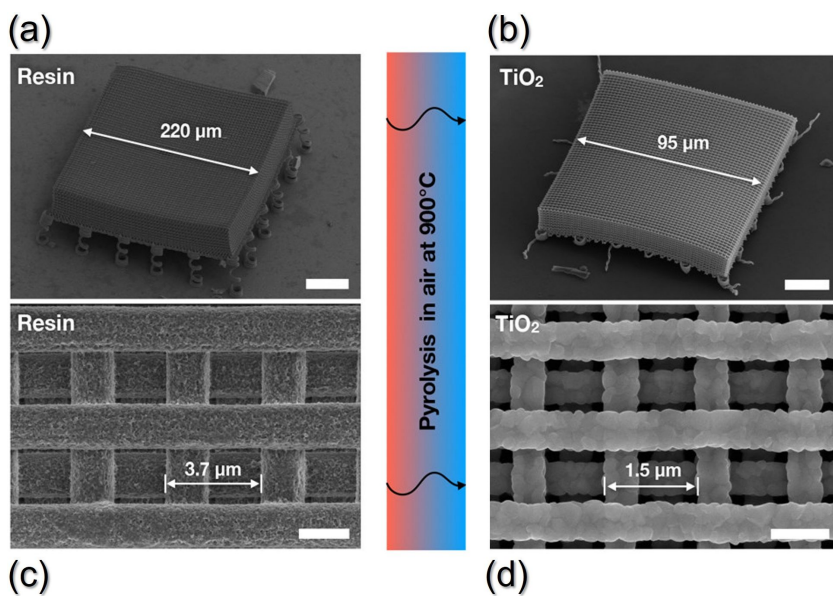


Figure 1.14: Schematic representation of laser additive manufacturing of TiO_2 3D nano-architectures by SEM images. (a) Woodpile architectures were supported by a set of springs that decouple them from the substrate. (b) Titania woodpile structure was formed by calcination of the preceramic part. Representative TiO_2 magnified view before (c) and after (d) calcination at 750 - 900 °C. Figures scale bars correspond to: (a) - 50 μm , (b) - 20 μm , (c) and (d) - 2 μm . Reprinted with permission from [122]. Copyright (2023) American Chemical Society.

thermal debinding and sintering processes. The removal of the polymeric templates during the debinding stage resulted in hollow cavities without material redeposition or channel blockages. This technique allows for precise control over the structure geometry [123].

The sintered fused silica glass parts demonstrated high optical transparency across the UV, visible, and infrared regions, as well as mechanical, chemical, and thermal stability. The surface properties of the glass, such as hydrophilicity and surface energy ($\approx 60 \text{ mN m}^{-1}$), resembled those of commercial fused silica glass. Overall, this technique for fabricating three-dimensional suspended hollow microstructures in fused silica glass using sacrificial templating has significant potential for applications in flow-through synthesis, microfluidics and lab-on-a-chip devices.

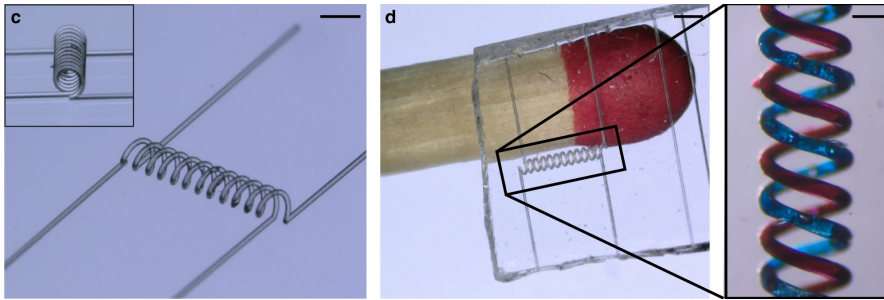


Figure 1.15: Glass templates produced by DLW and thermal treatment: (c) Intertwined spirals (scale: 900 μm). (d) Resulting intertwined microfluidic spiral channels in fused silica glass with a channel width of 74 μm . The channels were filled with dyes (see inset, scale: 140 μm). As it can be seen the 3D structures can be replicated with high accuracy and no deformations [123].

1.8.4 Micro-mechanics

Ultrafast DLW multiphoton lithography opened a new dimension for the mechanical material engineering based on nano-architected additive manufacturing [124]. High-porosity (low mass density) objects with optimized internal 3D geometries in combination with thermal treatment enable the production of ductile, ultrastrong polymer-derived nanoceramics [125]. As an example, mechanical performance in SiOC nanograting is shown in Figure 1.16. This nanograting is characterized as mechanical metamaterials with exceptional stiffness and strength properties. When subjected to uniaxial compression, their effective stiffness varies between 1 and 17 GPa, while their strengths span the range of 40 to 860 MPa. These mechanical properties are observed across relative densities ranging from 9% to 40%. Moreover, the nanograting demonstrates elastic-plastic behavior, with failure strains reaching up to 8%.

Recently, L. Brigo et al. (2018) showed that using commercial resist, 3D complex architectures with size of the order of 0.10 mm in the z-direction and with details down to 450 nm can be fabricated with 2 photon polymerization. The achieved structures, after pyrolysis, were dense ($1.98 \pm 0.02 \text{ g/cm}^3$) and fully transformed into SiOC. The mass loss of such structures was as high as 90%, the linear shrinkage was greater than 50% [126].

L. Yao et al. (2022) demonstrated a photocurable SiOC-based slurry which was developed with 20 μm printing accuracy. Fabricated gyroid metamaterials exhibited attractive mechanical properties: the specific compressive strength was as high as $63.0 \text{ MPa}/(\text{g/cm}^3)$ with 0.606 g/cm^3 density [127]. While E. Shukrun (2018) showed the fabrication of 3D-printed organic–ceramic complex hybrid structure with 139 MPa hardness [128]. These recent studies confirm the increasing interest in ceramic metamaterials with improved mechanical

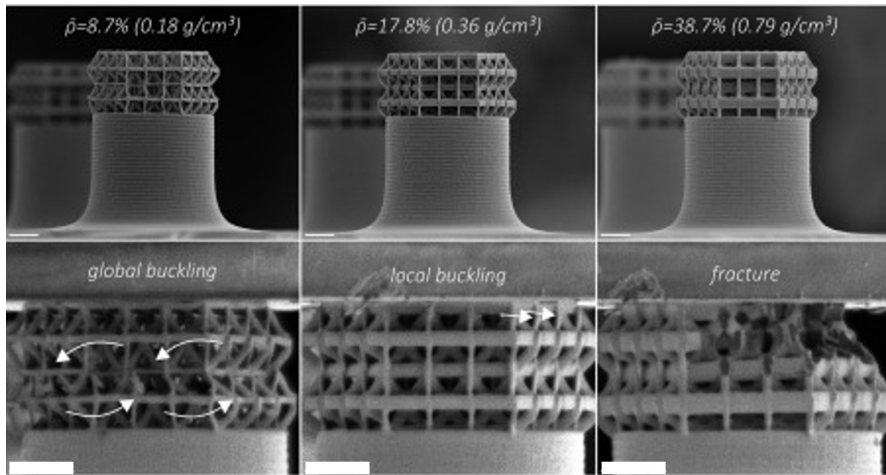


Figure 1.16: Mechanical characterization of SiOC nanolattices: 3D structures before mechanical characterization (top) and at the moment of failure (bottom). Scale bars are all 5 μm [125]. Reprinted with permission from Elsevier. Copyright ©2023 by Elsevier.

properties.

Comparison of hardness and/or compressing failure strengths of 3D inorganic or hybrid organic-inorganic structures prepared by additive manufacturing is depicted in Figure 1.17. It is clear that the hardness demonstrated in many studies are limited to the megapascal (MPa) scale. Only the last studies show hardness in the gigapascal (GPa) scale. The recent studies demonstrating hardness in the GPa scale reflect the availability of new advanced materials and the emergence of research areas that demand materials with higher hardness properties.

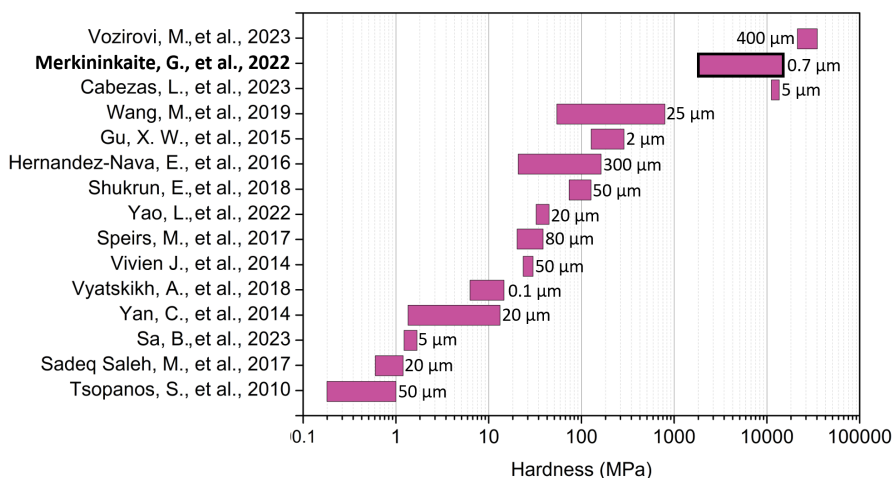


Figure 1.17: Comparison of the hardness of 3D inorganic or hybrid organic-inorganic structures prepared by additive manufacturing [11, 127–139] and [P1]. The achieved sizes of dimensions are provided. The result published in the thesis approbation patent [P1] is highlighted.

1.8.5 Nano-electronics

For true 3D micro-/nano-electronics applications conductive microstructures containing gold can be fabricated by simultaneous photopolymerization and photoreduction DLW and pyrolysis. E. Blasco et al. have reported employing a photoresist consisting of water-soluble polymers and a gold precursor. The fabricated microstructures demonstrated good conductivity and were successfully deployed for 3D connections between gold pads [140]. Ultrafast laser 3D lithography, combined with calcination, is a rapidly emerging field that is still being studied for its feasibility. However, it has already demonstrated its potential by successfully creating functional prototypes like ZnO-based UV photodetection devices with a large current on/off ratio and excellent cycling stability [97]. This is of crucial importance for next-generation MEMS/NEMS, and energy storage devices.

1.8.6 Sub-100 nm challenges: comparison of current achievements

The ability to fabricate structures with sub-100 nanometer resolution using 3D direct laser writing has far-reaching implications in various fields of research and technology. It drives advancements in photonics, enabling the development of advanced photonic devices and integrated optics. The successful attainment of nanoscale dimensions using laser lithography as a

standalone technique still presents challenges from a scientific perspective.

Sub-100 nm features can be fabricated using the stimulated emission depletion (STED) technique, or by employing post-processing methods. STED requires a more sophisticated two-wavelength laser setup and materials prepared for that specific lithography [141, 142], yet not for their functionality. Current achievements of sub-100 nm features via STED lithography are shown in Figures 1.18(c-e)[142, 143]. Plasma etching has proven to be effective in refining the features of fabricated structures, enhancing their quality and precision (Figure 1.18g). On the other hand, pyrolysis/calcination not only enables downscaling of the structures (Figure 1.18(h-j)) but also facilitates the transformation of the material into inorganic, rendering it highly advantageous for a wide range of technical applications. However, as depicted in Figure 1.18(j), it is evident that achieving nanoscale dimensions is feasible without the use of STED technique. Therefore, there is no requirement for upgrading the setup to a multi-wavelength exposure configuration. Finally, the calcination route ensures complete material conversion to inorganic, thus removing the photoinitiator in case it was used in the photoresin [7].

In Figure 1.19 essential publications in the DLW 3D lithography of inorganic material are marked and dated accordingly. As an important criterion, the reports are ranked in resolution (feature dimension), specifically on sub-100 nm scale. Another plot represents the growing number of citations which shows increasing interest in the field. It is noted, that during recent years the amount of original publications increases and the density of the achievements concentrates towards the 100 nm benchmark, with sub-100 nm being repeatedly reached.

1.8.7 Emerging applications

Appendix table A.11 summarizes the current achievements where DLW 3D lithography was used in combination with thermal post-treatment: reference, year, materials used, details of processing protocol, achieved dimensions, and targeted applications. As it is seen, various femtosecond laser setups of different wavelengths (515 nm, 780-800 nm), pulse durations (100 fs, 300 fs), as well as repetition rates (200 kHz or 80 MHz), were used. It can be deduced that the dimensions of a three-dimensional (3D) objects are influenced not only by the fabrication parameters but also by the specific material properties and an optimized calcination protocol. It should be noted, that not all researchers were aiming for the highest resolution, rather for the specific application. On the other hand, supporting techniques such as helium-assisted microcasting can be used for employing hollow polymer templates for filling it with glass slurry and sequentially removing the template completely [190]. This results into fused-silica structures where the laser 3D structured polymer serves just as a sacrificial structure. Hence, the accomplishments of scientific research in micro-

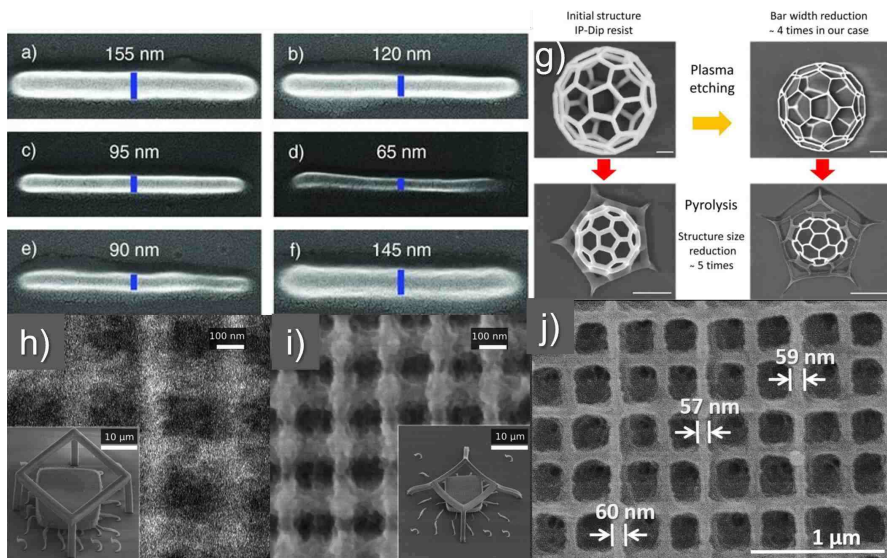


Figure 1.18: Current achievements of sub-100 nm features *via* STED lithography ((a) - (f)), plasma and pyrolysis assisted post-processing solutions (g), (h) - (j), and inorganic structures obtained *via* calcination approach. A note, that STED technique allowed achieving of 65 nm features of organic materials as shown in (d), yet further variations of depletion power resulted in enlargement of the primitive structures (e) - (f). In (h) a lattice structure out of SZ2080™ before and (i) after calcination is shown, with line widths reaching below 100 nm already in inorganic glass-ceramic material. Whereas with the material tuned for inorganic substance outcome results in reproducibly reached 60 nm homogeneous lines in a well ordered lattice geometry, shown in (j). Scale bars represent 1 μm in (g). [111, 141, 144], [A2].

and nano-scale ceramic make a substantial contribution to the technology industry.

Figure 1.20 depicts properties of 3D ceramics, their immediate possible and future potential technical applications. Certain applications necessitate distinct requirements for thermal conductivity, chemical reactivity (inertness), optical properties, mechanical, and electromagnetic characteristics. Described characteristics are compatible with the technology's capability of making multi-material polymer 3D objects [191], thus empowering to make multi-material inorganic-organic or inorganic-inorganic structures [145].

Finally, the eco-innovative aspect based on plant-derived optically 3D printable resins allows merging bio-renewable resources with the discussed calcination method - as the organic matter is only used for templating and is evaporated eventually, thus it can allow selection of bio-based resins (such as derived from vegetable oils for instance) instead of petroleum ones [192]. As an

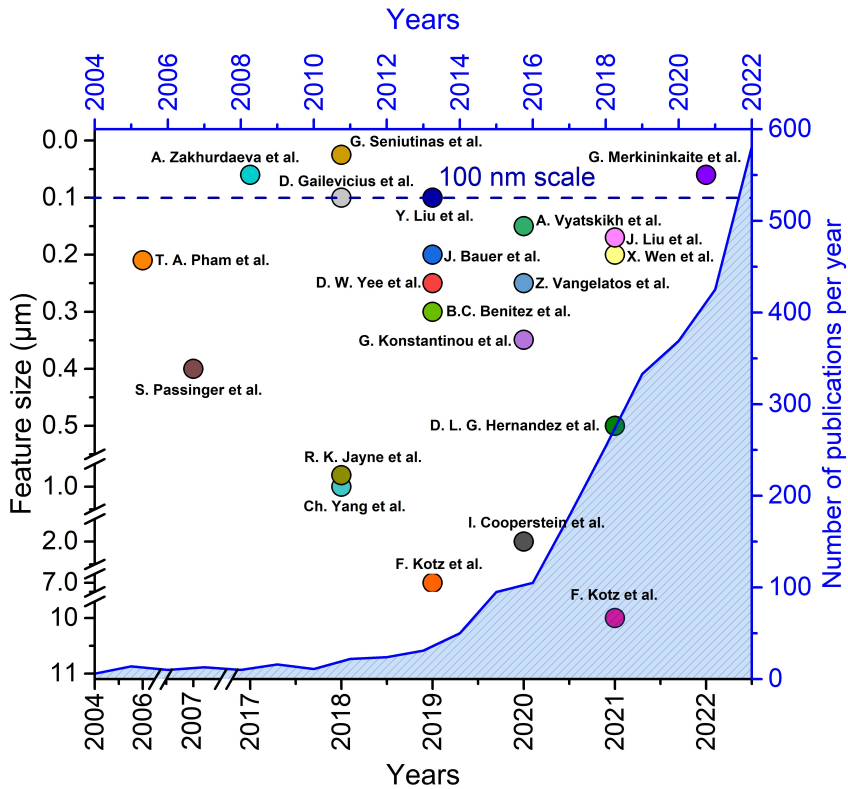


Figure 1.19: Current achievements of 3D inorganic structure resolution in 3D lithography (corresponds to the black coordinate axis) and the number of publications per year (corresponds to the blue coordinate axis). The number of publications resulting from a search with keywords "3D, ceramic, printing" on scopus.com website, from 2004 to 2022 [7, 97, 111, 122, 123, 125, 144–157]. The achieved feature size of G. Merkininkaite et al. (up to 60 nm) is published in article [A2] of the thesis approbation.

example, a resin based on AESO (acrylated epoxidized soy oil) and a natural diluent such as ethyl lactate can possess a renewable carbon content of up to 89%. Furthermore, this resin can be manufactured across a wide range of sizes, spanning from sub-micron to millimeter dimensions [193].

1.9 Summary and outlook

In conclusion, recent advances in ultrafast DLW lithography and its application for additive manufacturing of 3D inorganic nano-objects have shown significant progress. The ability to fabricate complex architectures and

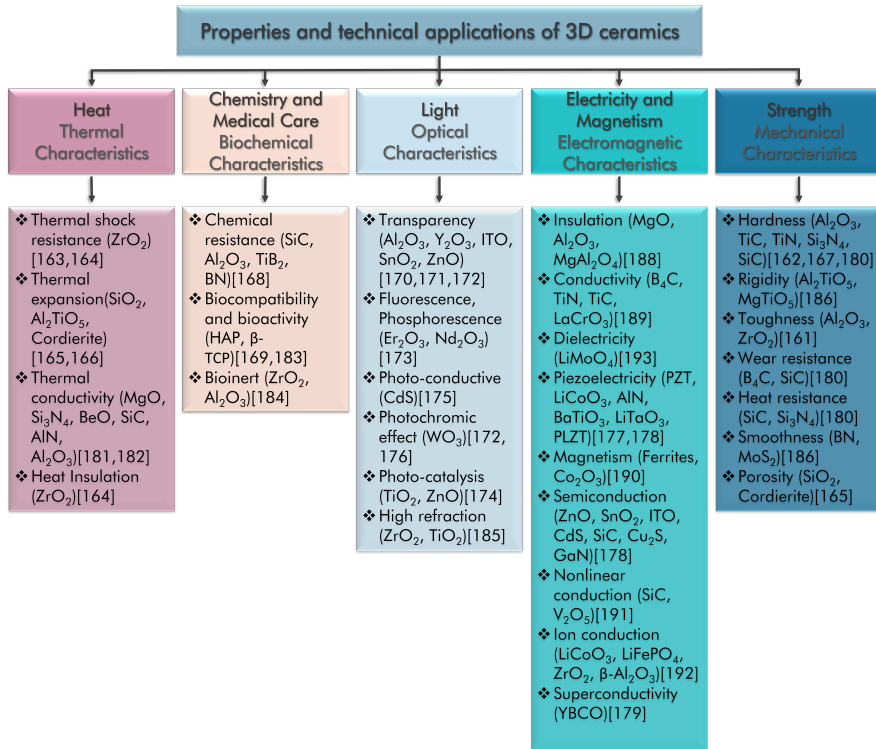


Figure 1.20: Properties of 3D ceramics, their immediate possible and future potential technical applications [158–189].

true glass, ceramic, and crystalline structures through precision optical 3D printing of hybrid organic-inorganic materials followed by high-temperature thermal post-treatment is a notable achievement.

The synergistic progress in laser technology and material sciences have already resulted in immediate applications in various fields such as microoptics, nano-fluidics, micro-mechanics, and nano-electronics.

Moreover, this technology has established a reliable route for downsizing structures, addressing the challenge of reaching below 100 nm features. By achieving a 40-60% feature reduction without compromising geometry, DLW 3D nanolithography enables the production of complex shaped geometries with the highest optically true 3D printable resolution. The material densification during sintering offers benefits such as surface self-smoothing, which is crucial for applications in micro-optics, nanophotonics, and fluidics.

However, it is important to note that the field of technology of precise 3D ceramics is experiencing rapid advancements and progress at an accelerated pace. Therefore, the quest for suitable hybrid precursors that are compatible

with laser 3D polymerization remains an urgent and timely task. This is primarily due to the fact that the formation of three-dimensional (3D) ceramic objects at micro- and nano-dimensions through laser lithography heavily rely on the chemical precursors nature.

2. EXPERIMENTAL

2.1 Materials and synthesis methods

2.1.1 Synthesis of Si/Zr metalorganic precursors

Photoactive monomers were synthesized by the sol-gel method according to the synthesis described in 2008 [194]. 3-(Trimethoxysilyl)propyl methacrylate (MAPTMS, Sigma Aldrich, 98%), zirconium(IV) propoxide solution 70 wt. % in 1-propanol (ZPO, Sigma Aldrich) and 2-methacrylic acid contains 250 ppm MEHQ as inhibitor (MAA, Sigma Aldrich, 99%) were selected as precursors for the preparation of the preceramic photopolymer. Methacrylic acid was vacuum distilled in order to remove the inhibitor. Other reagents were used without further purification. First, MAPTMS was hydrolyzed using aqueous HCl (0.1 M) solution at a 1:1 molar ratio (Figure 2.1 (I)). After half an hour of stirring, the solution of alkoxysilane and water becomes homogeneous, indicating the successful hydrolysis of the alkoxysilane groups.

Simultaneously, ZPO was stabilized by MAA at a 1:1 molar ratio (Figure 2.1 (II)). After that, hydrolyzed MAPTMS was added dropwise to the stabilized ZPO solution to form a liquid sol. The photoinitiator was not used. After stirring for 12 h in a sealed vial, the material was filtered using a 0.22 μm syringe filter. One series of Si_X:Zr_Y metalorganic precursors were synthesized, where X is Si molar ratio from 9 to 5 and Y is Zr molar ratio from 1 to 5. Five samples were prepared by adding drops of precursors on substrates. After that, drops were dried on a hotplate at 90 °C degree for 1 hour in order to form gels (Figure 2.1 (III)). After condensation, polymerization can be performed (Figure 2.1 (IV)).

2.1.2 Synthesis of silicon-organic precursors

The series of silicon-organic compounds were also synthesized via the sol-gel method using two silanes. Trimethoxymethylsilane (MTMS, $\geq 98.0\%$ Aldrich), possessing a 1:1 ratio of carbon and silicon atoms after hydrolysis and complete condensation. 3-(trimethoxysilyl)propyl methacrylate (MAPTMS, 98% Aldrich)

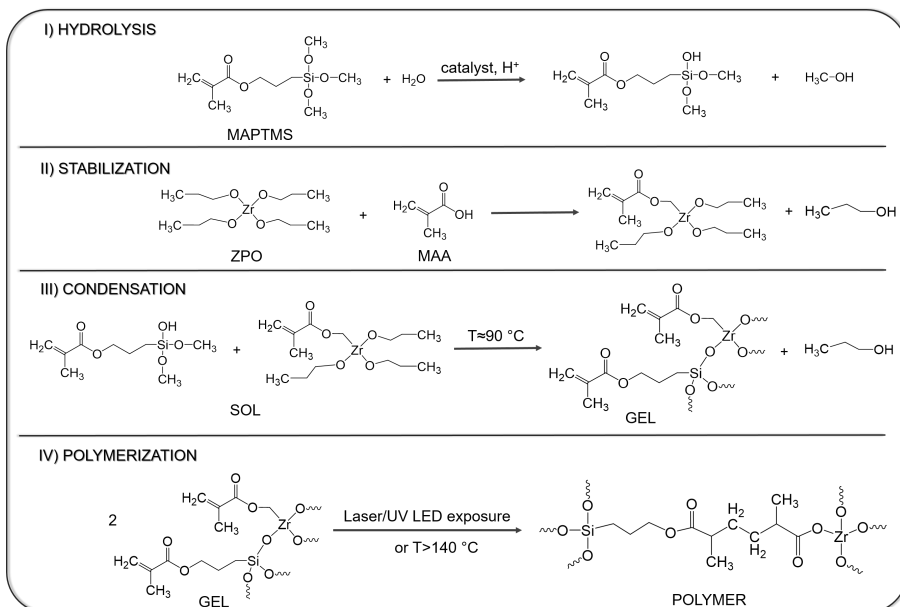


Figure 2.1: Flowchart of material synthesis and photopolymerization via following steps: hydrolysis of MAPTMS (I), stabilization of ZPO (II), mixing and condensation case of 1:1 molar ratio) (III) and polymerization (IV).

is well known and widely used in 3D laser lithography. A series of samples were prepared using 9:1, 8:2, and 7:3 molar ratios of MTMS and MAPTMS. Firstly, MAPTMS and MTMS were hydrolyzed separately using an aqueous HCl (0.1 M) solution at a 1:1 molar ratio (see Figure 2.2 (I) and (II)). The solution of alkoxy silane and water becomes homogeneous after 30 min of stirring indicating the successful hydrolysis of the alkoxy silane groups. During the next step hydrolyzed MAPTMS was added dropwise to the hydrolyzed MTMS solution. Lastly, the photoinitiator 2-benzyl-2-dimethylamino-1-(4-morpholino phenyl)-butanone-1 (IRG) was added giving a 1% wt/wt concentration to the final material. After stirring for 12 h in a sealed vial, the material was filtered using a 0.22 μm syringe filter. Before photopolymerization a drop of sol was placed on the substrate and dried on a hotplate at 50 °C for 1.5 h in order to form a gel, see Figure 2.2 (III). After condensation, photopolymerization can be carried out (Figure 2.2 (IV)).

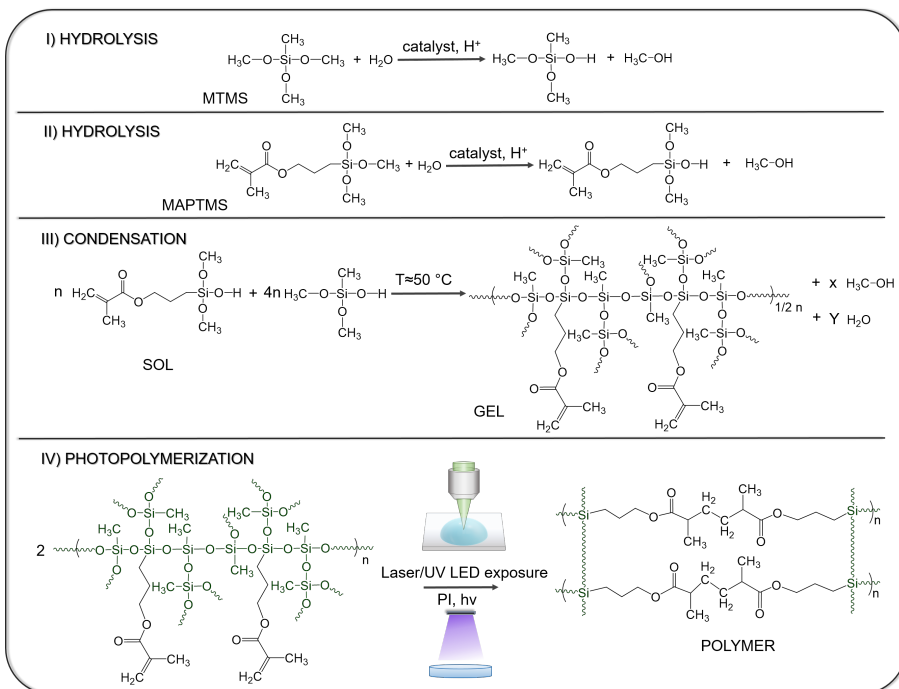


Figure 2.2: Flowchart of material synthesis and photopolymerization via following steps: hydrolysis of MTMS (I) and MAPTMS (II), mixing and condensation (case of 8:2 molar ratio) (III), photopolymerization (IV).

2.2 Characterization

2.2.1 Refractive indices measurements

Refractive indices were collected using Abbemat MW multiwavelength refractometer with YAG (Yttrium-Aluminium-Garnet) prism, white light LED source, and 6 different wavelength filter: 436.5, 486, 513.5, 546.3, 589.3, 643.3 nm. Measurements were performed at 25 °C.

2.2.2 FTIR measurements

Fourier transform infrared spectroscopy (FTIR) data were recorded in transmission mode using FTIR spectrometer ALPHA (Bruker, Inc.), equipped with a room temperature detector DLATGS. Spectra were acquired from 100 interferogram scans with 2 cm⁻¹ resolution, from 4000 to 485 cm⁻¹ wavenumbers.

2.2.3 TGA analysis

For thermogravimetric (TGA) analysis, Pyris 1 TGA (Perkin Elmer) equipment was used; samples were heated under air or nitrogen atmosphere from 30 °C to 900 °C with a heating rate of 5 °C/min.

2.2.4 X-ray diffraction analysis

The X-ray diffractograms were measured using two diffractometers. First, X-ray diffraction data were collected using a Rigaku Miniflex II diffractometer with Bragg-Brentano configuration ($\theta/2\theta$) and equipped with the copper anode (Cu $K\alpha$ radiation). The equipment settings were set as follows: step width was 0.02°, measurement speed 5 °/min. The data were collected in the 2θ range from 10° to 80°.

X-ray diffraction data of 3D microstructures and corresponding powder were collected on a BRUKER AXS (D8 Quest System) X-ray diffractometer equipped with PHOTON 100 CMOS detector. The X-ray generator was operated at 50 kV and 20 mA using Mo $K\alpha$ ($\lambda = 0.71073 \text{ \AA}$) radiation. Obtained X-ray diffraction rings were collected and integrated using Bruker Apex 3 software. Obtained data were compared to the reference data from COD (Crystallography Open Database).

2.2.5 SEM and EDS analysis

SEM images together with EDS were taken with a scanning electron microscope- Hitachi TM3000 at an accelerating voltage of 15 kV. High resolution SEM images were taken with a field-emission SEM Hitachi SU-70 at an acceleration voltage of 5 kV.

2.2.6 Mechanical properties measurements

The mechanical properties were evaluated by a Hysitron TI Premier nanoindenter equipped with a Berkovich diamond probe with a radius of approximately 87 nm. Nine indents, arrayed in a square, were made using a load-controlled indentation method with peak loads from 100 mN to 5 N.

2.2.7 Densities measurements

The non-destructive Archimedes method was used to evaluate the densities. A Radwag 310 analytical balance with a resolution of 0.1 mg was used to measure the mass of the sample in the air (A) and then submerged in the deionized water (B). The deionized water had a density of 0.9978 g/cm³ (ρ_0). Densities were calculated employing the equation:

$$\rho = \frac{A}{(A - B)} * \rho_0 \quad (2.1)$$

2.2.8 UV-VIS transmittance measurements

UV-VIS transmittance spectra were carried out using Cary 5000, Agilent, Santa Clara, CA, USA spectrometer. Transmittance was measured from 200 to 800 nm with a 1 nm interval.

2.3 Fabrication setups and parameters

Two fabrication setups were used in this work. A simplified diagram of a 3D laser lithography fabrication setup is presented in Figure 1.3. The first workstation is located at Vilnius University Laser Research Center. It was used for PI-free polymerization of woodpiles and scaffolds. The fs-laser is Pharos (Light Conversion Ltd.) operating at 1030 nm fundamental wavelength or second harmonic at 515 nm with 300 fs pulse duration and 200 kHz repetition rate. Power is controlled with two power control units consisting of $\lambda/2$ waveplate and Brewster angle polarizer. This two-stage power attenuation technique minimized fluctuations in laser output power and facilitated precise power control during the fabrication process. The laser beam is expanded by a 2 \times -magnification telescope in order to fill all the objective aperture. Structures fabrication was performed with a combination of Aerotech linear stages (ALS130-110-X,Y for positioning in XY plane, ALS130-60-Z for Z-axis) and galvo-scanner, operating in a synchronized regime. The sample is illuminated by a red LED which enables monitoring of the fabrication process in real-time using a CMOS camera.

Resolution arrays, fullerene-type models and gyroids were produced using a Laser Nanofactory setup (Femtika Ltd.) with accuracy at 300 nm [195]. The main light source in this setup is a femtosecond laser Carbide (Light Conversion), outputting either fundamental (1030 nm) or second harmonic (515 nm) radiation at repetition rates in the range of 60–1000 kHz and pulse duration between 250 fs and 10 ps [196]. Average power is controlled with an acousto optical element integrated into the laser. Laser light is guided to an automatic beam expander with a magnification range from 2x to 10x. Structure fabrication is performed by operating synchronously of Aerotech linear stages (ANT130XY-160 (Aerotech Inc.) for XY and ANT130LZS-060 (Aerotech Inc.) for Z-axis) and scanner system (AGV-10HPO (Aerotech Inc.)) [197].

Second harmonic (515 nm) wavelength focused with 20x 0.8 NA (Zeiss) or 100x 1.4 NA (Olympus) objectives was used for 3D free-form polymerization.

After photopolymerization, the development of all fabricated structures was carried out in methyl-isobutyl-ketone for one hour.

2.4 Heat treatment

Nabertherm high-temperature muffle furnace was used for heat treatments up to 1400 °C temperature under air atmosphere for 1 hour, temperature ramp rate was 5 °C/min.

Heat treatments under nitrogen atmosphere up to 1500 °C temperature and under vacuum up to 1400 °C for 1 hour were performed in a Nabertherm high-temperature tube furnace, temperature ramp rate was 5 °C/min.

3. RESULTS AND DISCUSSION



3.1 Introduction to high-resolution 3D inorganics fabrication

Precursors with required properties for fabrication are an essential prerequisite for micro- and nano-dimension ceramic frameworks made by laser 3D lithography. Thus, the search of new precursors suitable for laser 3D polymerization remains an urgent and timely task.

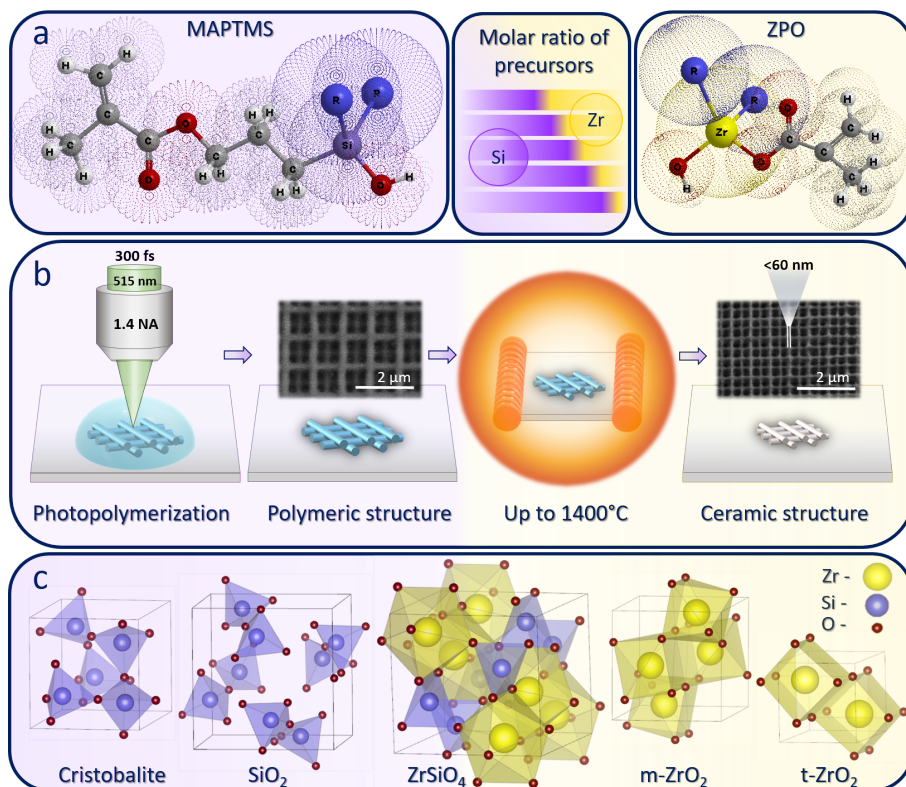


Figure 3.1: Graphical scheme showing precursors, their molar ratios in syntheses (a), photopolymerization and calcination technology (b) and formed crystalline phase lattices after calcination (Cristobalite, SiO₂, ZrSiO₄, monoclinic ZrO₂ and tetragonal ZrO₂) (c). These phases can be observed depending on the treatment temperature and initial hybrid materials compositions.

The presented study is directed to the rapidly developing field of inorganic material 3D object production at nano-/micro scale. The fabrication method includes laser lithography of hybrid organic-inorganic materials with subsequent heat treatment leading to a variety of crystalline phases in 3D objects. A series of organometallic polymer precursors with different silicon (Si) and zirconium (Zr) molar ratios, ranging from 9:1 to 5:5, was prepared via

sol-gel method (Figure 3.1 (a)). All mixtures were examined for perspective used in 3D laser manufacturing by fabricating nano- and micro-feature sized structures. Their spatial downscaling and surface morphology were evaluated depending on chemical composition and crystallographic phase. The appearance of a crystalline phase was proven using single-crystal X-ray diffraction analysis, which revealed a lower crystallization temperature for microstructures compared to bulk materials. Fabricated 3D objects retained a complex geometry without any distortion after heat treatment up to 1400 °C. Under the proper conditions, a wide variety of crystalline phases as well as zircon (ZrSiO_4 - a highly stable material) can be observed (Figure 3.1 (c)). In addition, the highest new record of achieved resolution below 60 nm has been reached (Figure 3.1 (b)). The proposed preparation protocol can be used to manufacture micro/nano-devices with high precision and resistance to high temperatures and aggressive environments.

The results published in paper [A2] are presented in this section (see list of publications): „Laser additive manufacturing of Si/ZrO₂ tunable crystalline phase 3D nanostructures“. *Opto-Electronic Advances*. Vol. 5, No. 5, 210077, 2022, doi.: 10.29026/oea.2022.210077.

For inorganic material printing with predictable phase composition the metalorganic silicon and zirconium mixtures with variable composition was selected. In order to find out the suitability of such precursors for 3D micro/nano scale printing the different variations of the precursor SiX:ZrY were synthesized, characterized and 3D laser exposure and heat treatment experiments were performed. The material in focus is a modified silicate (ORMOSIL) class sol-gel resist originating from SZ2080™ [194].

3.1.1 Refractive indices of SiX:ZrY materials

Initial characterization of selected mixtures include evaluation of refractive index for selected mixtures. Refractive indices of prepared sols and gels are depicted in Figure 3.2. It can be concluded that zirconium content increase raises the refractive index in both sols and gels. However, the change in refractive indices for different composition gels is small enough that there is no need for additional equipment adjustment during the fabrication process. Based on refractive index tendencies for sol and gels, it can be assumed that obtained polymers will follow a similar trend, i. e. slight increase in index values. Polymeric materials that have a greater refractive index than 1.50 are attributed to high-refractive-index polymers (HRIP), which on their own find applications in various fields [198, 199]. For the most part, the refractive indices of all prepared materials in this study are greater than 1.50 (except Si9:Zr1).

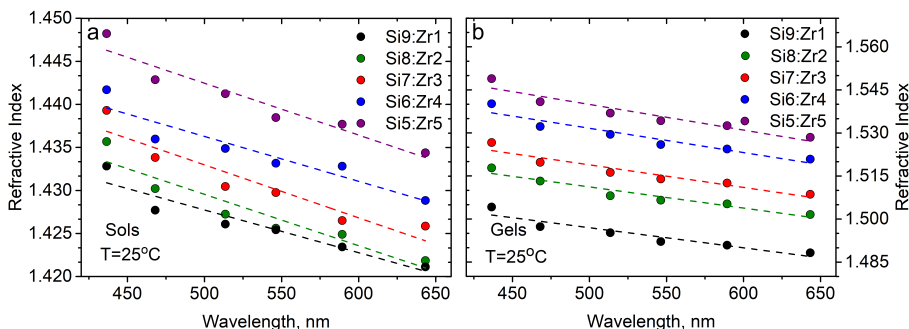


Figure 3.2: Refractive indices (n) of $\text{Si}_X\text{:Zr}_Y$ materials at room temperature (sols (a) and gels (b)) as a function of wavelength. Each measurement was repeated three times, estimated standard deviations were negligible.

3.1.2 Fourier transform infrared spectroscopy analysis

The FTIR analysis was chosen for the evaluation of chemical changes in prepared sols, gels, and polymers. Characteristic FTIR absorption peaks provide qualitative and semi-quantitative information on hydrolysis, condensation, and polymerization. The broad band absorption at $\approx 3330\text{ cm}^{-1}$ is characteristic of the axial deformation of Si-OH, Zr-OH or C-OH groups, which corresponds solvents, such as methanol and isopropyl alcohol or hydrolyzed silane and zirconium (IV) propoxide in sols (Figure 3.3 (a)). It is clear that during condensation (the process described in the paragraph "Materials and Synthesis") solvents, such as methanol and isopropyl alcohol are removed, therefore, a band of -OH groups ($\approx 3330\text{ cm}^{-1}$) decreases in gels and polymers spectra. Similar conclusions can be made for gels (Figure 3.3 (b)), FTIR spectra show the condensation reaction progress during which various Si-O-Si, Zr-O-Zr and Si-O-Zr bonds are formed. Increasing Si precursor concentration results in more intense Si-O-Si bond absorption peaks in polymerized mixtures. The analogous trend is visible for Zr precursor concentration increase. However, absorption peaks of Si-O-Zr overlap and derive clear bond concentration trends for different mixture variations is cumbersome. After condensation (Figure 3.3 (b)) Si-O-Si ($1130\text{-}1000\text{ cm}^{-1}$), Si-O-Zr ($1000\text{-}900\text{ cm}^{-1}$), Zr-O-Zr ($\approx 430\text{ cm}^{-1}$) absorption become broader and more complex, showing more overlapping bands, which confirms that siloxanes, silanates or zircoxanes chains become longer or branched. Additionally, FTIR data (Figure 3.3 (c)) indicate polymerization reaction process during which the signal of alkene groups diminishes, leading to polymerized material after thermal treatment for 3 hours at $140\text{ }^\circ\text{C}$.

Based on FTIR and refractive-index data the selected synthesis procedure is considered valid for further examination.

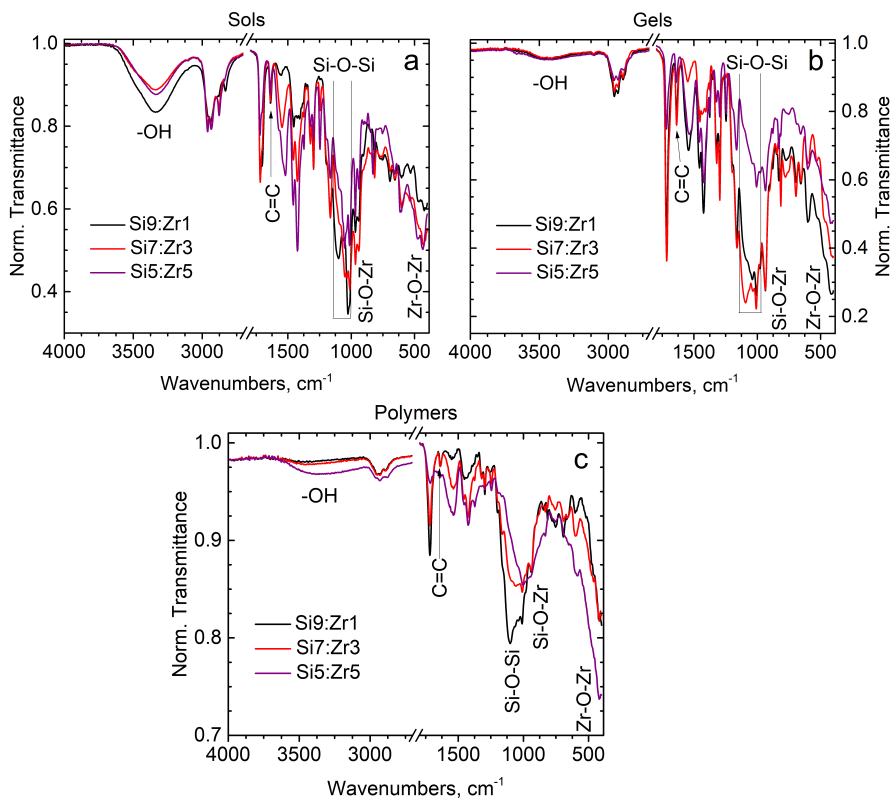


Figure 3.3: Fourier transform infrared spectroscopy (FTIR) spectra of $\text{Si}_x\text{:Zr}_y$ sols (a), gels (b) and polymers (c).

3.1.3 Thermogravimetric and volumetric shrinkage analysis of $\text{Si}_x\text{:Zr}_y$ materials

Thermogravimetric analysis and volumetric shrinkage data of 3D cubes for different ratio $\text{Si}_x\text{:Zr}_y$ materials and structures are depicted in (Figure 3.4 and Figure 3.5). Micro cubes were annealed on corundum substrates for 1 h at 1000°C , under air atmosphere. In Figure 3.4 red lines show weight loss dependence on temperature. The initial sharp weight loss (up to $\approx 140^\circ\text{C}$) is attributed to evaporation of solvents, such as methanol and isopropyl alcohol. Based on FTIR data it can be concluded that materials reach almost complete thermal polymerization at 140°C temperature (double $\text{C}=\text{C}$ bond (1650 cm^{-1}) signal intensity, while for polymers this signal almost disappear [200]. Thermal polymerization temperature determination for prepared mixtures was necessary in order to properly compare weight loss for laser printed structures during heating. Initial weight is set to 100% at 150°C , based on assumption

that polymerization is complete and bulk polymerized mixtures are similar to laser printed material. The weight loss patterns indicate that decomposition of organic moiety is finished at 600 - 700 °C temperature range. The weight stabilization at higher temperature points out the inorganic material formation. TGA data reveals that with increasing silicon content, weight loss increases and it ranges from 51% to 62% (Figure 3.5 (c)). It is necessary to mention, that with a higher amount of zirconium, the inorganic material is achieved at lower temperature. The weight loss and volume shrinkage comparison is depicted in Figure 3.5 (c). The volume change after annealing was estimated by measuring volume of fabricated cubes. The volumetric shrinkage was calculated employing the equation:

$$\Delta V_{(shrinkage)}(\%) = \frac{V_{(initial)} - V_{(final)}}{V_{(initial)}} * 100\% \quad (3.1)$$

here, $V_{(initial)}$ is a volume of cube before heat treatment, $V_{(final)}$ - after heat treatment. Each material sample contained set of three cube out of which standard deviation (%) was calculated. The error ranges from 0,56 to 3,70 percent, with lowest values for Si:Zr 8:2 composition and highest for Si:Zr 5:5 composition. The low deviation from mean value brings to conclusion that 3D structure fabrication and post heat treatment are reproducible and reliable. All experimental data are provided in an appendix table A.1.

Data in Figure 3.5 (c) bring to conclusion, that denser ceramic structures are obtained by increasing the silicon content, while theoretical prognosis is opposite. The calculated volume shrinkage should increase with higher zirconium content, because crystalline zirconia is much denser than silica. In order to compare obtained experimental results to the theoretical predictions, the theoretical shrinkage was calculated. The mass and density of each material was calculated using molecular weights of fully condensed precursors and methacrylic acid (molecular weights: condensed ZPO- 91.22 g/mol, condensed MAPTMS- 155.25 g/mol, MAA- 86.09 g/mol and oxygen- 15.999 g/mol), (densities: ZPO- 1.058 g/cm³, MAPTMS- 1.045 g/cm³, MAA- 1.020 g/cm³). The expected mass and density of ceramics was calculated based on assumption that silicon and zirconium are completely transformed to cristobalite and tetragonal ZrO₂ (molecular weights: cristobalite- 60.08 g/mol, t-ZrO₂- 123.22 g/mol), (densities: cristobalite (COD 96-900-8226)- 2.309 g/cm₂, t-ZrO₂ (COD 96-152-5706)- 6.190 g/cm₂). The fabricated cubes contained an unknown amount of amorphous phase after annealing at 1000 °C. It can be assumed that a higher amount of amorphous zirconia should be present compared to silica which crystallizes at lower temperature [201, 202]. Therefore, the trend in experimental data is opposite to the predicted (Figure 3.5 (c)).

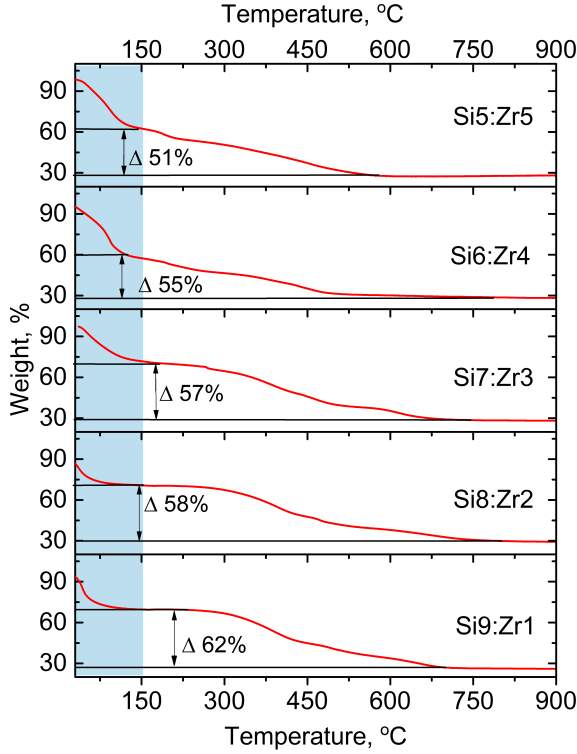


Figure 3.4: TGA data of SiX:ZrY showing weight loss *vs* temperature (red line). TGA measurements were performed once for each material, so it is not possible to include error bars for weight loss.

3.1.4 Investigation of fabrication prospects

To clarify the fabrication prospects of proposed mixtures, woodpiles were fabricated and annealed on corundum substrates for 1 h at 1000 °C, under air atmosphere (Figure 3.6). During woodpiles fabrication average laser power was 48, 56, and 64 μW , focused with a 100x1.4 NA objective, 300 fs pulse duration, 200 kHz repetition rate, 515 nm wavelength, scanning speed was 200 and 500 $\mu\text{m/s}$, hatching distances in both, X and Y axes, was 0.1 μm . The higher power was not used due to the uncontrolled burning of Si9:Zr1 material. The irradiance was calculated employing the following equation [203]:

$$I = \frac{E_p}{\tau_p \pi \omega^2}, \quad (3.2)$$

here I is irradiance [TW/cm^2], $E_p = P/f$, where P [mW] is average laser power, f - repetition rates [kHz], τ_p is the pulse duration [fs], $\omega = 0.61\lambda/\text{NA}$ [nm]. It was found that the highest resolution of the inorganic structure (58.7 ± 1.5 nm)

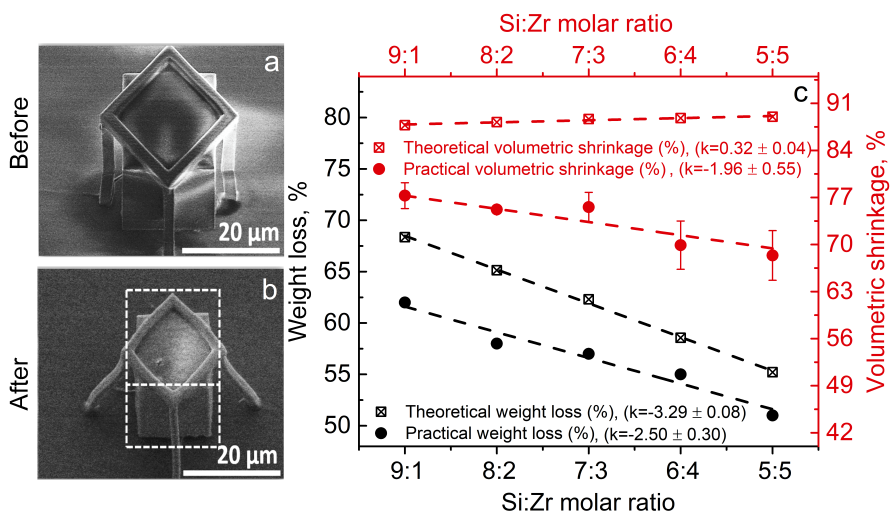


Figure 3.5: SEM images of the Si₇:Zr₃ cube before (a) and after (b) heat treatment at 1000 °C. The dashed line in (b) represents the dimensions of the cube before heat treatment. Theoretical (square symbols) and practical (circle symbols) weight loss for the phase transition from the polymeric to the glass/ceramic phase (black) and volumetric shrinkage (red) of cubes at the same phase transition (error bars of volumetric shrinkage represent standard deviation, n = 3).

is achieved for Si₉:Zr₁ material using 64 μW laser power, 200 μm/s velocity (irradiation 0.22 TW/cm²) followed by annealing at 1000 °C (Figure 3.6(f)). To the best of our knowledge, this is the highest resolution for inorganic 3D ceramic derivative achieved by printing up to 2022. The same woodpiles were fabricated with all hybrids for resolution comparison of all materials. The dependence of woodpile lines width on the laser irradiance is shown in Figure 3.7 (a, b) and the numerical values are listed in Appendix Tables A.2, A.3, A.4, A.5. At lower laser irradiance it is difficult to get a clear relationship between resolution and material composition, nevertheless, at higher laser irradiance it is evident that the resolution is higher where the zirconium content is lower. In prepared mixtures, the zirconium amount is linked to the methacrylic acid, while the silicon amount corresponds to the methyl methacrylate functional group. The resolution dependence of 3D derivatives changing composition can be explained by the fact that the photopolymerization activation energy of methacrylic acid is several times lower than the activation energy of the methyl methacrylate under the same conditions ($E_a(\text{methacrylic acid}) = 1.79$ kCal/mol, $E_a(\text{methyl methacrylate}) = 4.48$ kCal/mol) [204]. The same laser energy density tends to polymerize a larger volume of material with a lower photopolymerization activation energy during the unit pulse. However, photo-

polymerization activation energy may also depend on the influence of adjacent functional groups, photoinitiators, quenchers, and/or ambient conditions [205]. The printed structure treatment in a developing solvent after photopolymerization can also affect the resolution due to the solvent ability to dissolve the unpolymerized monomer molecules at the phase junction between polymer and gel. The higher solvent affinity to substance and the lower molecular weight or less branched structure of the molecule (steric effect), the better solubility is achieved [206]. Also, the increase in molecular weight in most cases leads to a decrease in solubility because the increase in molecular weight increases the cohesive energy density (CED), where, according to J. Hildebrand, the solubility parameter is the square root of the CED [207]. The molecular weight and branching are smaller for zirconium and methacrylic acid monomer compared to silicon monomer. Accordingly, as the zirconium content increases, the resolution of the 3D structure should increase too, different from the reaction activation energy influence. The competition takes place between two opposing processes. This fact explains why it is difficult to see the evident dependence of the resolution on the composition of the material at low laser irradiance. Similarly, the easier penetration of the solvent into the material can affect the swelling of the polymeric structure. It is important to mention that the solubility of materials depends on many factors, thus it is used here only for a comparison.

3.1.5 Quality and composition of structures

Scaffolds were produced with 10 mm/s fabrication velocity and average laser power of $655 \mu\text{W}$, focused with a 20×0.8 NA objective. Structures were annealed at 1000°C , 1200°C and 1400°C temperatures in order to determine the surface quality, elements distributions, resistance to aggressive chemicals, and crystalline phases of structures.

The graph in Figure 3.8 shows the dependence of the mass of silicon and zirconium elements on the initial sols composition. The images below are EDS maps of the spatial distributions of elements. Energy dispersive X-ray analysis confirmed that during photopolymerization and heating processes the relative amount of silicon and zirconium does not change and elements are evenly distributed over the entire surface of inorganic structures.

The surface quality of ceramic scaffolds annealed at 1400°C surface and the absence of porosity are confirmed by SEM images depicted in Figure 3.9. The porosity and deformations of the structure are observed only in the scaffold made of Si₉:Zr₁ (Figure 3.9 (f, k)). Unfortunately, corner fractures of the structures occurred by placing them on the carbon film prior to SEM analysis.

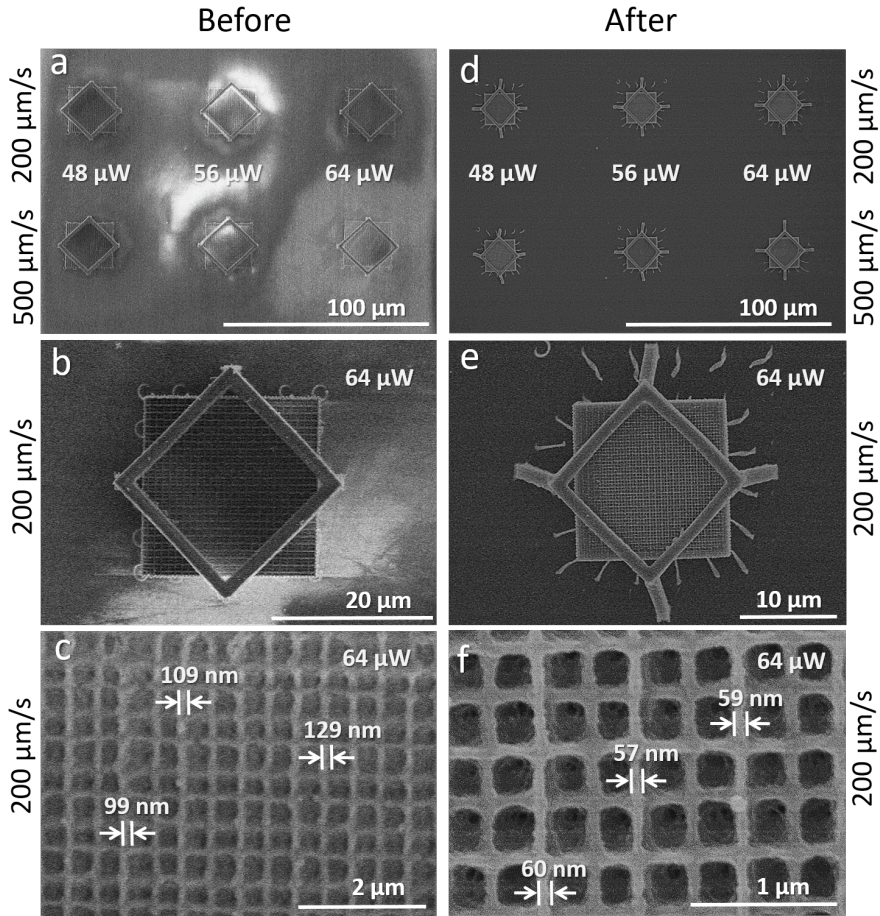


Figure 3.6: Si₉:Zr₁ woodpiles before heat treatment (a, b, c) and after heating at 1000 °C under air atmosphere (d, e, f). Woodpiles fabricated at 200 μm/s speed (on the top line) and at 500 μm/s speed (on the bottom line) with 48, 56, 64 μW incident irradiation power (a, d). The highest resolution of woodpiles was obtained by applying 200 μm/s and 64 μW parameters (b, c, e, and f).

3.1.6 Study of crystallization processes

For comparison of crystalline phases of 3D microstructures and powder, samples were placed on a single crystal diffractometer measuring needle (Fig. 3.10 (d)), obtained X-ray diffraction data (Debye-Scherrer rings (Fig. 3.10 (c)) were integrated. Obtained X-ray diffractograms were recalculated to Cu K α ($\lambda = 1.541874$ Å) wavelength using Bragg's law and data were compared to the reference data from COD (Crystallography Open Database) (Fig. 3.10 (a, b)).

In Figs. 3.11, 3.12, 3.13 XRD data of scaffolds (a-e) and corresponding

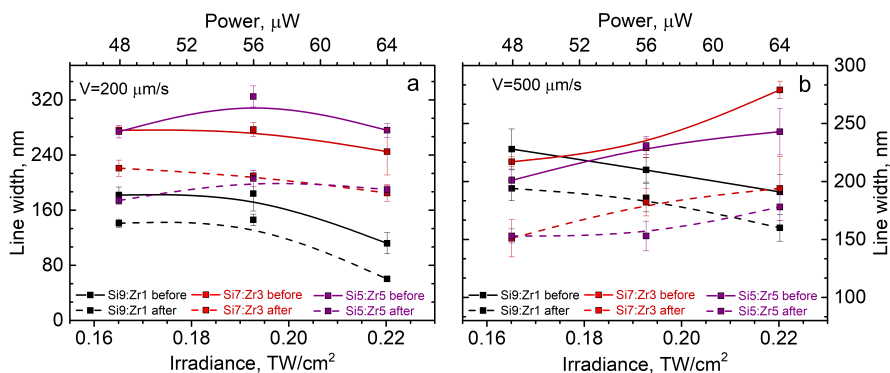


Figure 3.7: The dependence of Si9:Zr1, Si7:Zr3, Si5:Zr5 woodpiles lines width on the laser irradiance at 200 $\mu\text{m/s}$ speed (a). Before heat treatment- solid lines, after- dashed lines. The dependence of Si9:Zr1, Si7:Zr3, Si5:Zr5 woodpiles lines width on the laser irradiance at 500 $\mu\text{m/s}$ speed (b) (error bars represent Std. dev., $n = 3$).

powders (g-l) are presented for samples heat treated at 1000 $^{\circ}\text{C}$, 1200 $^{\circ}\text{C}$ and 1400 $^{\circ}\text{C}$, under air atmosphere. Scaffolds were annealed on graphite substrates, while powder samples were prepared by heating materials gels at appropriate temperatures (1000-1400 $^{\circ}\text{C}$) in corundum crucibles. The color of all structures and powders was white, indicating that no organic contaminants remained after calcination. Obtained data were compared to the reference patterns of the Crystallography Open Database (COD).

At the lowest heating temperature (Figure 3.11) in both, scaffolds and powders, the formation of crystalline cristobalite and tetragonal ZrO_2 phases are observed. Increasing zirconium amount leads to a more pronounced tetragonal ZrO_2 crystalline phase. However, a relatively high background in diffractograms indicates the presence of an amorphous phase. No visible deformations in 3D structures were observed for all series of samples with different compositions after calcination at 1000 $^{\circ}\text{C}$. With increasing heating temperature to 1200 $^{\circ}\text{C}$ (Figure 3.12) leads to samples, both powder, and structures, with higher crystallinity. However, X-ray diffraction data for all samples still provide evidence of glassy amorphous phase presence. Diffractogram of Si5:Zr5 3D structure shows that the cristobalite phase remains as pronounced as tetragonal ZrO_2 , while different behavior is observed for powder sample, tetragonal ZrO_2 phase is dominating. In order to find out why the XRD patterns of powders and 3D structures look so different, an extensive study should be done. However, it can be assumed that the difference in the amount of material (in the case of structure is very small) or the presence and absence of polymerization before heat treatment results in a difference in the XRD

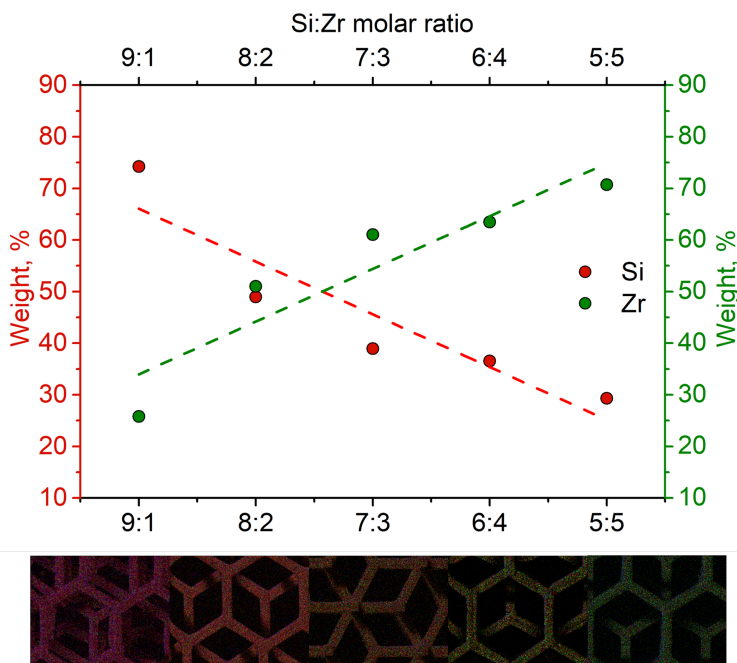


Figure 3.8: Energy-dispersive X-ray spectroscopy (EDS) analysis of scaffolds annealed at 1000 °C. The graph above shows the elements weight (w%) dependence on the initial composition of materials. Images below- EDS mapping of scaffold, where Si-red, Zr-green.

patterns due to diffusion or heat distribution discrepancies. Each 3D structure preserves its shape after 1200 °C heat treatment, except Si9:Zr1. The materials with the higher initial amount of silicon, start to melt due to the lower melting temperature of silicon oxide compared to zirconium oxides. The most stable zirconium dioxide phase is monoclinic, while tetragonal and cubic phases tend to form at higher temperatures [208]. However, the monoclinic ZrO_2 phase formed only at 1400 °C (see Figure 3.13(a-g)), while tetragonal dominated at all heat treatment temperatures and starting compositions (except Figure 3.13(g)). Such phenomenon can be explained using Ostwald's Step Rule, stating that phase formation follow a general pattern when phases with the highest energy are formed first following the transition to lower energy phases [209, 210]. This means that the higher energy metastable tetragonal phase is frozen in prepared samples. Recently, A. Auxéméry et al. demonstrated that it is possible to stabilize metastable tetragonal ZrO_2 not only by cationic substitution but it can be achieved by varying the synthesis conditions [211]. In sum, differences between the amounts of elements, such as Si, Zr, and O, before and after heat treatment, resulting in distinct ratios of the formed crystalline phases and the

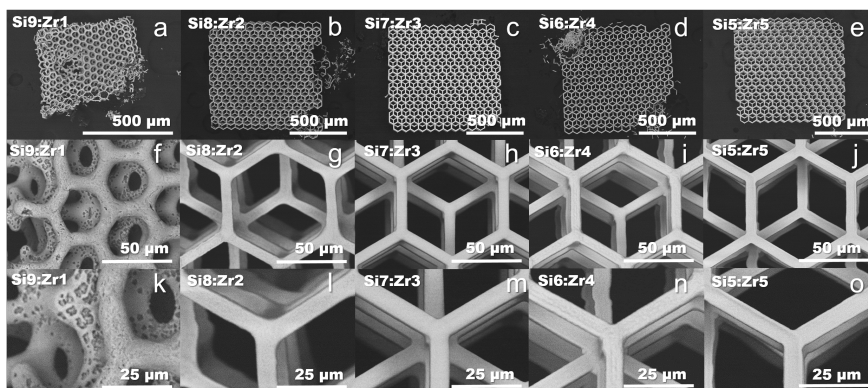


Figure 3.9: Scanning electron microscope images of Si9:Zr1 (a, f, k), Si8:Zr2 (b, g, l), Si7:Zr3 (c, h, m), Si6:Zr4 (d, i, n), Si5:Zr5 (e, j, o) scaffolds annealed at 1400 °C. The scale bars are 500 (a, b, c, d, e), 50 (f, g, h, i, j) and 25 μm (k, l, m, n, o).

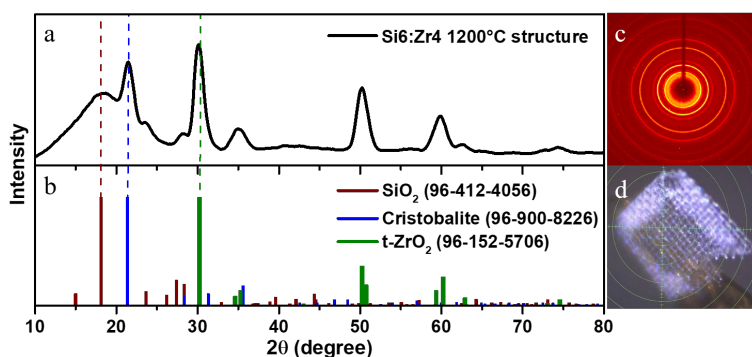


Figure 3.10: X-ray diffraction measurements. a- X-Ray diffraction pattern of Si6:Zr4 structure annealed at 1200 °C temperature, b- reference patterns, c- Debye-Scherrer rings obtained after X-Ray diffraction measurement, d- photograph of Si6:Zr4 structure annealed at 1200 °C temperature placed on the needle.

creation of further, higher or lower energy phases, although heated at the same temperature.

3.1.7 Study on the resistance to aggressive impact

Moreover, for the stability study of ceramic structures to aggressive chemical impact, ceramic (annealed at 1000 °C) in a comparison with polymeric Si7:Zr3 scaffolds were processed in a solution of piranha (volume ratio of 4:1 sulfuric

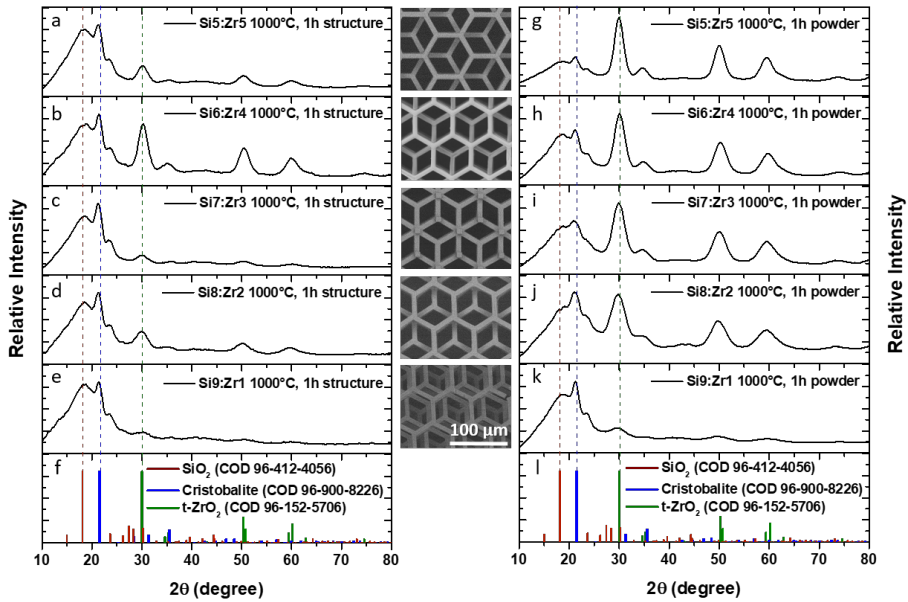


Figure 3.11: X-ray diffractograms of structures (SEM images) annealed at 1000 °C ((a)-Si5:Zr5, (b)-Si6:Zr4, (c)-Si7:Zr3, (d)-Si8:Zr2, (e)-Si9:Zr1, (f)-reference data) and X-ray diffractograms of powders annealed at 1000 °C ((g)-Si5:Zr5, (h)-Si6:Zr4, (i)-Si7:Zr3, (j)-Si8:Zr2, (k)-Si9:Zr1, (l)-reference data). SEM images show corresponding 3D scaffolds treated at 1000 °C temperature. SEM images correspond to the same scale bar.

acid (Chempur, 95-98%) and peroxide (Chempur, 50%)), a highly corrosive and an extremely powerful oxidizer, in an ultrasonic bath for 15 and 60 minutes. The polymeric scaffold cracked and acquired defects after piranha and ultrasonic treatment (Figure 3.14 (b, c)), while the ceramic structure showed complete immunity to aggressive conditions (Figure 3.14(e, f)).

The resistance of the ceramic structures to alkali was also investigated. Ceramic and polymeric Si7:Zr3 scaffolds were processed in a 1 mol/l aqueous potassium hydroxide (Penta, 85%) solution in an ultrasonic bath for 15 minutes. Alkali did not adversely affect either polymer or ceramic structures (see Figure 3.16).

In order to determine the resistance of ceramic structures to negative temperatures, the study described below was performed. A corundum substrate with Si9:Zr1 3D ceramic nanostructures on the surface was instantly immersed in a thermos filled with liquid nitrogen (≈ 77 K) and stored until the nitrogen had completely evaporated under ambient conditions. The evaporation process lasted 10 minutes. The results of this study confirmed that such structures remain robust and the adhesion between the specimen and the substrate remains even

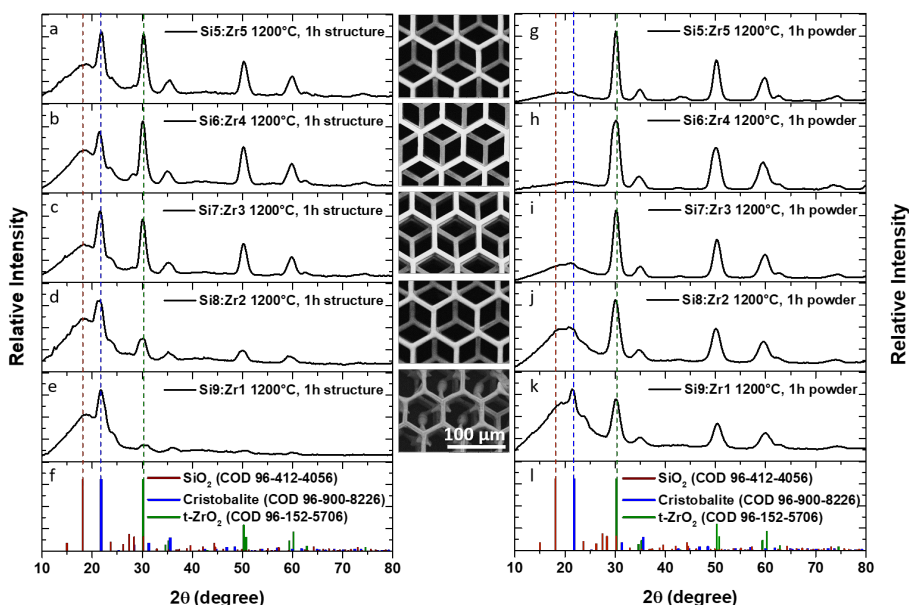


Figure 3.12: X-ray diffractograms of structures (SEM images) annealed at 1200 °C ((a)-Si5:Zr5, (b)-Si6:Zr4, (c)-Si7:Zr3, (d)-Si8:Zr2, (e)-Si9:Zr1, (f)-reference data) and X-ray diffractograms of powders annealed at 1200 °C ((g)-Si5:Zr5, (h)-Si6:Zr4, (i)-Si7:Zr3, (j)-Si8:Zr2, (k)-Si9:Zr1, (l)-reference data). SEM images show corresponding 3D scaffolds treated at 1200 °C temperature. SEM images correspond to the same scale bar.

after the rapid negative temperature impact. According to SEM measurements of Si9:Zr1 (see Figure 3.15) ceramic woodpile fabricated at 500 $\mu\text{m/s}$ and 64 μW , the negative temperature caused no damage to the 3D nanostructures or their detachment from the substrate (which, intuitively, could be caused due to different thermal expansion coefficients).

A summarized graphically visualized map of 3D nanostructure resiliency is shown in Figure 3.16, which confirms that fabricated ceramic micro-nano 3D structures withstand a wide range of temperatures (at least from -200 °C to 1400 °C), remain stable and maintain sub-100 nm resolution throughout the pH range even under ultrasonic exposure [B1].

3.1.8 Conclusions on high-resolution 3D inorganics fabrication results

The hybrid organic-inorganic polymer resists of variable composition SiX:ZrY can be directly 3D laser structured and heat-treated to produce micro- and nanostructures of different SiO₂/ZrO₂ inorganic phases. In particular, along with a typical amorphous (glass), t-ZrO₂ and monoclinic cristobalite, the

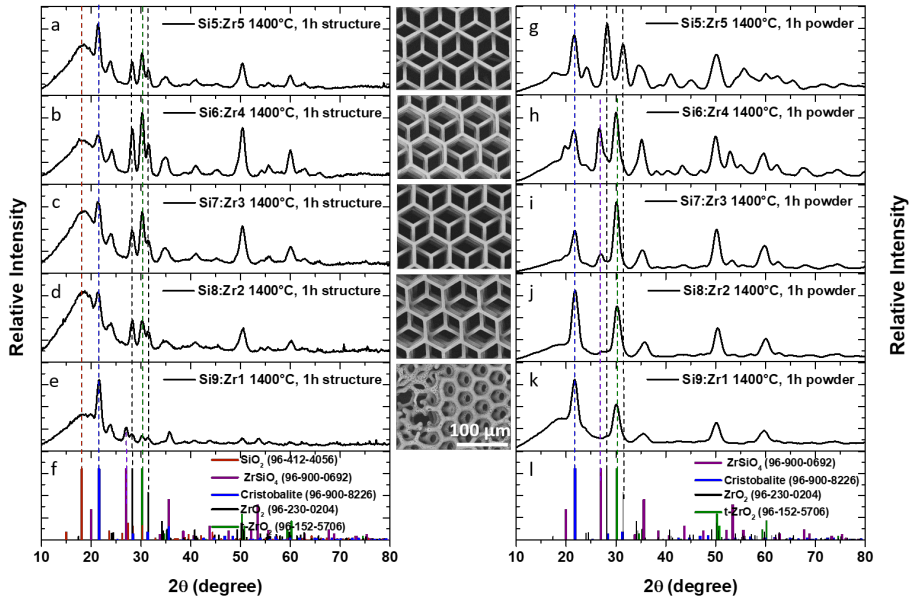


Figure 3.13: X-ray diffractograms of structures (SEM images) annealed at 1400 °C ((a)-Si₅:Zr₅, (b)-Si₆:Zr₄, (c)-Si₇:Zr₃, (d)-Si₈:Zr₂, (e)-Si₉:Zr₁, (f)-reference data) and X-ray diffractograms of powders annealed at 1400 °C ((g)-Si₅:Zr₅, (h)-Si₆:Zr₄, (i)-Si₇:Zr₃, (j)-Si₈:Zr₂, (k)-Si₉:Zr₁, (l)-reference data). SEM images show corresponding 3D scaffolds treated at 1400 °C temperature. SEM images correspond to the same scale bar.

new m-ZrO₂ and zircon phases have been detected.

The t-ZrO₂ and cristobalite phases are observed after calcination at 1000 °C, 1200 °C and 1400 °C for all initial compositions Si₅:Zr₅-Si₉:Zr₁. However, the m-ZrO₂ and zircon polycrystalline phases are mostly pronounced in printed Si₆:Zr₄ and Si₉:Zr₁ composition samples after treatment at 1400 °C. This procedure is essential and relevant at the micro/nano-scale leading to individual feature size below 100 nm, while 3D additive manufacturing methods of hard inorganic materials is far from being readily available.

Repeatable nanoscale features size down to 60 nm were achieved for the composition of Si₉:Zr₁ heat-treated at 1000 °C. The resolution is proven for fine woodpile geometry periodic 3D structures. This is the highest resolution achieved for an ORMOSIL class material using laser additive manufacturing based on multi-photon lithography and thermal post-processing. The 3D nanostructures also proved to be robust in low temperatures down to -200 °C despite rapid cooling with liquid nitrogen and do not detach from the substrate, delaminate into layers, fracture due to instantaneous thermal expansion or show any kind of geometrical distortions.

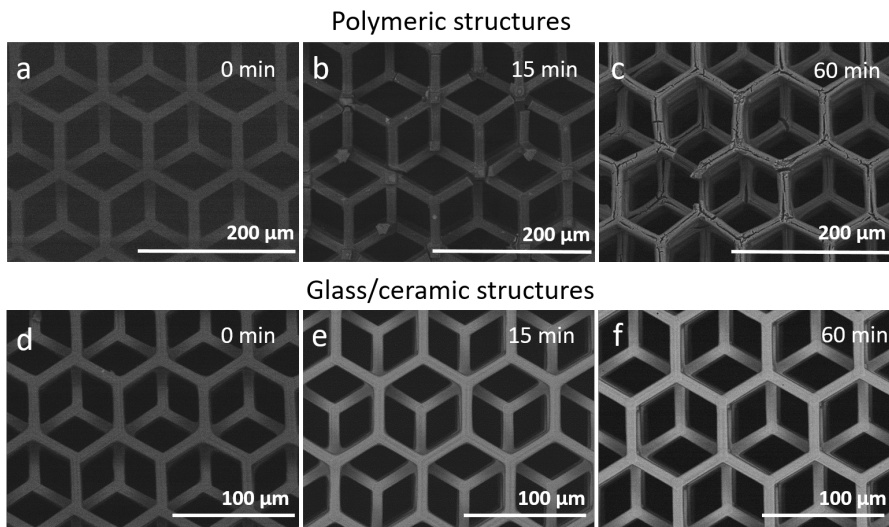


Figure 3.14: Chemical resistance investigation - applying ultrasonic bath while immersion in piranha solution. (a) - Si₇:Zr₃ polymeric structure before chemical treatment, (b) - Si₇:Zr₃ polymeric structure after chemical treatment (duration 15 min), (c) - Si₇:Zr₃ polymeric structure after chemical treatment (duration 60 min), (d) - Si₇:Zr₃ ceramic structure (after 1000 °C heat treatment) before chemical treatment, (e) - Si₇:Zr₃ ceramic structure after chemical treatment (duration 15 min), (f) - Si₇:Zr₃ ceramic structure after chemical treatment (duration 60 min).

In perspective, further variation in composition of the metalorganic pre-polymer SiX:ZrY in finer steps could yield more fine-adjusted physical and chemical properties. This should be expected not only for the examined current composition, but for other multicomponent metalorganic polymer mixtures. Such approach is highly promising, especially with combination with localised heat treatment methods, e.g. focused electron or ion beam, as well as a focused infrared laser radiation could generate a 3D structures with varying and controllable material properties throughout all 3D structure. Besides, proposed preparation approach is promising for 4D printing of inorganic smart/programmable materials.

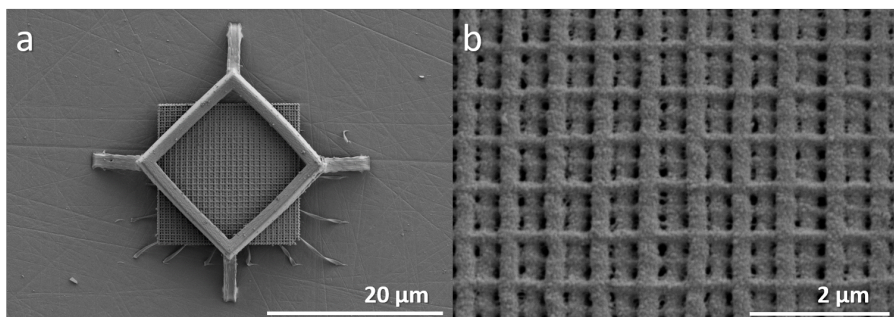


Figure 3.15: Scanning electron microscope images of $\text{Si}_9\text{:Zr}_1$ ceramic woodpile fabricated at $500 \mu\text{m/s}$ and $64 \mu\text{W}$ after storage in liquid nitrogen ($\approx 77 \text{ K}$) for 10 minutes. The scale bars are $20 \mu\text{m}$ (a) and $2 \mu\text{m}$ (b). The surface grainy structure is due to a magnetron sputtered conductive 10-20 nm metallic silver to reduce charge up during SEM observations.

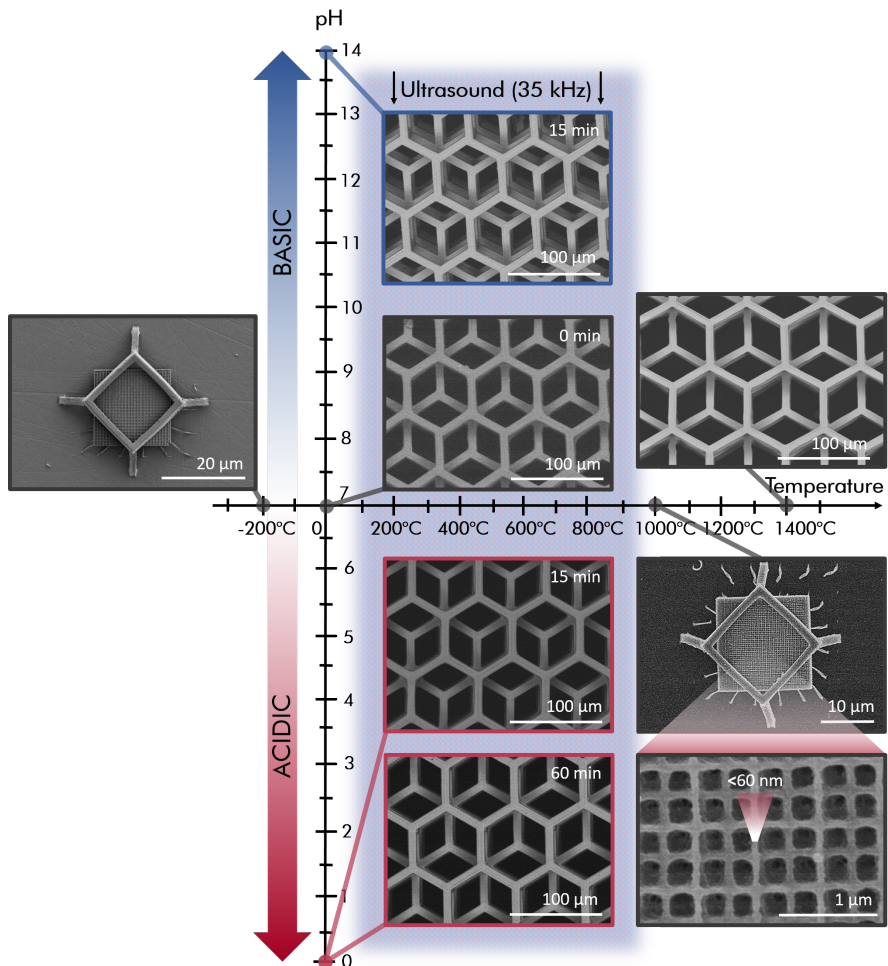


Figure 3.16: Resistance of ceramic/crystalline 3D nano/micro-derivatives to aggressive chemicals, temperature and ultrasound in Si/ZrO₂ system. Figure produced using results from [A2].

3.2 Introduction to manufacturing of 3D hard ceramic structures

In this study, the fabrication of hard ceramic SiOC 3D microstructures by precursor synthesis, laser lithography, and pyrolysis combination is proposed. Precursors are hybrid organosilicon materials prepared *via* sol-gel method using trimethoxymethylsilane and 3-(trimethoxysilyl)propyl methacrylate, which has an acrylate functional group enabling laser photopolymerization process. Hard 3D ceramic structures (hardness up to ≈ 15 GPa, reduced elastic modulus ≈ 105 GPa) from soft organometallic derivatives are obtained after high-temperature pyrolysis under a nitrogen atmosphere. The advantage of the proposed method is the absence of shrinkage defects leading to a uniform repetitive decrease in the volume of printed microstructures. In contrast to slurry-based printing technology, the proposed method is focused on homogeneous monolithic molecular resins resulting in visual smooth surfaces of prepared microstructures. Moreover, the printing resolution of the proposed method is substantially improved through the absence of pre-dispersed ceramic microparticles in mixtures, which is a necessary element in a slurry-based technology.

The presented results chapter are published in a patent application [P1] (see list of publications): G. Merkininkaitė, D. Gailevičius, S. Šakirzanovas (2022). "A method for production of a photo-curable inorganic-organic hybrid resin and a method for production of hard SiO_xC_y ceramic microstructures using the photo-curable inorganic-organic hybrid resin". Patent application no. LT2022537. Patent submission no. 107277. Submitted on September 14 (2022) and in a paper [A3] (see list of publications): G. Merkininkaitė, et al. „Additive Manufacturing of SiOC, SiC, Si_3N_4 Ceramic 3D Micro-Structures“. *Advanced Engineering Materials*, 2023, doi.: 10.1002/adem.202300639.

In order to examine the suitability of silicon-organic precursors for the printing of hard 3D structures variable compositions using two monomers were synthesized (MTMS:MAPTMS (9:1, 8:2, 7:3)), characterized before and after 515 nm laser or ≈ 365 nm LED (light emitting diode) treatment.

3.2.1 Ceramic plate fabrication

First of all, disk-shaped structures (plates) were fabricated in order to investigate the mechanical, crystalline and optical properties of the materials. For this purpose, 1 mm height and 8 mm diameter PDMS preforms were filled with prepared liquid materials (MTMS:MAPTMS 9:1, 8:2, 7:3), the materials were condensed on a hotplate at 50°C for 1.5 h and polymerized by homemade LED lamp (365 nm wavelength) for 1 h. Plates were annealed on corundum substrates for 1 h in the temperature range from 1000°C to 1500°C under nitrogen atmosphere, and at 1400°C under vacuum. A scheme of plate fabrication is shown in Figure 3.17.

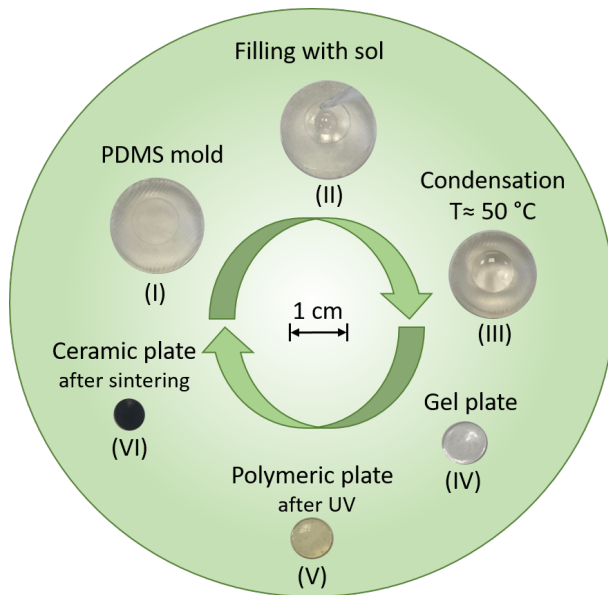


Figure 3.17: A scheme of ceramic plates fabrication.

3.2.2 Evaluation of refractive indices

Initial characterization includes the evaluation of refractive indices (RI) for selected mixtures. RI of prepared sols, gels and polymers determines the transmittance to electromagnetic waves and helps to set the manufacturing coefficient, which is equal to the RI of the material. To compensate the light path through the air and material differences, 3D structure model in the Z direction must be divided by the RI. Figure 3.18 shows a 3D structure model and a structure made of MTMS:MAPTMS 8:2 material without introducing the manufacturing coefficient into the code. The higher the refractive index of the material, the higher structure is obtained. It is evident that it is necessary to evaluate the RI of the material in order to obtain an appropriate shape. The required effective manufacturing coefficient was determined to be 1.7 for MTMS:MAPTMS 8:2 material. The coefficient is higher than the established RI of materials.

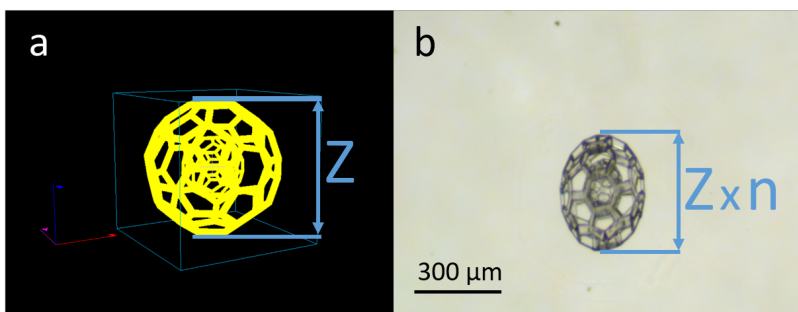


Figure 3.18: 3D fullerene model with a smaller fullerene inside (a) and a structure made of MTMS:MAPTMS 8:2 material without introducing a refractive index into the fabrication code (b). Z is the height of the structure set in the model before fabrication. n is a factor that is equal to the refractive index of the material and affects the height of the manufactured structure.

RI of prepared MTMS:MAPTMS (9:1, 8:2 and 7:3) sols, gels and polymers are depicted in Figure 3.19 (a), (b) and (c), respectively. The RI ranged between 1.371 - 1.390, 1.428 - 1.454 and 1.431 - 1.456 across the entire visible spectrum (436.5 - 643.3 nm) in sols, gels and polymers. All experimental data are provided in Appendix Table A.6. Based on Lorentz-Lorenz theory, the RI of materials can be predicted from their molar refractions and molar volumes of their substituent groups and backbone repeating units [212]. Therefore, the higher MTMS content or higher degree of structural bonding in materials results in a higher RI (see Figure 3.19).

RI results indicate that synthesized materials can be applied in a wide range of advanced optical and optoelectronic devices including light-emitting diodes [213], microlenses [7, 214], image sensors [215], photonic crystals [216] and metamaterials where high RI and transparency to the visible spectrum are required [198].

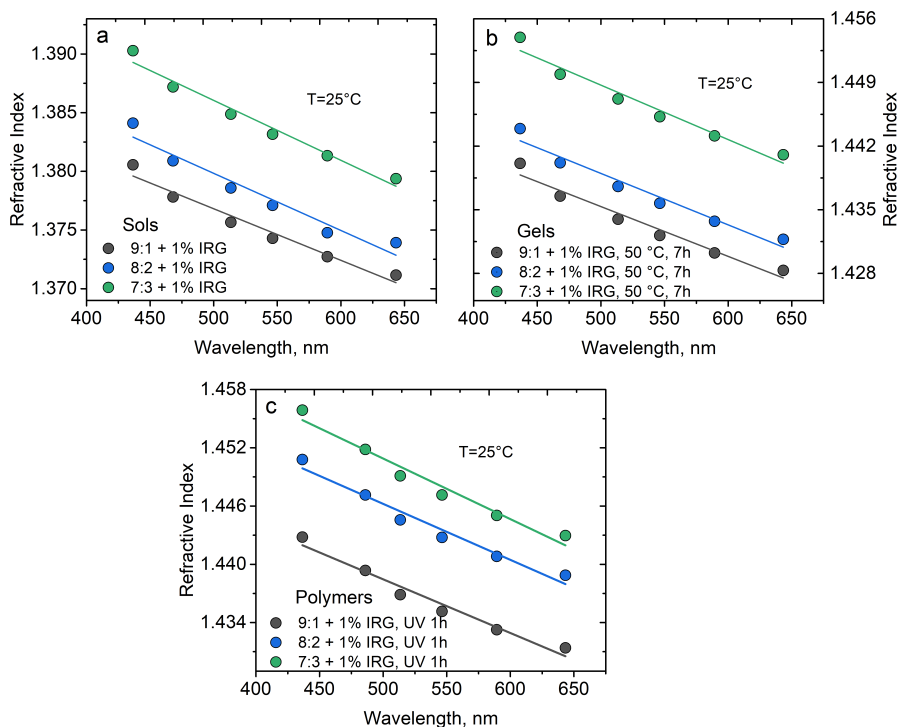


Figure 3.19: Refractive indices of MTMS:MAPTMS + 1% PI (IRG 369) materials at 25 °C temperature (sols (a), gels (b) and polymers (c) as a function of wavelength.).

3.2.3 Investigation of changes in chemical structure

Optimizing, controlling, and designing these sol-gel reactions is crucial for achieving the desired properties and characteristics of the final product. Numerous studies on silica sol-gel systems have demonstrated that the alkoxy silane hydrolysis and condensation process, as well as the properties of the resulting polymer, can be influenced by various synthesis parameters. These parameters include temperature, pH, water/alkoxy silane ratio, and solvent used [100]. The latter synthesis parameters were selected based on studies carried out previously [194, 217]. The changes in bonding of prepared MTMS:MAPTMS (9:1, 8:2, 7:3) materials after hydrolysis (a), condensation (b), polymerization (c) and high-temperature treatment (d) were evaluated using FTIR analysis (see Figure 3.20).

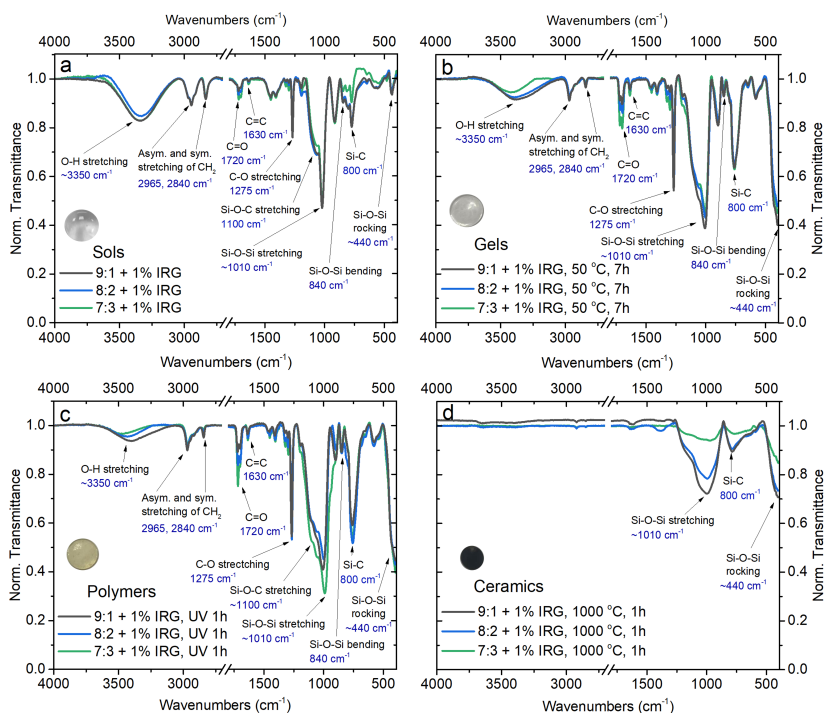


Figure 3.20: Fourier transform infrared spectroscopy (FTIR) spectra of MTMS:MAPTMS + 1% PI sols (a), gels (b), polymers (c) and ceramics heated at 1000 °C temperature in a nitrogen atmosphere (d).

Under acidic conditions the hydrolysis reaction of alkoxy silane in most cases is faster than the condensation reaction, therefore, hydrolysis occurs first at room temperature. FTIR data of MTMS:MAPTMS (9:1, 8:2, 7:3) sols were collected after the last synthesis step, *i.e.*, filtration. The presence of solvents (water, isopropyl alcohol, and methanol) is confirmed by the broadband in FTIR spectra that peaks at $\approx 3350\text{ cm}^{-1}$ (a) and is attributed to the OH stretching involved in hydrogen bonds. After condensation (b) and polymerization (c) the decrease in peak intensity indicates the evaporation of solvents and the existence of terminal hydrolyzed groups of siloxanes mixtures. During the reactions Si-O-Si rocking absorption band at $\approx 440\text{ cm}^{-1}$ and Si-O-Si stretching signal at $\approx 1010\text{ cm}^{-1}$ has a sharp change in intensity (Figure 3.20(b,c)), confirming that condensation has occurred after heating at 50 °C for 7 h. Furthermore, the increased absorption intensity of the Si-C stretching bond at 800 cm^{-1} is attributed to the cyclic compound, which means that a more extended condensation network of siloxanes was formed where the alkyl groups do not interact with other function groups [218].

As condensation and photopolymerization proceeded, the typical for esters C=O absorption at 1720 cm^{-1} becomes broader and splits into two peaks due to the change of mobility of C=O bonds with gradual terminal double bond polymerization [217]. However, the C=C double bond peak at 1630 cm^{-1} remained even after exposure to UV light, indicating that the UV diode is not suitable for complete photopolymerization.

The most evident band rearrangements in FTIR spectra are observed after the polymer-to-ceramic phase transition. The material pyrolyzed at $1000\text{ }^{\circ}\text{C}$ have three peaks attributed solely to inorganic bonds (800 cm^{-1} Si-C; $\approx 440\text{ cm}^{-1}$ and $\approx 1010\text{ cm}^{-1}$ Si-O-Si rocking and stretching, respectively), indicating absence of organic residue after heating and an inorganic SiO_xC_y compound is formed (Figure 3.20(d)).

3.2.4 Thermogravimetric analysis

The preceramic polymers to the ceramic phase transition of MTMS:MAPTMS (9:1, 8:2, 7:3) polymerized samples were investigated by thermal gravimetric analysis up to $950\text{ }^{\circ}\text{C}$ under a nitrogen atmosphere. The thermal degradation/mass loss behavior (black curve), rate of mass loss (blue curve) and heat change measurements (red curve) are shown in Figure 3.21. Mass changes occur due to evaporation, decomposition, and ceramization. Thermogravimetric analysis showed that precursors almost completely decompose/ evaporate during the exothermal process at low temperatures (up to $300\text{ }^{\circ}\text{C}$) (residual weights of MAPTMS $\approx 2.2\%$, MTMS $\approx 0\%$).

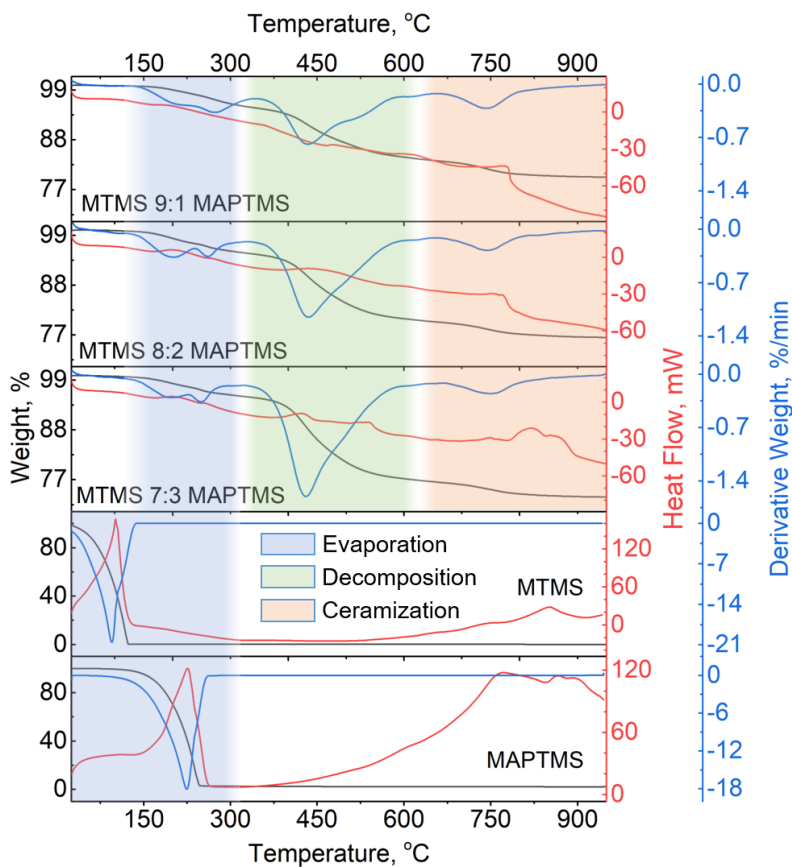


Figure 3.21: Thermogravimetric analysis data showing weight loss *vs* temperature (black curve), heat flow over a temperature range (red curve), and differential thermal analysis data (blue curve) of MTMS:MAPTMS (9:1, 8:2 and 7:3) polymers and initial precursors that are MTMS and MAPTMS.

It was observed that polymeric MTMS:MAPTMS samples are thermally stable up to 150 °C, as expected. Above this temperature, the thermal degradation of polymeric samples takes place in three stages. First, the mass of synthesized hybrid polymeric materials starts to decrease during the endothermal process at temperature interval 150 °C < *t* < 300 °C. This mass loss is attributed to the evaporation of unreacted precursors (residuals), which take up *ca.* 4-5% of all samples. The second and fastest endothermal mass loss at 350 °C < *t* < 600 °C temperature range indicates the decomposition of the organic moiety. During this step, the mass loss increased with increasing organic content in the prepared material. Sample with the most organic

content, MTMS:MAPTMS=7:3, resulted in highest mass loss, *i.e.*, 17.7%. Another sample where MTMS:MAPTMS ratio was equal to 8:2 lost 14.1% of its initial weight. While the polymer with the lowest amount of organic content (MTMS:MAPTMS=9:1) lost the lowest amount of its initial weight, *i.e.*, 10.7%. Finally, at the $650\text{ }^{\circ}\text{C} < t < 950\text{ }^{\circ}\text{C}$ temperature interval, amorphous SiO_xC_y was formed with 73.2% (MTMS:MAPTMS=7:3), 76.4% (MTMS:MAPTMS=8:2) and 79.8% (MTMS:MAPTMS=9:1) mass remaining. These results indicate that hydrolysis and condensation procedures are necessary. Otherwise, the precursors evaporate/decompose at low temperature without the phase transition into ceramics.

3.2.5 Study of crystallization processes

X-ray diffraction (XRD) analysis was used to study the composition and crystalline state after the pyrolysis. The results are shown in Figures 3.22, 3.24, 3.25. XRD patterns collected from MTMS:MAPTMS disk shape samples calcinated under the nitrogen atmosphere at the temperature range from $1000\text{ }^{\circ}\text{C}$ to $1500\text{ }^{\circ}\text{C}$ with a $100\text{ }^{\circ}\text{C}$ step are shown in Figures 3.22(a-f), 3.24(a-f), 3.25(a-f) for the sample with MTMS:MAPTMS ratio 9:1, 8:2, 7:3, respectively. Moreover, XRD patterns of materials heat treated at $1400\text{ }^{\circ}\text{C}$ under vacuum are depicted in Figures 3.22(b), 3.24(b), 3.25(b). Heating samples under vacuum up to $1300\text{ }^{\circ}\text{C}$ provided the same XRD patterns as heating under the nitrogen atmosphere (completely amorphous structures were formed) therefore, these patterns are not presented. Obtained data were compared to the reference patterns (see Figures 3.22(g), 3.24(g), 3.25(g)) of the Crystallography Open Database (COD).

The pure crystalline trigonal silicon carbide phase is identified after annealing the samples at a temperature of $1400\text{ }^{\circ}\text{C}$ in a vacuum, regardless of the ratio of precursors (Figures 3.22(b), 3.24(b), 3.25(b)), illustrating that the crystallization of trigonal SiC is promoted by the increased pyrolysis temperature. The crystal lattice pattern of trigonal silicon carbide is depicted in Figure 3.23(c).

Broad diffraction bands in patterns demonstrate that the samples were amorphous and had no crystalline structure after pyrolysis in the temperature range $1000\text{ }^{\circ}\text{C} < t < 1300\text{ }^{\circ}\text{C}$. Sharp but low-intensity peaks of trigonal alpha Si_3N_4 phase peaks appeared in the XRD pattern of MTMS:MAPTMS 9:1 sample, pyrolyzed at $1400\text{ }^{\circ}\text{C}$, indicating that the ceramic began to transform from amorphous to crystal state. However, the material was still mainly amorphous (see Figure 3.22(b)). Meanwhile, MTMS:MAPTMS 8:2 and 7:3 samples remained amorphous even after pyrolysis at $1400\text{ }^{\circ}\text{C}$ temperature (see Figure 3.24(b), 3.25(b)).

Lattice patterns of crystalline alpha and beta silicon nitride are shown in Figure 3.23. The significant change in XRD patterns was observed after pyro-

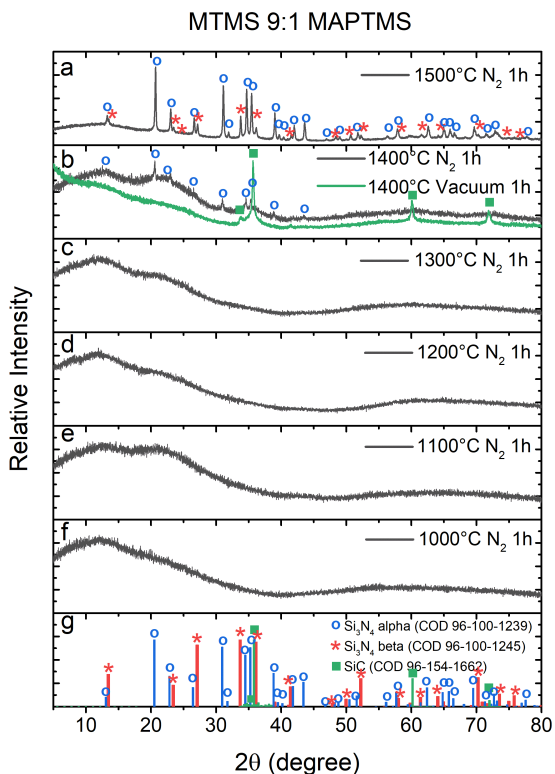


Figure 3.22: X-ray diffractograms of prepared 9:1 MTMS:MAPTMS ceramic plates heat treated in a temperature range from 1000 °C to 1500 °C (a-f) in a nitrogen atmosphere and at 1400 °C in a vacuum (b). Reference data (g).

lysis at 1500 °C. Sharp diffraction peaks seen in Figures 3.22 (a), 3.24 (a), 3.25(a) indicate that the precursors had successfully converted to trigonal alpha Si_3N_4 phase (lattice pattern is depicted in Figure 3.23(b)) which is predominant if compared to peaks of hexagonal beta Si_3N_4 .

Interestingly, the starting materials had no nitrogen atoms in their composition, thus proving that the samples are reacting with nitrogen gas resulting in silicon nitride production. Such reactions between solid SiO_xC_y (see Figure 3.23(a)) composite and nitrogen gas are explained in recent scientific publications [219–221]. Based on the literature, the formation and evolution process of Si_3N_4 ceramics can be divided into several stages. First of all, below 1200 °C, preceramic material is converted to a mixture of silicon oxide and carbon (SiO_xC_y composites). When the temperature reaches 1200 °C, SiO vapor and CO gas are released through carbothermic reduction between silicon oxide and carbon. Finally, SiO, C, and nitrogen gas conversion to CO gas and $\alpha\text{-Si}_3\text{N}_4$

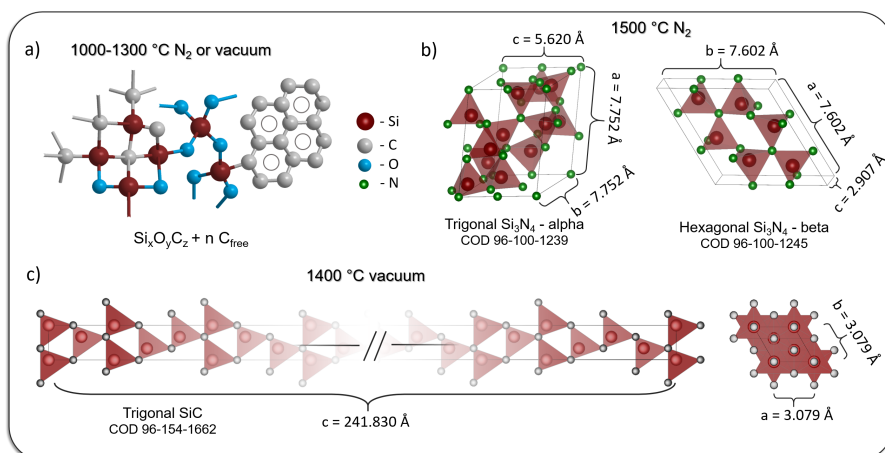


Figure 3.23: Crystalline structures obtained after heat treatments of silicon-organics at 1000-1300 °C under vacuum or N_2 atmosphere (a), at 1500 °C under N_2 atmosphere (b) and at 1400 °C under vacuum (c).

(a small amount of β - Si_3N_4 as a secondary phase can be also detected). Here, the nitrogen gas has two functions: as reactant and as a carrier gas to remove CO from the reaction sites, allowing the decomposition to proceed further. These results establish that the precursors were successfully converted to Si_3N_4 ceramic after pyrolysis at 1500 °C. However, the background of the XRD signal confirms the presence of a substantial amount of amorphous material.

3.2.6 3D fabrication prospects

3D structures such as a resolution array of lines with frames, fullerene-type models (with smaller fullerene inside) and gyroids were formed to investigate the potential of materials to participate in laser photopolymerization. The material MTMS 7:3 MAPTMS was too liquid after condensation to form a suitable height drop for laser photopolymerization, while in the case of MTMS 9:1 MAPTMS development of structures after photopolymerization was impossible due to the high degree of condensation. Therefore, 3D lithography is provided only for MTMS 8:2 MAPTMS material (see Figures 3.26 and 3.27).

The resolution test of MTMS:MAPTMS 8:2 material was performed by fabricating a resolution array of structures. The production velocity was adjusted in increments of 50 $\mu m/s$, ranging from 50 $\mu m/s$ to 500 $\mu m/s$, while the power was varied in increments of 20 μW , from 20 μW to 220 μW (see Figure 3.26). The structure produced using 40 μW laser power and 150 $\mu m/s$ fabrication speed had the smallest feature size. The average polymeric line

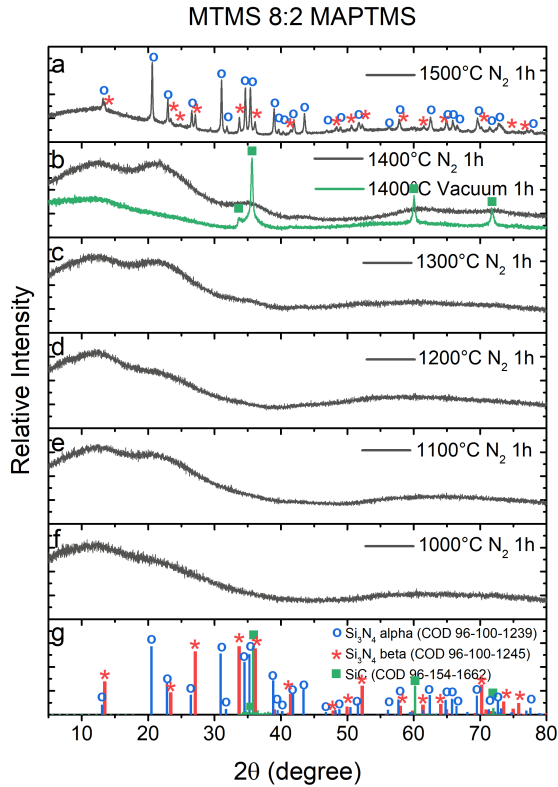


Figure 3.24: X-ray diffractograms of prepared 8:2 MTMS:MAPTMS ceramic plates heat treated in a temperature range from 1000 °C to 1500 °C (a-f) in a nitrogen atmosphere and at 1400 °C in a vacuum (b). Reference data (g).

thickness was 717.2 ± 83 nm (Figure 3.26(d)). The capillary forces that acted during development caused the merging of vertical lines. In order to avoid merging, the development must be carried out using a critical point dryer (CPD).

The structures chosen for larger dimensions derivatives fabrication experiments were gyroids and fullerene-type models with smaller fullerene inside. With this configuration, it is possible to determine several important factors. First, the gyroid shows if it is possible to produce true cubic periodic 3D structures. Fullerene-type models provide information about the production possibilities of thin features and of hollow round shapes.

Gyroids and fullerene-type model fabrication were carried out using 515 nm wavelength radiation, at repetition rates 200 kHz and pulse duration 300 fs, focused by an objective lens with 20x 0.8 NA using 1.0 mW incident irradiation

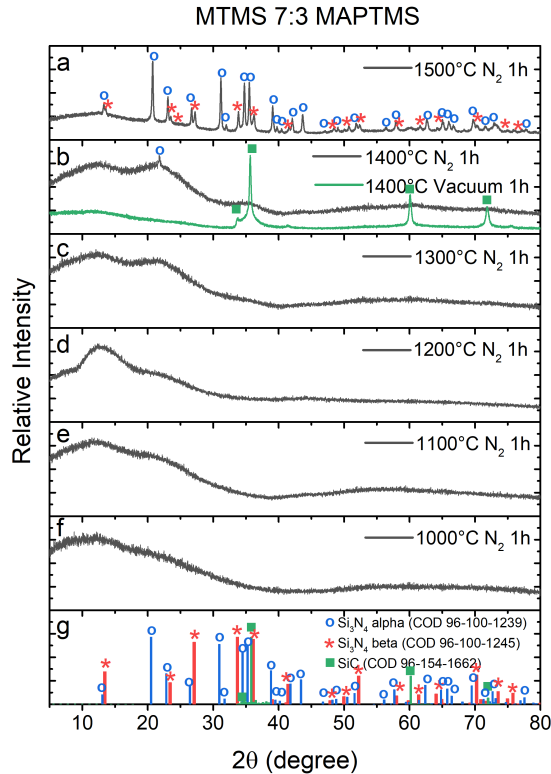


Figure 3.25: X-ray diffractograms of prepared 7:3 MTMS:MAPTMS ceramic plates heat treated in a temperature range from 1000 °C to 1500 °C (a-f) in a nitrogen atmosphere and at 1400 °C in a vacuum (b). Reference data (g).

power and 10 mm/s speed [12]. In order to evaluate surface and shape deformations after high temperature treatment all 3D structures were annealed in the temperature range of 1000-1500 °C in a nitrogen atmosphere. Derivatives with good quality (green) with insignificant cracks (yellow) and with severe cracks or slight melting (red) are depicted and outlined in Figure 3.27. It is evident that the gyroids retained their shape in the entire temperature range even after reaching the Si₃N₄ crystalline phase. However, slight cracks were recognized on the surface of a structure after heat treatment at 1200 °C (Figure 3.27(m)), which became more pronounced as the temperature increased (Figure 3.27(r,w)).

Further, it was observed that after heat treatment at the highest temperature, the structure started to melt in the contact zone between the structure and the corundum substrate (see Figure 3.27(u)). This consequence can be explained by

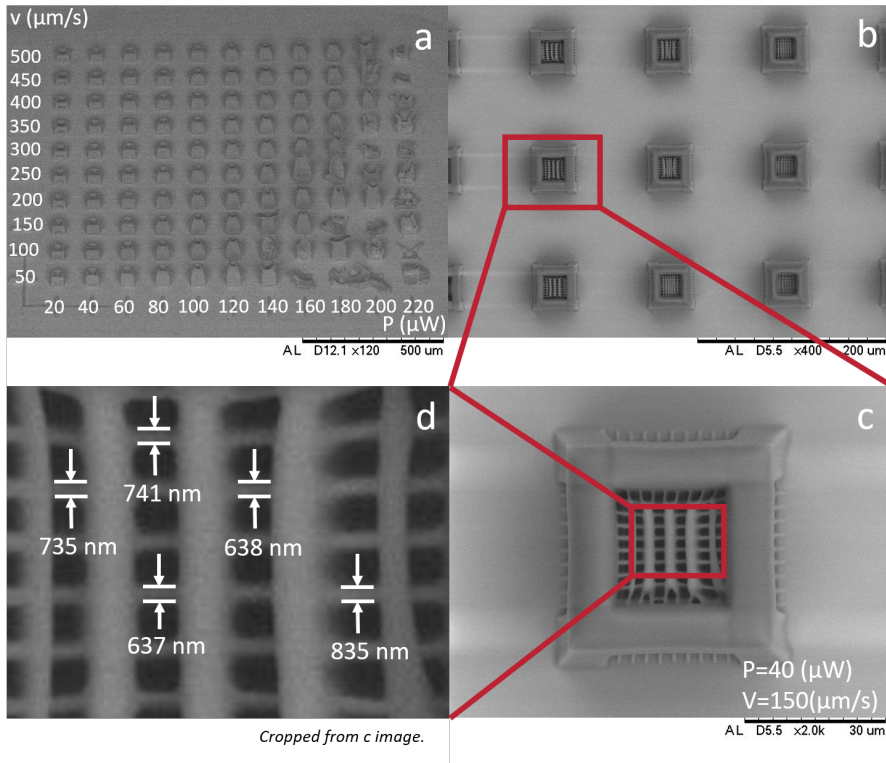


Figure 3.26: SEM images of resolution array of MTMS:MAPTMS 8:2 polymeric structures (a,b), one of the structures in the array is shown in greater detail (c), cropped and zoomed part of (c) image with marked sizes of lines (d). Code authored by Linas Jonušauskas.

the higher thermal conductivity of solids than gases. Nevertheless, the visual quality of the ceramic structures is improved more than published in other similar studies [144, 160], even after processing at such high temperatures.

Fullerene-type models, which are less bulk-filled than gyroids, showed excellent structure quality even up to 1400 °C temperature treatment. The higher ratio of surface area and volume (in the case of the fullerene-type model) resulted in an easier escape of CO gas from the structure volume during the previously described Si_3N_4 synthesis reaction. Consequently, fewer defects are presented after the highest temperature treatment.

3.2.7 Investigation of mechanical properties

The mechanical properties of ceramics are one of the most important features. In order to evaluate the hardness of ceramic plates nine indents, arrayed in a

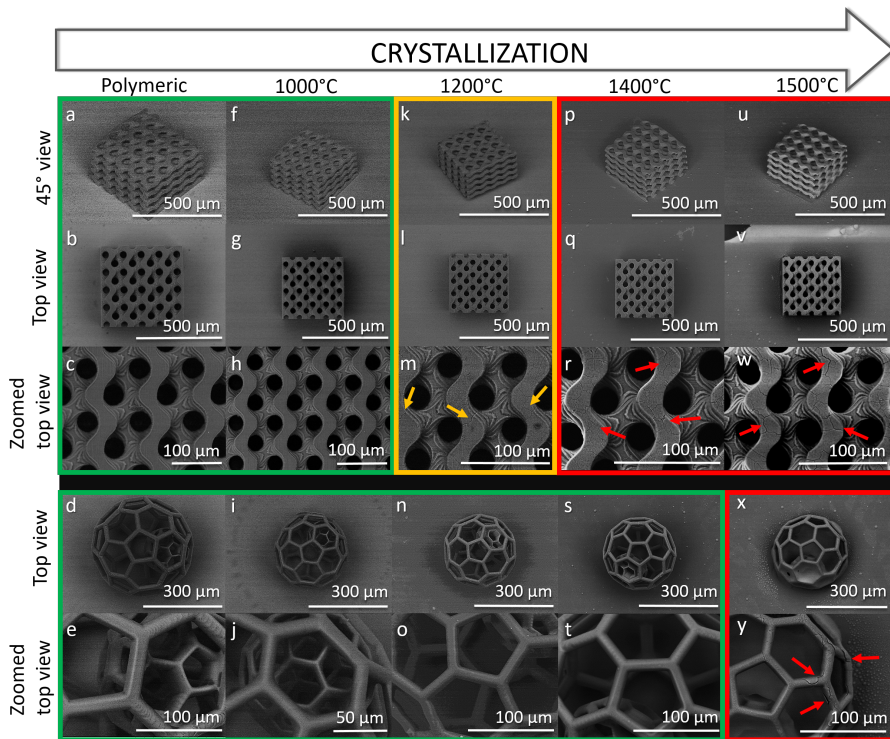


Figure 3.27: SEM images of polymeric (a-e) and ceramic (heat-treated at 1000 °C (f-j), 1200 °C (k-o), 1400 °C (p-t), 1500 °C (u-y) in a nitrogen atmosphere) gyroids and fullerene-type models, with the smaller fullerene inside the structure, fabricated using MTMS 8:2 MAPTMS material. Structures with good quality (green) with insignificant cracks (yellow) and with severe cracks or slight melting (red) are outlined and marked with arrows.

square (Figure 3.28), were made using a load-controlled indentation method with peak loads from 100 mN to 5 N.

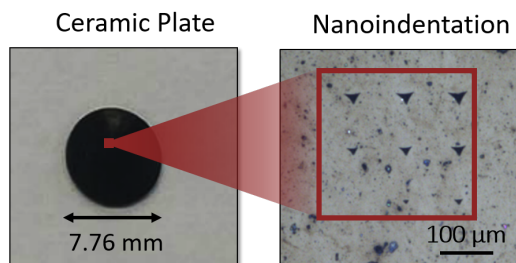


Figure 3.28: 3D ceramic plate with nine indents on the surface.

Figure 3.30(a) shows the average Berkovich hardness dependency and average reduced elastic modulus of sintered ceramic plate samples as a function of the sintering temperature. All experimental data are provided in Appendix Tables A.7, A.8. The optimization of sintering temperature was made for each MTMS:MAPTMS composition. Averages of mechanical properties were calculated using Berkovich hardness and reduced elastic modulus relationship on applied loads data depicted in Figure 3.29.

Reduced elastic modulus is a physical quantity that determines the resistance of a material to compression or tension. Meanwhile, hardness measurement shows the resistance of a sample deformation due to a constant compression load from a diamond indenter [222]. The tests work on the basic premise of measuring the critical dimensions of an indentation left by a specifically dimensioned and loaded indenter. Therefore, the measured hardness is not a result of the shape of the structure, but a property of the specific material. It can be seen that the maximum hardness and reduced elastic modulus were measured for MTMS:MAPTMS 8:2 sample sintered at 1200 °C, respectively 14.33 ± 1.17 GPa and 104.99 ± 1.81 GPa. The general trend which can be observed from Figure 3.30(a) and b is that the hardness and reduced elastic modulus increase from 1000 °C to 1200 °C. However, the further increase of the temperature (values higher than 1200 °C) results in decreasing of the values of mechanical properties. These results coincide with defects that have started to appear in the structure and can be seen in Figure 3.27(m,r,w). All data sets, except for samples annealed at 1500 °C, and all reduced elastic modules, except for 7:3 samples, annealed at 1000 °C and 1500 °C, were higher than the fused quartz standard (FQ) (PN: 5-0098-2) (FQ hardness- 10.39 ± 0.34 GPa, FQ reduced elastic modulus- 69.45 ± 1.17 GPa). However, the large standard deviations of the values at high temperatures can be explained by the inhomogeneity of the material (severe cracks). Nevertheless, demonstrated hardness results are truly stunning in comparison with other reported results.

In addition to hardness, the synthesized material density data also were evaluated. Figure 3.31 displays the linear shrinkage (a) and the bulk density (b) of the polymeric and sintered MTMS:MAPTMS (9:1, 8:2 and 7:3) samples as a function of the sintering temperature. The increase in the heating temperature caused linear shrinkage and density to increase with logarithmic progression. This increase was due to the structural change and compactness of the sample structure after the heat-treatment process. The linear shrinkage reached 22.62%, 23.66% and 25.50% for MTMS:MAPTMS 9:1, 8:2 and 7:3 samples, after the highest 1500 °C temperature heat treatment. The mixture with a higher organic proportion (7:3) shrank the most in the whole temperature range. The numerical values of all shrinkages are listed in Appendix Table A.9.

As shown in Figure 3.31(b) densities of MTMS:MAPTMS 9:1, 8:2 and 7:3 polymeric samples increased from 1.32, 1.30, 1.30 g/cm³ to 2.33, 2.28, 2.23 g/cm³

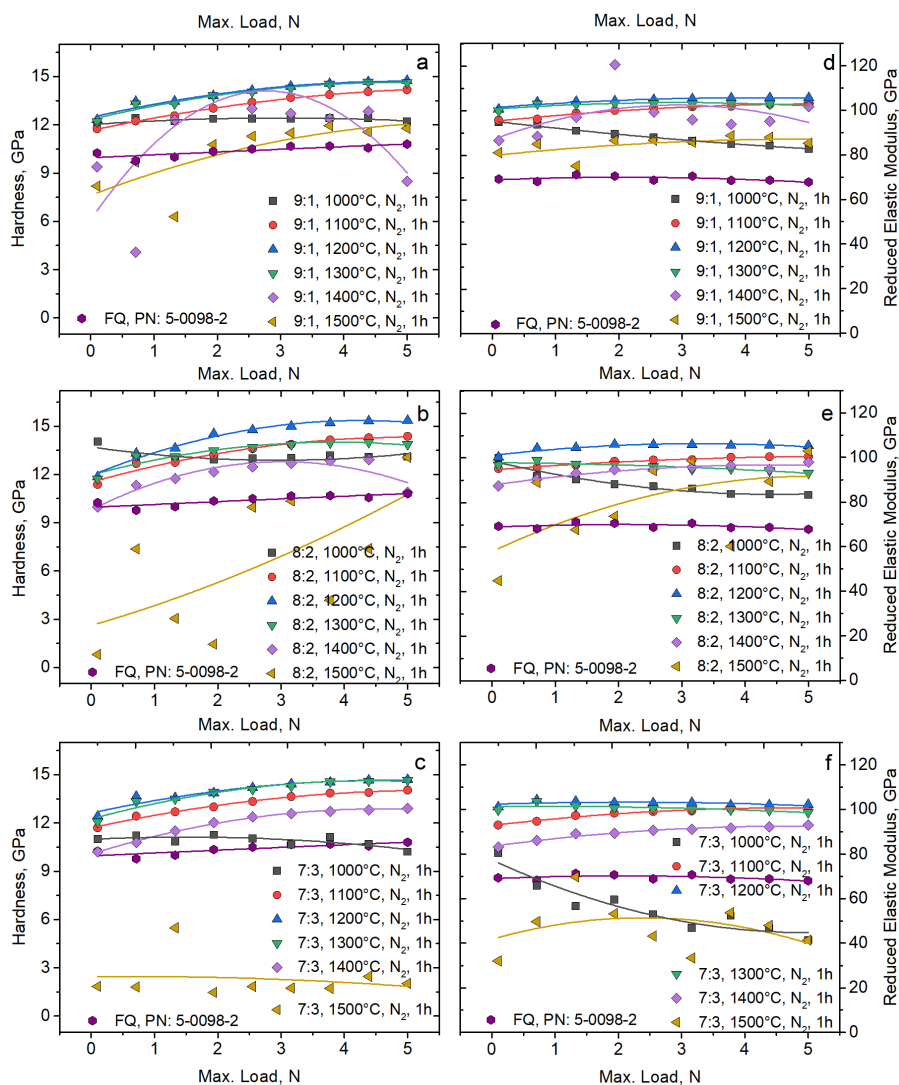


Figure 3.29: Hardness (a, b, c) and reduced elastic modulus (d, e, f) dependence on applied loads for prepared MTMS:MAPTMS (9:1, 8:2 and 7:3) ceramic plates after heat treatment in a nitrogen atmosphere at a temperature range from 1000 °C to 1500 °C in a comparison with a fused quartz reference (PN:5-0098-2).

after crystallization. The numerical values of densities are listed in Appendix Table A.10. The mixture with the lowest organic content in the starting material (9:1) had the highest density in the entire temperature range. No fractional porosity of the ceramic samples was observed (see Figure 3.27), therefore, specimens density and shrinkage are mostly determined by the type of their

individual constituents and their change with increasing temperature. The low-density ceramics achieved allow the manufacturing of lighter structures in the technology field.

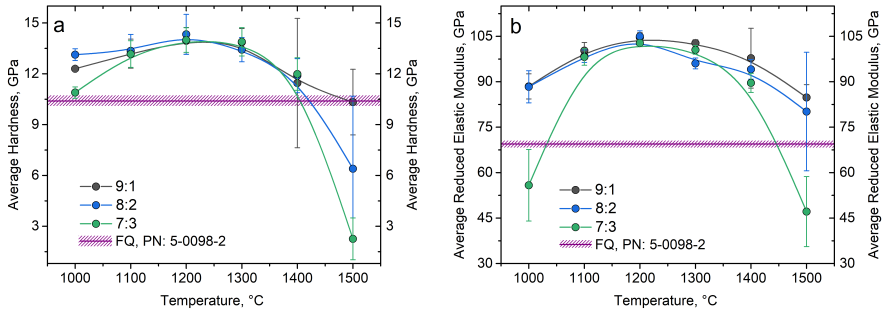


Figure 3.30: Average hardness (a) and reduced elastic modulus (b) dependence on prepared MTMS:MAPTMS (9:1, 8:2 and 7:3) ceramic plates heating temperature in a comparison with a fused quartz reference (PN: 5-0098-2). Hardness and reduced elastic modulus dependence on applied loads for prepared MTMS:MAPTMS (9:1, 8:2 and 7:3) ceramic plates are depicted in Figure 3.29.

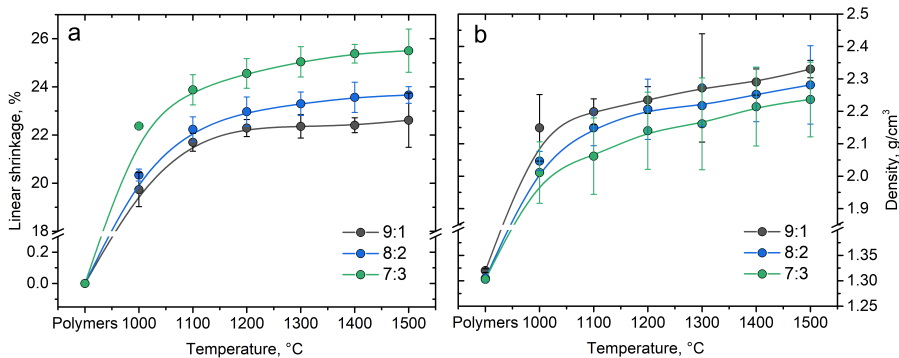


Figure 3.31: The variation of linear shrinkage (a) and bulk density (b) of prepared MTMS:MAPTMS (9:1, 8:2 and 7:3) polymeric, glass and ceramic samples at various sintering temperatures in a nitrogen atmosphere.

3.2.8 Technical application in micro-optics

Recently, there is a growing demand to combine the production of transparent and opaque 3D structures [223]. Photopolymerization of opaque resins is very difficult or impossible due to light absorption in the Ultraviolet-Visible-

Near Infrared (UV-VIS-NIR) region. Here was demonstrated that it is possible to produce black structures without process limitations, since the initial resin is transparent to UV-VIS, and opaque structures are obtained only after post-processing. The transparency of the initial polymeric material and the absorption of ceramics were quantitatively determined by transmittance measurement in the UV-VIS region. Optical microscope images of MTMS:MAPTMS 8:2 3D polymeric and opaque ceramic structures together with transmission spectra of gel, polymer and ceramic discs are introduced in Figure 3.32(a,b,c). The ceramic has demonstrated complete absorption in the UV-VIS range, while the gel transmits up to 70.6% of visible light, depending on the wavelength. Therefore, such a fabrication method can be used in mechanically proof micro-optic manufacturing. Transparent polymer is appropriate for lens production, and opaque ceramics for the fabrication of microscopic apertures with increased contrast of 3D-printed micro-optics.

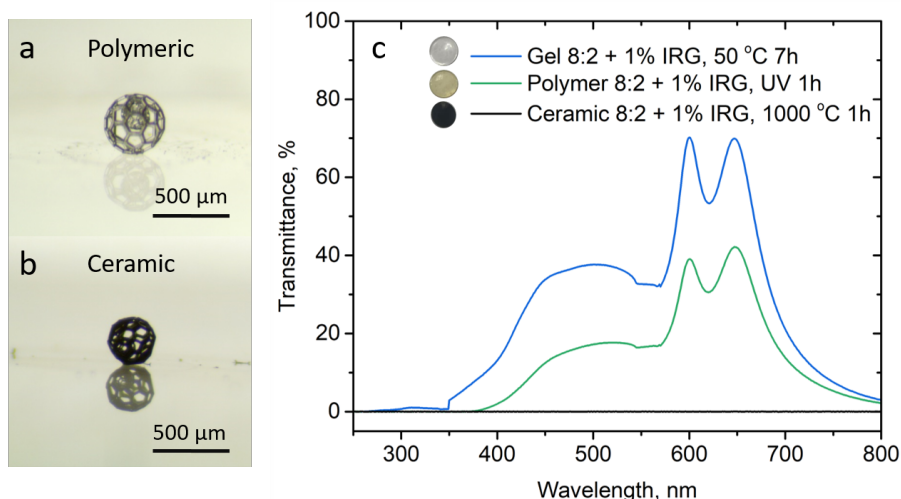


Figure 3.32: Optical microscope images of MTMS:MAPTMS 8:2 polymeric (a) and ceramic fullerenes after heat treatment at 1000 °C temperature (b). Spectra showing MTMS:MAPTMS 8:2 gel, polymer and black ceramic discs transmittance (c) to UV-VIS light. The thickness of the discs for the UV-VIS measurement was 1 mm. The ceramic disc shows complete absorption in the UV-VIS light range.

3.2.9 Conclusions on manufacturing of 3D hard ceramic structures

Achieved mechanical properties and demonstrated tunability of material (amorphous SiOC, SiC and α,β -Si₃N₄) make it a milestone advance in the laser applications field of mechanically hard devices manufacturing. The

highest achieved Berkovich hardness was 14.33 ± 1.17 GPa and reduced elastic modulus 104.99 ± 1.81 GPa for MTMS:MAPTMS 8:2 material, annealed at 1200°C . This material was characterized by a low density (2.21 ± 0.09 g/cm³) and an amorphous state of SiOC. Because of its hardness and high thermal stability, the produced ceramic is suitable as pressing molds for micro-optic fabrication from fused quartz. Also, due to opacity ceramics is appropriate for the manufacturing of microscopic apertures.

The materials synthesized using MTMS and MAPTMS are suitable for the production of micro-optics due to the visible light transmittance of the polymeric material (for the optical element) and the impermeable ceramic structures (for the apertures).

In perspective, the industry of micro-mechanics will benefit from this investigation as it reveals the potential for manufacturing 3D high spatial resolution and high solid ceramic structures. Such technology is in a perfect match with the direction for downscaling and increasing functionalities of novel crystalline ceramics structures that are precise, mechanically proof, light, and defect-free without resolution limits.

4. CONCLUSIONS

1. The sol-gel synthesis technique is a viable method for producing transparent organometallic compounds using precursors such as 3-methacryloxypropyltrimethoxysilane and zirconium propoxide, with molar ratios ranging from 9:1 to 5:5, and trimethoxymethylsilane and 3-methacryloxypropyltrimethoxysilane, ranging from 9:1 to 7:3. The resulting materials synthesized through this technique can be utilized for laser 3D photopolymerization.
2. The resolution of inorganic 3D objects is dependent on various factors including the composition of the photoactive material (3-methacryloxypropyltrimethoxysilane : zirconium propoxide from 9:1 to 5:5), laser parameters during photopolymerization (fabrication velocities 200 $\mu\text{m/s}$ and 500 $\mu\text{m/s}$, laser powers 48 μW , 56 μW , 64 μW), and heating protocol. By selecting 9:1 (3-methacryloxypropyltrimethoxysilane : zirconium propoxide) precursor, 200 $\mu\text{m/s}$ fabrication velocity, 64 μW laser power and heat treatment at 1000 °C under air atmosphere it is possible to achieve a ceramic object resolution of up to 60 nm.
3. The crystalline phases of powders and 3D objects with identical initial compositions exhibit structural variations in the range of starting materials (3-methacryloxypropyltrimethoxysilane : zirconium propoxide) from 9:1 to 5:Zr and the heating protocol from 1000 °C to 1400 °C temperature under air atmosphere. ZrSiO_4 (COD 96-900-0692) crystalline phase was obtained for 9:1 3D object and for 7:3, 6:4 powders heat-treated at 1400 °C under air atmosphere.
4. The mechanical properties of inorganic 3D objects are dependent on the composition of the starting photoactive material (trimethoxymethylsilane : 3-methacryloxypropyltrimethoxysilane from 9:1 to 7:3) and the heating protocol (from 1000 °C to 1500 °C under nitrogen atmosphere). It

is possible to obtain 3D inorganic objects that are harder than fused quartz. The maximum value of Berkovich hardness as high as 14.33 ± 1.77 GPa and an elastic modulus of 104.99 ± 1.81 GPa were achieved for 8:2 (trimethoxymethylsilane : 3-methacryloxypropyltrimethoxysilane) sample sintered at 1200 °C.

5. Synthesized 8:2 (trimethoxymethylsilane : 3-methacryloxypropyltrimethoxysilane) material is suitable for the production of micro-optics due to the polymeric material transmittance up to 70.6% to visible light ($\approx 350-700$ nm) (for the optical element manufacturing) and the impermeable of the ceramic 3D object (for the apertures).

PUBLICATIONS INCLUDED IN THE THESIS

Articles in Journals

- A1. **G. Merkininkaitė**, D. Gailevičius, S. Šakirzanovas, L. Jonušauskas. „Polymers for Regenerative Medicine Structures Made via Multiphoton 3D Lithography: a Review“. *International Journal of Polymer Science*. Vol. 2019, 3403548, 23, 2019, doi.: 10.1155/2019/3403548.
- A2. **G. Merkininkaitė**, E. Aleksandravičius, M. Malinauskas, D. Gailevičius, S. Šakirzanovas. „Laser additive manufacturing of Si/ZrO₂ tunable crystalline phase 3D nanostructures“. *Opto-Electronic Advances*. Vol. 5, No. 5, 210077, 2022, doi.: 10.29026/oea.2022.210077.
- A3. **G. Merkininkaitė**, D. Gailevičius, L. Staišiūnas, E. Ežerskytė, R. Vargalis, M. Malinauskas and S. Šakirzanovas. „Additive Manufacturing of SiOC, SiC, Si₃N₄ Ceramic 3D Micro-Structures“. *Advanced Engineering Materials*, 2023, doi.: 10.1002/adem.202300639.

Book Chapter

- B1. **G. Merkininkaitė**, E. Aleksandravičius, S. Varapnickas, D. Gailevičius, S. Šakirzanovas, M. Malinauskas: „Multi-photon 3D lithography for sub-100 nm additive manufacturing of inorganics“. In: Stoian, R., Bonse, J. (eds) *Ultrafast Laser Nanostructuring*. Springer Series in Optical Sciences. Vol 239. Springer, Cham. Chapter No. 22, 2023, doi.: 10.1007/978-3-031-14752-422.

Patent Application

- P1. **G. Merkininkaitė**, D. Gailevičius, S. Šakirzanovas (2022). "A method for production of a photo-curable inorganic-organic hybrid resin and a method for production of hard SiO_xC_y ceramic microstructures using the photo-curable inorganic-organic hybrid resin". Patent application no. LT2022537. Patent submission no. 107277. Submitted on September 14 (2022).

ATTENDED CONFERENCES

Oral Presentations

- O1. **G. Merkininkaitė**, V. Padolskytė, D. Gailevičius, M. Malinauskas, S. Šakirzanovas. "Preparation and characterization of metal-organic precursors for laser fabrication of 3D ceramic micro-/nano-structures", Open Readings 2019, 62rd international conference for students of physics and natural sciences Vilnius, Lithuania, March 19-22 (2019).
- O2. D. Gailevičius, V. Padolskytė, **G. Merkininkaitė**, L. Mikoliūnaitė, S. Šakirzanovas, S. Juodkakis, M. Malinauskas. „True 3D Additive-Manufacturing of Glass-Ceramic down to Nanoscale“. CLEO/EUROPE-EQEC, Munich, Germany, June 23-27 (2019).
- O3. E. Aleksandravičius, V. Padolskytė, D. Gailevičius, **G. Merkininkaitė**, S. Šakirzanovas, L. Mikoliūnaitė, S. Juodkakis, M. Malinauskas. "Nano/Micro-additive inorganic direct laser structuring via multiphoton polymerization". APPOLO 2019. Vilnius, Lithuania, July 07-12 (2019).
- O4. D. Gailevičius, **G. Merkininkaitė**, V. Padolskytė, S. Šakirzanovas, V. Mizeikis, S. Juodkakis, M. Malinauskas „Nanoscale 3D Laser Additive-Manufacturing of Highly-Resilient Glass-Ceramics“. SPIE Defence. Strasbourg, France, September 9-12 (2019).
- O5. **G. Merkininkaitė**, D. Gailevičius, R. Vargalis, S. Šakirzanovas, L. Jonušauskas. "Fabrication optimization and post-processing solutions for high-resolution 3D laser lithography". International Conference on Nanoscience, Nanotechnology and Advanced Materials. Czech Republic, March 21-22 (2020).
- O6. **G. Merkininkaitė**, E. Aleksandravičius, D. Gailevičius, M. Malinauskas, S. Šakirzanovas. "Preparation of 3D glass ceramic micro-/nanostructures by combining laser nanolithography with calcination". International Conference SPIE Photonics Europe. France, March 31 (2020).
- O7. **G. Merkininkaitė**, E. Aleksandravičius, D. Gailevičius, M. Malinauskas, S. Šakirzanovas. „Glass-ceramic crystalline 3D micro-/nano-structures: preparation to application“. 21th International Symposium on Laser Precision Microfabrication. Germany, June 24 (2020).
- O8. D. Gailevičius, **G. Merkininkaitė**, D. Andrijev, D. Andriukaitis, H. Gričius, Rokas Vargalis, L. Jonušauskas, S. Šakirzanovas. "3D Additive manufacturing of shape shifting scaffolds: polymeric and ceramic solutions". Additive Manufacturing Meets Medicine 2020, online, September 9-11 (2020).

- O9. L. Jonušauskas, T. Baravykas, R. Vargalis, D. Andriukaitis, H. Gričius, E. Ežerskytė, D. Andriječ, **G. Merkininkaitė**, A. Žemaitis, A. Butkutė, T. Tičkunas, D. Gailevičius. "Free-form 3D direct laser writing for medical applications". SPIE Photonics West 2021, March 6-11 (2021).
- O10. S. Varapnickas, M. Ryu, D. Gailevičius, T. Suzuki, **G. Merkininkaitė**, S. Šakirzanovas, J. Morikawa, S. Juodkasis, M. Malinauskas. "Glassy free-form 3D micro-optics enabled via ultrafast laser 3D nanolithography". SPIE Photonics West 2021. March 6-11 (2021).
- O11. G. Nemickas, D. Čereška, G. Kontenis, A. Žemaitis, **G. Merkininkaitė**, S. Šakirzanovas, L. Jonušauskas. "Femtosecond surface structuring: wettability, friction control and surface chemistry". SPIE Photonics West 2021, March 6-11 (2021).
- O12. D. Gailevičius, **G. Merkininkaitė**, S. Šakirzanovas, M. Malinauskas. „Calcination: the enabler of next-gen additive inorganic 3D structuring“. SPIE Photonics West 2022, San Francisco, January 22-27 (2022).
- O13. **G. Merkininkaitė**, E. Aleksandravičius, D. Gailevičius, M. Malinauskas, S. Šakirzanovas. „Optimization of multi-photon polymerization and thermal post-treatment for free-form glass-ceramic nano/microstructures manufacturing“. 23th International Symposium on Laser Precision Microfabrication. Germany, Dresden, June 7-10 (2022).
- O14. **G. Merkininkaitė**, E. Aleksandravičius, D. Gailevičius, M. Malinauskas, S. Šakirzanovas. „Additive manufacturing of inorganic 3D nanostructures by combining laser lithography and pyrolysis“. International Conference of Functional Inorganic Materials 2022. Lithuania, Vilnius, October 6-8 (2022).

Poster Presentations

- S1. **G. Merkininkaitė**, V. Padolskytė, E. Aleksandravičius, D. Gailevičius, M. Malinauskas, S. Šakirzanovas. „Application of metalorganic precursors for laser fabrication“. Nanostructured bioceramic materials 2020. Vilnius, Lithuania, December 1-3 (2020).
- S2. **G. Merkininkaitė**, E. Aleksandravičius, M. Malinauskas, D. Gailevičius, S. Šakirzanovas. „Laser additive manufacturing of crystalline 3D nanostructures“. 64th international conference for physics and natural sciences students, Open Readings 2021, Vilnius, Lithuania, March 16-19 (2021).
- S3. **G. Merkininkaitė**, E. Aleksandravičius, D. Gailevičius, M. Malinauskas and S.Šakirzanovas. „Optimization of multi-photon polymeriza-

tion and thermal post-treatment for free-form glass-ceramic nano/micro-structures manufacturing". „4th International Conference on Optics, Photonics and Lasers (OPAL' 2021)", Corfu, Greece, October 13-15 (2021).

PUBLICATIONS NOT INCLUDED IN THE THESIS

Articles in Journals

- N1. M. Janulevičius, J. Grigorjevaitė, **G. Merkininkaitė**, S. Šakirzanovas, A. Katelnikovas, "Luminescence and luminescence quenching of $\text{Eu}_2\text{Mo}_4\text{O}_{15}$ ". *Journal of Luminescence*, 179, pp. 35-39, 2016.
doi.: 10.1016/j.jlumin.2016.06.050.
- N2. D. Gonzalez-Hernandez, S. Varapnickas, **G. Merkininkaitė**, A. Čiburys, D. Gailevičius, S. Šakirzanovas, S. Juodkazis, M. Malinauskas, „Laser 3D Printing of Inorganic Free-Form Micro-Optics“. „*Photonics*“, 2021, 8(12), 577. doi.: 10.3390/photonics8120577.
- N3. A. Butkutė, **G. Merkininkaitė**, T. Jurkšas, J. Stančikas, T. Baravykas, R. Vargalis, T. Tičkūnas, J. Bachmann, S. Šakirzanovas, V. Sirutkaitis and L. Jonušauskas. „Femtosecond Laser-Assisted 3D Etching Using Inorganic-Organic Etchant“. *Materials* 2022, 15(8), 2817; doi.: 10.3390/ma15082817.
- N4. E. Ežerskytė, M. Vengris, K. Gineitis, **G. Merkininkaitė**, B. Leber, R. Vargalis, P. Stiegler, P. Schemmer, S. Šakirzanovas, A. Kielaitė-Gulla, K. Strupas, L. Jonušauskas. „Qualitative comparison between different biopolymers for usage in two-photon polymerization towards liver regeneration“. *Optical Materials Express*, Optica Publishing Group, Vol.12, 7, pp. 2550-2567, 2022, doi.: 10.1364/OME.459057.
- N5. A. Butkutė, T. Jurkšas, T. Baravykas, B. Leber, **G. Merkininkaitė**, R. Žilėnaitė, D. Čereška, A. Gulla, M. Kvietkauskas, K. Marcinkevičiūtė, P. Schemmer, K. Strupas. "Combined Femtosecond Laser Glass Microprocessing for Liver-on-Chip Device Fabrication". *Materials*, MDPI, vol. 16, 2174, 2023, doi.: 10.3390/ma16062174.
- N6. **G. Merkininkaitė**, A. Zabiliūtė-Karaliūnė, T. Jüstel, V. Klimkevičius, S. Šakirzanovas, A. Katelnikovas „ $\text{Ce}^{3+} \rightarrow \text{Cr}^{3+}$ energy transfer in $\text{Y}_3\text{Al}_3\text{MgSiO}_{12}$ garnet host and application in horticultural lighting“. *Ceramics International*, Elsevier, vol. 49, 11, 2023, pp. 16796-16808, 2023, doi.: 10.1016/j.ceramint.2023.02.040.

- M1. A. Butkutė, **G. Merkininkaitė**, T. Baravykas, T. Jurkšas, J. Stančikas, T. Tičkūnas, L. Jonušauskas, V. Sirutkaitis. „Selective laser etching of high aspect ratio 3D glass microstructures“, Proceedings Volume PC11992, Laser 3D Manufacturing IX; PC119920D, 2022, doi.: 10.1117/12.2609758.
- M2. D. Gailevičius, **G. Merkininkaitė**, S. Šakirzanovas, M. Malinauskas. „Calcination: the enabler of next-gen additive inorganic 3D structuring“. Proceedings Volume PC12012, Advanced Fabrication Technologies for Micro/Nano Optics and Photonics XV; PC120120T, 2022, doi.: 10.1117/12.2608928.
- M3. S. Varapnickas, M. Ryu, D. Gailevičius, T. Suzuki, **G. Merkininkaitė**, S. Šakirzanovas, J. Morikawa, S. Juodkasis, M. Malinauskas. „Glassy free-form 3D micro-optics enabled via ultrafast laser 3D nanolithography“. Proceedings Volume 11696, Advanced Fabrication Technologies for Micro/Nano Optics and Photonics XIV; 1169610, 2021, doi.: 10.1117/12.2578469.
- M4. L. Jonušauskas, D. Andriječ, D. Andriukaitis, R. Vargalis, T. Baravykas, A. Stankevičius, **G. Merkininkaitė**, A. Pautienius, H. Gričius, E. Ežerskytė, E. Šimkutė, A. Butkutė, J. Grigas, S. Šakirzanovas. „Expansion of Direct Laser Writing (DLW) Capabilities for Usage in Biomedical Applications“. „Laser 3D Manufacturing VIII“, Proceedings of SPIE - The International Society for Optical Engineering, 2021, 11677,1167713, doi.: 10.1117/12.2579245.
- M5. G. Nemickas, D. Čereška, G. Kontenis, A. Žemaitis, **G. Merkininkaitė**, S. Šakirzanovas, L. Jonušauskas. „Femtosecond surface structuring: wettability, friction control and surface chemistry“. „Laser-based Micro- and Nanoprocessing XV“, Proceedings of SPIE Vol. 11674, 116740Q, 2021, doi.: 10.1117/12.2578355.
- M6. **G. Merkininkaitė**, D. Gailevičius, R. Vargalis, S. Šakirzanovas, L. Jonušauskas. „Fabrication Optimization and Post-Processing Solutions for High-Resolution 3D Laser Lithography“, „International Journal of Advances in Science, Engineering and Technology (IJASEAT)“, 2020.
- M7. D. Gailevičius, **G. Merkininkaitė**, D. Andriukaitis, H. Gričius, R. Vargalis, D. Andriječ, L. Jonušauskas, and S. Šakirzanovas. „3D Additive manufacturing of shapeshifting scaffolds: polymeric and ceramic solutions“. „Transactions on Additive Manufacturing Meets Medicine“. Trans. AMMM, Vol 2, No 1, 2020, Article ID 010, doi.: 10.18416/AMMM.2020.2009010.

- M8. **G. Merkininkaitė**, E. Aleksandravičius, D. Gailevičius, S. Varapnickas, M. Malinauskas, S. Šakirzanovas. „Preparation of 3D glass ceramic micro/nanostructures by combining laser nanolithography with calcination“. Proceedings Volume 11349, 3D Printed Optics and Additive Photonic Manufacturing II; 113490E, 2020, doi.: 10.1117/12.2555838.
- M9. D. Gailevičius, **G. Merkininkaitė**, V. Padolskyte, S. Varapnickas, M. Ryu, J. Morikawa, V. Mizeikis, S. Šakirzanovas, S. Juodkasis, M. Malinauskas. „Nanoscale 3D laser additive manufacturing of highly resilient glass ceramics“. Proceedings Volume 11168, Advanced Manufacturing Technologies for Micro- and Nanosystems in Security and Defence II; 111680F, 2019, doi.org/10.1117/12.2532804.

BIBLIOGRAPHY

- [1] R. Janssen, S. Scheppokat, and N. Claussen, "Tailor-made ceramic-based components—Advantages by reactive processing and advanced shaping techniques," *J. Eur. Ceram. Soc.*, vol. 28, no. 7, pp. 1369 – 1379, 2008.
- [2] Y.-L. Zhang, Q.-D. Chen, H. Xia, and H.-B. Sun, "Designable 3d nanofabrication by femtosecond laser direct writing," *Nano Today*, vol. 5, no. 5, pp. 435–448, 2010.
- [3] M. Mangirdas, A. Žukauskas, S. Hasegawa, Y. Hayasaki, V. Mizeikis, R. Buividas, and S. Juodkasis, "Ultrafast laser processing of materials: from science to industry," *Light Sci. Appl.*, vol. 5, p. 16133, 2016.
- [4] D. Gailevičius, V. Padolskytė, L. Mikoliunaite, S. Sakirzanovas, S. Juodkasis, and M. Malinauskas, "Additive-manufacturing of 3D glass-ceramics down to nanoscale resolution," *Nanoscale Horizons*, vol. in press, 2018.
- [5] T. Frenzel, M. Kadic, and M. Wegener, "Three-dimensional mechanical metamaterials with a twist," *Science*, vol. 358, no. 6366, pp. 1072–1074, 2017.
- [6] R. Liang, Y. Gu, Y. Wu, V. Bunpetch, and S. Zhang, "Lithography-based 3d bioprinting and bioinks for bone repair and regeneration," *ACS biomaterials science & engineering*, vol. 7 3, pp. 806–816, 2021.
- [7] D. L. G. Hernandez, S. Varapnickas, G. Merkininkaite, A. Ciburys, D. Gailevičius, S. Sakirzanovas, S. Juodkasis, and M. Malinauskas, "Laser 3D printing of inorganic free-form micro-optics," *Photonics*, vol. 8, no. 12, p. 577, 2021.
- [8] A. Vyatskikh, R. Ng, B. Edwards, R. Briggs, and J. Greer, "Additive manufacturing of high-refractive-index, nanoarchitected titanium dioxide for 3d dielectric photonic crystals," *Nano Lett.*, vol. 20, no. 5, p. 3513–3520, 2020.
- [9] Z. Chen, Z. Li, J. Li, C. Liu, C. Lao, Y. Fu, C. Liu, Y. Li, P. Wang, and Y. He, "3D printing of ceramics: A review," *J. Eur. Ceram. Soc.*, vol. 39, no. 4, pp. 661 – 687, 2019.
- [10] J. Pose-Rodriguez, J. Ceulemans, Y. Ménière, A. Nichogiannopoulou, and I. Rudyk, "Patents and additive manufacturing: Trends in 3d printing

- technologies," 07 2020.
- [11] A. Vyatskikh, S. Delalande, A. Kudo, X. Zhang, C. Portela, and J. Greer, "Additive manufacturing of 3d nano-architected metals," *Nature Communications*, vol. 9, 02 2018.
- [12] L. Jonušauskas, D. Gailevičius, S. Rekštytė, T. Baldacchini, S. Juodkazis, and M. Malinauskas, "Mesoscale laser 3D printing," *Opt. Express*, vol. 27, no. 11, pp. 15205–15221, 2019.
- [13] S. Maruo, O. Nakamura, and S. Kawata, "Three-dimensional microfabrication with two-photon-absorbed photopolymerization," *Opt. Lett.*, vol. 22, pp. 132–134, 1997.
- [14] K. Sugioka, "Hybrid femtosecond laser three-dimensional micro- and nanoprocessing: a review," *Int. J. Extrem. Manuf.*, vol. 1, p. 012003, 2019.
- [15] E. Skliutas, M. Lebedevaite, E. Kabouraki, T. Baldacchini, J. Ostrauskaite, M. Vamvakaki, M. Farsari, S. Juodkazis, and M. Malinauskas, "Polymerization mechanisms initiated by spatio-temporally confined light," *Nanophotonics*, vol. 10, no. 4, pp. 1211–1242, 2021.
- [16] T. Baldacchini, *Three-dimensional microfabrication using two photon polymerization: fundamentals, technology, and applications*. Elsevier, 2015.
- [17] L. Yang, F. Mayer, U. H. F. Bunz, E. Blasco, and M. Wegener, "Multi-material multi-photon 3D laser micro- and nanoprinting," *Light Adv. Manuf.*, vol. 2, p. 2021020003, 2021.
- [18] J. B. Mueller, J. Fischer, and M. Wegener, *Chapter 3 - Reaction Mechanisms and In Situ Process Diagnostics*. Oxford: William Andrew Publishing, 2016.
- [19] P. Kiefer, V. Hahn, M. Nardi, L. Yang, E. Blasco, C. Barner-Kowollik, and M. Wegener, "Sensitive photoresists for rapid multiphoton 3D laser micro- and nanoprinting," *Adv. Opt. Mater.*, vol. 8, p. 2000895, 2020.
- [20] M. Malinauskas, A. Žukauskas, G. Bičkauskaitė, R. Gadonas, and S. Juodkazis, "Mechanisms of three-dimensional structuring of photo-polymers by tightly focussed femtosecond laser pulses," *Opt. Express*, vol. 18, no. 10, pp. 10209–10221, 2010.
- [21] V. Hahn, T. Messer, N. M. Bojanowski, E. R. Curticean, I. Wacker, R. R. Schroder, E. Blasco, and M. Wegener, "Two-step absorption instead of two-photon absorption in 3D nanoprinting," *Nat. Photon.*, vol. 15, p. 932–938, 2021.
- [22] C.-H. Lin, G.-B. Lee, B.-W. Chang, and G.-L. Chang, "A new fabrication process for ultra-thick microfluidic microstructures utilizing SU-8 photoresist," *J. Micromech. Microeng.*, vol. 12, pp. 590–597, jun 2002.
- [23] D. T. Pham, S. S. Dimov, and R. S. Gault, "Part orientation in stereolithography," *Int. J. Adv. Manuf. Technol.*, vol. 15, pp. 674–682, aug 1999.
- [24] V. Hahn, P. Kiefer, T. Frenzel, J. Qu, E. Blasco, C. Barner-Kowollik, and M. Wegener, "Rapid assembly of small materials building blocks (voxels) into large functional 3D metamaterials," *Adv. Func. Mater.*, vol. 30,

- p. 1907795, 2020.
- [25] T. B. N. . E. R. C. . W. I. . S. R. . B. E. . W. M. Hahn, Vincent Messer, "Two-step absorption instead of two-photon absorption in 3d nanoprinting," vol. 15, pp. 932–938, 2021.
- [26] L. Jonušauskas, D. Gailevičius, L. Mikoliūnaitė, D. Sakalauskas, S. Šakirzhanovas, S. Juodkazis, and M. Malinauskas, "Optically clear and resilient free-form μ -optics 3D-printed via ultrafast laser lithography," *Materials*, vol. 10, no. 1, p. 12, 2017.
- [27] L. Jonušauskas, D. Mackevičiūtė, G. Kontenis, and V. Purlys, "Femtosecond lasers: the ultimate tool for high-precision 3D manufacturing," *Adv. Opt. Technol.*, vol. 8, pp. 241–251, may 2019.
- [28] M. Malinauskas, P. Danilevičius, and S. Juodkazis, "Three-dimensional micro-/nano-structuring via direct write polymerization with picosecond laser pulses," *Opt. Express*, vol. 19, pp. 5602–5610, mar 2011.
- [29] E. Stankevičius, E. Daugnoraitė, A. Selskis, S. Juodkazis, and G. Račiukaitis, "Photo-polymerization differences by using nanosecond and picosecond laser pulses," *Opt. Express*, vol. 25, no. 5, pp. 4819–4830, 2017.
- [30] M. Thiel, J. Fischer, G. Freymann, and M. Wegener, "Direct laser writing of three-dimensional submicron structures using a continuous-wave laser at 532 nm," *Appl. Phys. Lett.*, vol. 97, p. 221102, nov 2010.
- [31] D. Wu, S.-Z. Wu, J. Xu, L.-G. Niu, K. Midorikawa, and K. Sugioka, "Hybrid femtosecond laser microfabrication to achieve true 3D glass/polymer composite biochips with multiscale features and high performance: the concept of ship-in-a-bottle biochip," *Laser Photonics Rev.*, vol. 8, no. 3, pp. 458–467, 2014.
- [32] L. Jonušauskas, S. Rekštytė, R. Buividas, S. Butkus, R. Gadonas, S. Juodkazis, and M. Malinauskas, "Hybrid subtractive-additive-welding microfabrication for lab-on-chip (LOC) applications via single amplified femtosecond laser source," *Opt. Eng.*, vol. 56, no. 9, p. 094108, 2017.
- [33] T. Tičkūnas, M. Perrenoud, S. Butkus, R. Gadonas, S. Rekštytė, M. Malinauskas, D. Paipulas, Y. Bellouard, and V. Sirutkaitis, "Combination of additive and subtractive laser 3D microprocessing in hybrid glass/polymer microsystems for chemical sensing applications," *Opt. Express*, vol. 25, no. 21, pp. 26280–26288, 2017.
- [34] F. He, H. Xu, Y. Cheng, J. Ni, H. Xiong, Z. Xu, K. Sugioka, and K. Midorikawa, "Fabrication of microfluidic channels with a circular cross section using spatiotemporally focused femtosecond laser pulses," *Opt. Lett.*, vol. 35, no. 7, pp. 1106–1108, 2010.
- [35] Y. Tan, W. Chu, P. Wang, W. Li, J. Qi, J. Xu, Z. Wang, and Y. Cheng, "High-throughput multi-resolution three dimensional laser printing," *Phys. Scr.*, vol. 94, no. 1, p. 015501, 2018.
- [36] J. Hering, E. H. Waller, and G. Von Freymann, "Automated aberration

- correction of arbitrary laser modes in high numerical aperture systems," *Opt. Express*, vol. 24, no. 25, pp. 28500–28508, 2016.
- [37] L. Jonušauskas, S. Juodkazis, and M. Malinauskas, "Optical 3D printing: bridging the gaps in the mesoscale," *J. Opt.*, vol. 20, no. 5, p. 053001, 2018.
- [38] M. Straub and M. Gu, "Near-infrared photonic crystals with higher-order bandgaps generated by two-photon photopolymerization," *Opt. Lett.*, vol. 27, pp. 1824–1826, oct 2002.
- [39] K. Obata, A. El-Tamer, L. Koch, U. Hinze, and B. N. Chichkov, "High-aspect 3D two-photon polymerization structuring with widened objective working range (WOW-2PP)," *Light Sci. Appl.*, vol. 2, p. e116, dec 2013.
- [40] J. S. Oakdale, R. F. Smith, J.-B. Forien, W. L. Smith, S. J. Ali, L. B. Bayu Aji, T. M. Willey, J. Ye, A. W. van Buuren, M. A. Worthington, S. T. Prsbrey, H. S. Park, P. A. Amendt, T. F. Baumann, and J. Biener, "Direct laser writing of low-density interdigitated foams for plasma drive shaping," *Adv. Funct. Mater.*, vol. 27, no. 43, p. 1702425, 2017.
- [41] J. Li, P. Fejes, D. Lorensen, B. C. Quirk, P. B. Noble, R. W. Kirk, A. Orth, F. M. Wood, B. C. Gibson, D. D. Sampson, and R. A. McLaughlin, "Two-photon polymerisation 3D printed freeform micro-optics for optical coherence tomography fibre probes," *Sci. Rep.*, vol. 8, p. 14789, oct 2018.
- [42] H. Ni, G. Yuan, L. Sun, N. Chang, D. Zhang, R. Chen, L. Jiang, H. Chen, Z. Gu, and X. Zhao, "Large-scale high-numerical-aperture super-oscillatory lens fabricated by direct laser writing lithography," *RSC Advances*, vol. 8, no. 36, pp. 20117–20123, 2018.
- [43] S. Dehaeck, B. Scheid, and P. Lambert, "Adaptive stitching for meso-scale printing with two-photon lithography," *Additive Manufacturing*, vol. 21, pp. 589–597, may 2018.
- [44] P. Danilevičius, S. Rekštytė, E. Balčiūnas, A. Karaniauskas, R. Širmenis, D. Baltriukienė, M. Malinauskas, V. Bukelskienė, R. Gadonas, V. Sirvydis, and A. Piskarskas, "Direct laser fabrication of polymeric implants for cardiovascular surgery," *Mater. Sci.*, vol. 18, no. 2, pp. 145–149, 2012.
- [45] J. Torgersen, A. Ovsianikov, V. Mironov, N. Pucher, X. Qin, Z. Li, K. Cicha, T. Machacek, R. Liska, V. Jantsch, and J. Stampfl, "Photo-sensitive hydrogels for three-dimensional laser microfabrication in the presence of whole organisms," *J. Biomed. Opt.*, vol. 17, p. 105008, oct 2012.
- [46] D. Ricci, M. Nava, T. Zandrini, G. Cerullo, M. Raimondi, and R. Osellame, "Scaling-up techniques for the nanofabrication of cell culture substrates via two-photon polymerization for industrial-scale expansion of stem cells," *Materials*, vol. 10, p. 66, jan 2017.
- [47] E. Yulianto, S. Chatterjee, V. Purlys, and V. Mizeikis, "Imaging of latent three-dimensional exposure patterns created by direct laser writing in photoresists," *Appl. Surf. Sci.*, vol. 479, pp. 822–827, jun 2019.

- [48] M. Manousidaki, D. G. Papazoglou, M. Farsari, and S. Tzortzakis, "Abruptly autofocusing beams enable advanced multiscale photopolymerization," *Optica*, vol. 3, pp. 525–530, may 2016.
- [49] Y. Y. Schechner, N. Kiryati, and J. Shamir, "Separation of transparent layers by polarization analysis," *Surfaces*, vol. 8, p. 18, 1999.
- [50] M. Lago, A. Rodriguez, R. Sendón, J. Bustos, M. Nieto, and P. Paseiro, "Photoinitiators: a food safety review," *Food additives contaminants. Part A, Chemistry, analysis, control, exposure risk assessment*, vol. 32, 2015.
- [51] T. Bérces, *Chapter 3. The Decomposition of Aldehydes and Ketones*, vol. 5 of *Comprehensive Chemical Kinetics*. Elsevier, 1972.
- [52] E. Andrzejewska, *Three-Dimensional Microfabrication Using Two-photon Polymerization*. Micro and Nano Technologies, Oxford: William Andrew Publishing, 2016.
- [53] S. Maruo, O. Nakamura, and S. Kawata, "Three-dimensional microfabrication with two-photon-absorbed photopolymerization," *Opt. Lett.*, vol. 22, no. 2, pp. 132–134, 1997.
- [54] C. A. Coenjarts and C. K. Ober, "Two-photon three-dimensional microfabrication of poly(dimethylsiloxane) elastomers," *Chem. Mater.*, vol. 16, pp. 5556–5558, dec 2004.
- [55] S. M. Kuebler, K. L. Braun, W. Zhou, J. K. Cammack, T. Y., C. K. Ober, S. R. Marder, and J. W. Perry, "Design and application of high-sensitivity two-photon initiators for three-dimensional microfabrication," *J. Photochem. Photobiol.*, vol. 158, pp. 163–170, jun 2003.
- [56] B. D. Zhao, G. L. Li, Y. Z. Shi, H. Q. Zhang, and T. Wang, "Synthesis and optical properties of novel d- π -a- π -d type cationic cyclopentadienyliron complexes of arenes," *RSC Adv.*, vol. 5, pp. 54749–54756, 2015.
- [57] Z. Li, J. Torgersen, A. Ajami, S. Muhleder, X.-H. Qin, W. Husinsky, W. Holthöner, A. Ovsianikov, J. Stampfl, and R. Liska, "Initiation efficiency and cytotoxicity of novel water-soluble two-photon photoinitiators for direct 3d microfabrication of hydrogels," *RSC Advances*, 09 2013.
- [58] N. Pucher, A. Rosspeintner, V. Satzinger, V. Schmidt, G. Gescheidt, J. Stampfl, and R. Liska, "Structureactivity relationship in d- π -a- π -d-based photoinitiators for the two-photon-induced photopolymerization process," *Macromolecules*, vol. 42, pp. 6519–6528, 09 2009.
- [59] M. Albota, D. Beljonne, J.-L. Brédas, J. E. Ehrlich, J.-Y. Fu, A. A. Heikal, S. E. Hess, T. Kogej, M. D. Levin, S. R. Marder, D. McCord-Maughon, J. W. Perry, H. Röckel, M. Rumi, G. Subramaniam, W. W. Webb, X.-L. Wu, and C. Xu, "Design of organic molecules with large two-photon absorption cross sections," *Science*, vol. 281, no. 5383, pp. 1653–1656, 1998.
- [60] L. Markus, D. Ossipov, J. Hilborn, G. Peter, H. Katja, M. Markovic, S. Jrgen, R. Liska, and A. Ovsianikov, "Two-photon degradation of a hyaluronic acid based hydrogel using a two-photon initiator as photosensitizer,"

- Frontiers in Bioengineering and Biotechnology*, vol. 4, 01 2016.
- [61] M. Malinauskas, A. Žukauskas, G. Bičkauskaitė, R. Gadonas, and S. Juodkazis, "Mechanisms of three-dimensional structuring of photopolymers by tightly focussed femtosecond laser pulses," *Opt. Express*, vol. 18, no. 10, pp. 10209–10221, 2010.
- [62] K. Parkatzidis, E. Kabouraki, A. Selimis, M. Kaliva, A. Ranella, M. Farsari, and M. Vamvakaki, "Initiator-free, multiphoton polymerization of gelatin methacrylamide," *Macromol. Mater. Eng.*, vol. 303, p. 1800458, oct 2018.
- [63] R. Buividas, S. Rekštytė, M. Malinauskas, and S. Juodkazis, "Nanogroove and 3D fabrication by controlled avalanche using femtosecond laser pulses," *Opt. Mater. Express*, vol. 3, no. 10, pp. 1674–1686, 2013.
- [64] C. N. LaFratta and T. Baldacchini, "Two-photon polymerization metrology: Characterization methods of mechanisms and microstructures," *Micromachines*, vol. 8, no. 4, 2017.
- [65] V. R. Sastri, "Plastics in medical devices.: Chapter 7 : Engineering thermoplastics: Acrylics, polycarbonates, polyurethanes, polyacetals, polyesters, and polyamides," pp. 121 – 173, 2010.
- [66] S. Sarkar, K. B. Visscher, D. K. Hood, and C. J. Wasserman, *Patent US2016282737*. National Center for Biotechnology Information. PubChem Database, 2014.
- [67] U. Ali, K. J. Abd Karim, and N. Buang, "A review of the properties and applications of poly (methyl methacrylate) (pmma)," *Polymer Reviews*, vol. 55, pp. 1–28, 06 2015.
- [68] M. Rahmah, N. Razali, A. Ehsan, and S. Shaari, "Characterisation and process optimisation of photosensitive acrylates for photonics applications," *Science and Technology of Advanced Materials*, vol. 6, pp. 375–382, 04 2005.
- [69] T. Baldacchini, C. N. LaFratta, R. A. Farrer, M. C. Teich, B. E. A. Saleh, M. J. Naughton, and J. T. Fourkas, "Acrylic-based resin with favorable properties for three-dimensional two-photon polymerization," *Journal of Applied Physics*, vol. 95, no. 11, pp. 6072–6076, 2004.
- [70] M. Farsari, G. Filippidis, K. Sambani, T. S. Drakakis, and C. Fotakis, "Two-photon polymerization of an eosin Y-sensitized acrylate composite," *J. Photochem. Photobiol.*, vol. 181, pp. 132–135, jul 2006.
- [71] R. J. Winfield and S. O'Brien, "Two-photon polymerization of an epoxy-acrylate resin material system," *Appl. Surf. Sci.*, vol. 257, pp. 5389–5392, apr 2011.
- [72] T. Zandrini, N. Liaros, L. J. Jiang, Y. F. Lu, J. T. Fourkas, R. Osellame, and T. Baldacchini, "Effect of the resin viscosity on the writing properties of two-photon polymerization," *Opt. Mater. Express*, vol. 9, pp. 2601–2616, may 2019.
- [73] M. F. Akhtar, M. Hanif, and N. M. Ranjha, "Methods of synthesis of

- hydrogels . . . a review," *Saudi Pharmaceutical Journal*, vol. 24, no. 5, pp. 554 – 559, 2016.
- [74] E. M. Ahmed, "Hydrogel: Preparation, characterization, and applications: A review," *Journal of Advanced Research*, vol. 6, no. 2, pp. 105 – 121, 2015.
- [75] J. Torgersen, X.-H. Qin, Z. Li, A. Ovsianikov, R. Liska, and J. Stampfl, "Hydrogels for two-photon polymerization: A toolbox for mimicking the extracellular matrix," *Advanced Functional Materials*, vol. 23, no. 36, pp. 4542–4554, 2013.
- [76] A. Ovsianikov, M. Malinauskas, S. Schlie, B. N. Chichkov, S. Gittard, J. Narayan, M. Löbler, K. Sternberg, K.-P. Schmitz, and A. Haverich, "Three-dimensional laser micro- and nano-structuring of acrylated poly(ethylene glycol) materials and evaluation of their cytotoxicity for tissue engineering applications," *Acta biomaterialia*, vol. 7, pp. 967–74, 10 2010.
- [77] L. D. V. Lith, "Functionalization of poly-(ethylene glycol)- diacrylate (pegda) with different molecular mass using two-photon-polymerisation," 2016.
- [78] A. Ovsianikov, M. Gruene, M. Pflaum, L. Koch, F. Maiorana, M. Wilhelmi, A. Haverich, and B. Chichkov, "Laser printing of cells into 3D scaffolds," *Biofabrication*, vol. 2, p. 014104, 2010.
- [79] O. Kufelt, A. El-Tamer, C. Sehring, M. Meissner, S. Schlie-Wolter, and B. N. Chichkov, "Water-soluble photopolymerizable chitosan hydrogels for biofabrication via two-photon polymerization," *Acta Biomater.*, vol. 18, pp. 186–195, may 2015.
- [80] J.-F. Xing, M.-L. Zheng, and X.-M. Duan, "Two-photon polymerization microfabrication of hydrogels: an advanced 3D printing technology for tissue engineering and drug delivery," *Chem. Soc. Rev.*, vol. 44, no. 15, pp. 5031–5039, 2015.
- [81] H. Wang, W. Zhang, D. Ladika, H. Yu, D. Gailevičius, H. Wang, C.-F. Pan, P. N. S. Nair, Y. Ke, T. Mori, J. Y. E. Chan, Q. Ruan, M. Farsari, M. Malinauskas, S. Juodkakis, M. Gu, and J. K. W. Yang, "Two-photon polymerization lithography for optics and photonics: Fundamentals, materials, technologies, and applications," *Advanced Functional Materials*, vol. n/a, no. n/a, p. 2214211.
- [82] A. Campo and C. Greiner, "SU-8: a photoresist for high-aspect-ratio and 3D submicron lithography," *J. Micromech. Microeng.*, vol. 17, no. 6, pp. R81–R95, 2007.
- [83] B. Bilenberg, S. Jacobsen, M. S. Schmidt, L. H. D. Skjolding, P. Shi, P. Bøggild, J. O. Tegenfeldt, and A. Kristensen, "High resolution 100 kV electron beam lithography in SU-8," *Microelectron. Eng.*, vol. 83, no. 4-9, pp. 1609–1612, 2006.

- [84] K. K. Seet, S. Juodkazis, V. Jarutis, and H. Misawa, "Feature-size reduction of photopolymerized structures by femtosecond optical curing of SU-8," *Appl. Phys. Lett.*, vol. 89, no. 2, p. 024106, 2006.
- [85] Z.-J. Chen, J. Yao, Q.-J. Xu, and Z.-H. Wang, "Two-photon polymerization fabrication and raman spectroscopy research of SU-8 photoresist using the femtosecond laser," *Optoelectron. Lett.*, vol. 13, no. 3, pp. 210–213, 2017.
- [86] W. H. Teh, U. Dürig, G. Salis, R. Harbers, U. Drechsler, R. F. Mahrt, C. G. Smith, and H.-J. Güntherodt, "SU-8 for real three-dimensional subdiffraction-limit two-photon microfabrication," *Appl. Phys. Lett.*, vol. 84, no. 20, pp. 4095–4097, 2004.
- [87] Y. Liu, D. D. Nolte, and L. J. Pyrak-Nolte, "Large-format fabrication by two-photon polymerization in SU-8," *Appl. Phys. A*, vol. 100, no. 1, pp. 181–191, 2010.
- [88] H. E. Williams, D. J. Freppon, S. M. Kuebler, R. C. Rumpf, and M. A. Melino, "Fabrication of three-dimensional micro-photonic structures on the tip of optical fibers using SU-8," *Opt. Express*, vol. 19, no. 23, pp. 22910–22922, 2011.
- [89] J. Serbin, A. Ovsianikov, and B. Chichkov, "Fabrication of woodpile structures by two-photon polymerization and investigation of their optical properties," *Opt. Express*, vol. 12, no. 21, pp. 5221–5228, 2004.
- [90] E. Balčiūnas, S. J. Baldock, N. Dreižė, M. Grubliauskaitė, S. Coultas, D. L. Rochester, M. Valius, J. G. Hardy, and D. Baltriukienė, "3D printing hybrid organometallic polymer-based biomaterials via laser two-photon polymerization," *Polymer International*, vol. 68, no. 11, pp. 1928–1940, 2019.
- [91] G. Barroso, Q. Li, R. K. Bordia, and G. Motz, "Polymeric and ceramic silicon-based coatings – a review," *J. Mater. Chem. A*, vol. 7, pp. 1936–1963, 2019.
- [92] Z. Chen, Z. Li, J. Li, C. Liu, C. Lao, Y. Fu, C. Liu, Y. Li, P. Wang, and Y. He, "3D printing of ceramics: A review," *Journal of the European Ceramic Society*, vol. 39, no. 4, pp. 661–687, 2019.
- [93] P. A. Mathews, S. Koonisetty, S. Bhardwaj, P. Biswas, R. Johnson, and P. Gadhe, "Patent trends in additive manufacturing of ceramic materials," 2020.
- [94] M. Farsari, M. Vamvakaki, and B. Chichkov, "Multiphoton polymerization of hybrid materials," *J. Opt.*, vol. 12, p. 124001, 2010.
- [95] M. Malinauskas, M. Farsari, A. Piskarskas, and S. Juodkazis, "Ultrafast-laser micro/nano-structuring of photo-polymers: a decade of advances," *Phys. Rep.*, vol. 533, pp. 1–31, 2013).
- [96] G. J. Owens, R. K. Singh, F. Foroutan, M. Alqaysi, C. Han, C. Mahapatra, H. W. Kim, and J. C. Knowles, "Sol-gel based materials for biomedical

- applications," *Progress in Materials Science*, vol. 77, pp. 1–79, 2016.
- [97] J. Liu, Y. Liu, C. Deng, K. Yu, X. Fan, W. Zhang, Y. Tao, H. Hu, L. Deng, and W. Xiong, "3D printing nano-architected semiconductors based on versatile and customizable metal-bound composite photoresins," *Adv. Mat. Tech.*, p. 2101230, 2021.
- [98] J. Livage, "Sol-gel synthesis of hybrid materials," *Bulletin of Materials Science*, vol. 22, pp. 201–205, 1999.
- [99] M. Oubaha, "Introduction to hybrid sol-gel materials," *World Scientific Reference of Hybrid Materials*, pp. 1–36, 2019.
- [100] B. L. Rivas, B. F. Urbano, and J. Sánchez, "Water-soluble and insoluble polymers, nanoparticles, nanocomposites and hybrids with ability to remove hazardous inorganic pollutants in water," *Frontiers in Chemistry*, vol. 6, p. 320, 2018.
- [101] M. Shirai and H. Okamura, "Uv-curable positive photoresists for screen printing plate," *Polym. Int.*, vol. 65, pp. 362–370, 2016.
- [102] X. Zheng, C. Ji, O. Zeng, J. Liu, R. Liu, O. Mu, and X. Liu, "Synthesis of novel copolymer based on precipitation polymerization and its application in positive-tone photoresist," *J. Polym. Res.*, vol. 24, 2017.
- [103] N. Tsutsumi, A. Fukuda, R. Nakamura, K. Kinashi, and W. Sakai, "Fabrication of three-dimensional microstructures in positive photoresist through two-photon direct laser writing," *Appl. Phys. A*, vol. 123, no. 8, p. 553, 2017.
- [104] C. Hong-Zhong, Z. Mei-Ling, D. Xian-Zi, J. Feng, Z. Zhen-Sheng, and D. Xuan-Ming, "Two-photon nanolithography of positive photoresist thin film with ultrafast laser direct writing," *Appl. Phys. Lett.*, vol. 102, 2013.
- [105] O. Wei, F. Hu, and L. Wang, "Formation of nanotunnels inside a resist film in laser interference lithography," *Langmuir*, vol. 31, no. 19, pp. 5464–5468, 2015.
- [106] S. Z. Huang and K. Y. Wu, "Health risk assessment of photoresists used in an optoelectronic semiconductor factory," *Risk Analysis*, 2019.
- [107] W. Zhou, S. M. Kuebler, K. L. Braun, T. Yu, J. K. Cammack, C. K. Ober, J. W. Perry, and S. R. Marder, "An efficient two-photon-generated photoacid applied to positive-tone 3D microfabrication," *Science*, vol. 296, pp. 1106–1109, may 2002.
- [108] T. Yu, C. K. Ober, S. M. Kuebler, W. Zhou, S. R. Marder, and J. W. Perry, "Chemically amplified positive resists for two-photon three-dimensional microfabrication," *Adv. Mater.*, vol. 15, pp. 517–521, mar 2003.
- [109] S. Fafenrot, N. Grimmelsmann, M. Wortmann, and A. Ehrmann, "Three-dimensional (3D) printing of polymer-metal hybrid materials by fused deposition modeling," *Materials*, vol. 10, no. 10, 2017.
- [110] E. Balčiūnas, S. Baldock, N. Dreize, M. Grubliauskaitė, S. Coultas,

- D. Rochester, M. Valius, J. Hardy, and D. Baltriukiene, "3D printing hybrid organometallic polymer-based biomaterials via laser two-photon polymerisation," *Polymer International*, vol. 68, 08 2019.
- [111] D. Gailevičius, V. Padolskytė, L. Mikoliūnaitė, S. Šakirzanovas, S. Juodkazis, and M. Malinauskas, "Additive-manufacturing of 3D glass-ceramics down to nanoscale resolution," *Nanoscale Horizons*, vol. 4, pp. 647–651, 2019.
- [112] Q. Wen, Z. Yu, and R. Riedel, "The fate and role of in situ formed carbon in polymer-derived ceramics," *Progress in Materials Science*, vol. 109, p. 100623, 2020.
- [113] A. Ovsianikov, J. Viertl, B. Chichkov, M. Oubaha, B. Macraith, I. Sakellari, A. Giakoumaki, D. Gray, M. Vamvakaki, M. Farsari, and C. Fotakis, "Ultra-low shrinkage hybrid photosensitive material for two-photon polymerization microfabrication," *ACS nano*, vol. 2, pp. 2257–62, 2008.
- [114] P. Colombo, G. Mera, R. Riedel, and G. D. Sorarù, "Polymer-derived ceramics: 40 years of research and innovation in advanced ceramics," *Journal of the American Ceramic Society*, vol. 93, pp. 1805–1837, 2010.
- [115] P. Colombo, G. Mera, R. Riedel, and G. D. Sorarù, "Polymer-derived ceramics: 40 years of research and innovation in advanced ceramics," *Journal of the American Ceramic Society*, vol. 93, no. 7, pp. 1805–1837, 2010.
- [116] B. Cardenas-Benitez, C. Eschenbaum, D. Mager, J. Korvink, M. Madou, U. Lemmer, I. De Leon, and S. Martinez-Chapa, "Pyrolysis-induced shrinking of three-dimensional structures fabricated by two-photon polymerization: experiment and theoretical model," *Microsyst. Nanoeng.*, vol. 5, p. 38, 2019.
- [117] G. Konstantinou, E. Kakkava, L. Hagelucken, P. Sasikumar, J. Wanga, M. Makowska, G. Blugan, N. Nianias, F. Marone, H. Van Swygenhoven, J. Brugger, D. Psaltis, and C. Moser, "Additive micro-manufacturing of crack-free pdcs by two-photon polymerization of a single, low-shrinkage preceramic resin," *Add. Manuf.*, vol. 35, p. 101343, 2020.
- [118] N. Chai, Y. Liu, Y. Yue, P. Wei, X. Wang, J. Zhao, Q. Zhang, F. Huang, Z. Zeng, Z. Gan, L. Mai, and Y. Cheng, "Tin oxide ceramics 3d nonlinear photolithography via femtosecond laser," *Sci. Chi. Mater.*, vol. in press, no. 0, p. 00, 2020.
- [119] J. Bauer, C. Crook, A. Izard, Z. Eckel, N. Ruvalcaba, T. Schaedler, and L. Valdevit, "Additive manufacturing of ductile, ultrastrong polymer-derived nanoceramics," *Matter*, vol. 1, pp. 1–10, 2019.
- [120] D. W. Yee, M. A. Citrin, Z. W. Taylor, M. A. Saccone, V. L. Tovmasyan, and J. R. Greer, "Hydrogel-based additive manufacturing of lithium cobalt oxide," *Advanced Materials Technologies*, vol. 6, no. 2, p. 2000791, 2021.
- [121] M. Nogami, "Glass preparation of the ZrO_2 - SiO_2 system by the sol-gel process from metal alkoxides," *J. Non-Crystall. Sol.*, vol. 69, pp. 415–423,

1985.

- [122] A. Vyatskikh, R. C. Ng, B. Edwards, R. M. Briggs, and J. R. Greer, "Additive manufacturing of high-refractive-index, nanoarchitected titanium dioxide for 3D dielectric photonic crystals," *Nano Letters*, vol. 20, no. 5, pp. 3513–3520, 2020.
- [123] F. Kotz, P. Risch, K. Arnold, J. S. Sevim, Puigmartí-Luis, A. Quick, M. Thiel, A. Hrynevich, P. D. Dalton, D. Helmer, and B. E. Rapp, "Fabrication of arbitrary three-dimensional suspended hollow microstructures in transparent fused silica glass," *Nature Communications*, vol. 10, no. 1439, 2019.
- [124] Z. Vangelatos, H.-M. Sheikh, P.-S. Marcus, C.-P. Grigoropoulos, V.-Z. Lopez, G. Flamourakis, and M. Farsari, "Strength through defects: A novel bayesian approach for the optimization of architected materials," *Science Advances*, vol. 7, p. 2218, 2021.
- [125] J. Bauer, C. Crook, A. G. Izard, Z. C. Eckel, N. Ruvalcaba, T. A. Schaedler, and L. Valdevit, "Additive manufacturing of ductile, ultrastrong polymer-derived nanoceramics," *Matter*, vol. 1, no. 6, pp. 1547–1556, 2019.
- [126] L. Brigo, J. E. M. Schmidt, A. Gandin, N. Michieli, P. Colombo, and G. Brusatin, "3D nanofabrication of SiOC ceramic structures," *Advanced Science*, vol. 5, no. 12, p. 1800937, 2018.
- [127] L. Yao, W. Yang, S. Zhou, H. Mei, L. Cheng, and L. Zhang, "Design paradigm for strong-lightweight perfect microwave absorbers: The case of 3d printed gyroid shellular SiOC-based metamaterials," *Carbon*, vol. 196, pp. 961–971, 2022.
- [128] E. Shukrun, I. Cooperstein, and S. Magdassi, "3D-printed organic–ceramic complex hybrid structures with high silica content," *Advanced Science*, vol. 5, no. 8, p. 1800061, 2018.
- [129] M. Wang, C. Xie, R. He, G. Ding, K. Zhang, G. Wang, and D. Fang, "Polymer-derived silicon nitride ceramics by digital light processing based additive manufacturing," *Journal of the American Ceramic Society*, vol. 102, no. 9, pp. 5117–5126, 2019.
- [130] M. Vozárová, E. Neubauer, L. Bača, M. Kitzmantel, J. Feranc, V. Trembošová, P. Peciar, M. Kritikos, M. Orlovská, M. Janek, and M. Matejdes, "Preparation of fully dense boron carbide ceramics by fused filament fabrication (fff)," *Journal of the European Ceramic Society*, vol. 43, no. 5, pp. 1751–1761, 2023.
- [131] B. Sa, S. Lu, P. Gong, D. Wang, Y. Dong, J. Cheng, G. Ren, and M. Yan, "Printability and properties of tungsten cemented carbide produced using laser powder bed fusion additive manufacturing with Ti as a binder," *International Journal of Refractory Metals and Hard Materials*, vol. 111, 2023.
- [132] L. Cabezas, C. Berger, E. Jiménez-Piqué, J. Pötschke, and L. Llanes, "Testing length-scale considerations in mechanical characterization of WC-Co

- hardmetal produced via binder jetting 3d printing," *International Journal of Refractory Metals and Hard Materials*, vol. 111, p. 106099, 2023.
- [133] E. Hernández-Nava, C. Smith, F. Derguti, S. Tammam-Williams, F. Leonard, P. Withers, I. Todd, and R. Goodall, "The effect of defects on the mechanical response of ti-6al-4v cubic lattice structures fabricated by electron beam melting," *Acta Materialia*, vol. 108, pp. 279–292, 2016.
- [134] V. J. Challis, X. Xu, L. C. Zhang, A. P. Roberts, J. F. Grotowski, and T. B. Sercombe, "High specific strength and stiffness structures produced using selective laser melting," *Materials Design*, vol. 63, pp. 783–788, 2014.
- [135] C. Yan, L. Hao, A. Hussein, S. L. Bubb, P. Young, and D. Raymont, "Evaluation of light-weight AlSi10Mg periodic cellular lattice structures fabricated via direct metal laser sintering," *Journal of Materials Processing Technology*, vol. 214, no. 4, pp. 856–864, 2014.
- [136] S. Tsopanos, R. Mines, S. Mckown, Y. Shen, W. Cantwell, W. Brooks, and C. Sutcliffe, "The influence of processing parameters on the mechanical properties of selectively laser melted stainless steel microlattice structures," *Journal of Manufacturing Science and Engineering-transactions of The Asme - J MANUF SCI ENG*, vol. 132, 08 2010.
- [137] M. Sadeq Saleh, C. Hu, and R. Panat, "Three-dimensional microarchitected materials and devices using nanoparticle assembly by pointwise spatial printing," *Science Advances*, vol. 3, no. 3, p. e1601986, 2017.
- [138] M. Speirs, B. Van Hooreweder, V. Humbeeck, and J.-P. Kruth, "Fatigue behaviour of niti shape memory alloy scaffolds produced by slm, a unit cell design comparison," *Journal of the Mechanical Behavior of Biomedical Materials*, vol. 70, pp. 53–59, 2017.
- [139] X. W. Gu and J. R. Greer, "Ultra-strong architected cu meso-lattices," *Extreme Mechanics Letters*, vol. 2, pp. 7–14, 2015.
- [140] E. Blasco, J. Muller, P. Muller, V. Trouillet, M. Schon, T. Scherer, C. Barner-Kowollik, and M. Wegener, "Fabrication of conductive 3D gold-containing microstructures via direct laser writing," *Adv. Mater.*, vol. 28, pp. 3592–3595, 2016.
- [141] J. Fischer, G. von Freymann, and M. Wegener, "The materials challenge in diffraction-unlimited direct-laser-writing optical lithography," *Adv. Mater.*, vol. 22, pp. 3578–3582, 2010.
- [142] J. Fischer and M. Wegener, "Three-dimensional optical laser lithography beyond the diffraction limit," *Laser Photon. Rev.*, vol. 7, pp. 22–44, 2013.
- [143] R. Wollhofen, J. Katzmann, C. Hrelescu, J. Jacak, and T. A. Klar, "120 nm resolution and 55 nm structure size in sted-lithography," *Opt. Express*, vol. 21, pp. 10831–10840, 2013.
- [144] G. Seniutinas, A. Weber, C. Padeste, I. Sakellari, M. Farsari, and C. David, "Beyond 100 nm resolution in 3D laser lithography — post processing

- solutions," *Microelectron. Eng.*, vol. 191, pp. 25 – 31, 2018.
- [145] C. Ido, I. S. R. K. Chaitanya, B. Alisa, L. Uriel, and M. Shlomo, "3D printing of micrometer-sized transparent ceramics with on-demand optical-gain properties," *Adv. Mat.*, vol. 32, no. 28, p. 2001675, 2020.
- [146] Y. Cheng, C. Qun, P. Pumidech, L. Scott, G. Mallikarjunarao, L. Nickolay, and V. B. Jill, "3D-printed carbon electrodes for neurotransmitter detection," *Angewandte Chemie International Edition*, vol. 57, no. 43, pp. 14255–14259, 2018.
- [147] Y. D. W., L. M. L., E. B. W., and G. J. R., "Additive manufacturing of 3D-architected multifunctional metal oxides," *Advanced Materials*, vol. 31, no. 33, p. 1901345, 2019.
- [148] G. Konstantinou, E. Kakkava, L. Hagelüken, P. V. W. Sasikumar, J. Wang, M. G. Makowska, G. Blugan, N. Nianias, F. Marone, H. V. Swygenhoven, J. Brugger, D. Psaltis, and C. Moser, "Additive micro-manufacturing of crack-free PDCs by two-photon polymerization of a single, low-shrinkage preceramic resin," *Additive Manufacturing*, vol. 35, p. 101343, 2020.
- [149] A. Zakhurdaeva, P. I. Dietrich, H. Hölscher, C. Koos, J. G. Korvink, and S. Sharma, "Custom-designed glassy carbon tips for atomic force microscopy," *Micromachines*, vol. 8, no. 9, 2017.
- [150] S. Passinger, M. Saifullah, C. Reinhardt, S. K.R.V, B. Chichkov, and M. Welland, "Direct 3D patterning of TiO₂ using femtosecond laser pulses," *Ad. Mat.*, vol. 19, pp. 1218 – 1221, 2007.
- [151] R. K. Jayne, T. J. Stark, J. B. Reeves, D. J. Bishop, and A. E. White, "Dynamic actuation of soft 3D micromechanical structures using microelectromechanical systems (MEMS)," *Advanced Materials Technologies*, vol. 3, no. 3, p. 1700293, 2018.
- [152] Z. Vangelatos, L. Wang, and C. P. Grigoropoulos, "Laser pyrolysis for controlled morphing and chemical modification on 3D microlattices," *Journal of Micromechanics and Microengineering*, vol. 30, p. 055008, 2020.
- [153] B. Cardenas-Benitez, C. Eschebaum, D. Mager, J. Korvink, M. Madou, U. Lemmer, I. De Leon, and S. O. Martinez-Chapa, "Pyrolysis-induced shrinking of three-dimensional structures fabricated by two-photon polymerization: experiment and theoretical model," *Microsystems Nanoengineering*, vol. 5, 2019.
- [154] Y. Liu, H. Wang, J. Ho, R. Ng, R. Ng, V. Hall-Chen, E. Koay, Z. Dong, H. Liu, C. W. Qiu, J. Greer, and J. Yang, "Structural color three-dimensional printing by shrinking photonic crystals," *Nature Communications*, vol. 10, pp. 1–8, 2019.
- [155] T. Pham, D.-P. Kim, T.-W. Lim, S.-H. Park, D.-Y. Yang, and K.-S. Lee, "Three-dimensional SiCN ceramic microstructures via nanostereolithography of inorganic polymer photoresists," *Advanced Func-*

- tional Materials*, vol. 16, no. 9, pp. 1235–1241, 2006.
- [156] F. Kotz, A. S. Quick, P. Risch, T. Martin, T. Hoose, M. Thiel, D. Helmer, and B. E. Rapp, “Two-photon polymerization of nanocomposites for the fabrication of transparent fused silica glass microstructures,” *Adv. Mat.*, vol. 33, no. 9, p. 2006341, 2021.
- [157] X. Wen, B. Zhang, W. Wang, F. Ye, S. Yue, H. Guo, G. Gao, Y. Zhao, Q. Fang, C. Nguyen, X. Zhang, J. Bao, J. T. Robinson, P. M. Ajayan, and J. Lou, “3D-printed silica with nanoscale resolution,” *Nature Materials*, vol. 20, p. 1506–1511, 2021.
- [158] P. Boch and J.-C. Niepce, *Ceramic Materials: Processes, Properties and Applications*. 2010.
- [159] J. Binner, M. Porter, B. Baker, J. Zou, V. Venkatachalam, V. R. Diaz, A. D’Angio, P. Ramanujam, T. Zhang, and T. S. R. C. Murthy, “Selection, processing, properties and applications of ultra-high temperature ceramic matrix composites, UHTCMCs – a review,” *International Materials Reviews*, vol. 65, no. 7, pp. 389–444, 2020.
- [160] R. Bermejo, L. Llanes, P. Supancic, and T. Lube, “Thermal shock behaviour of an $\text{Al}_2\text{O}_3/\text{ZrO}_2$ multilayered ceramic with residual stresses due to phase transformations,” *Key Engineering Materials - KEY ENG MAT*, vol. 290, pp. 191–198, 2005.
- [161] W. Liu, Y. Xie, Z. Deng, Y. Peng, J. Dong, Z. Zhu, D. Ma, Z. Yi, G. Zhang, and X. Wang, “Preparation of Al_2TiO_5 ceramic fibers and thermal expansion, insulation, and strength of ZrO_2 - Al_2TiO_5 fiberboards,” 2021.
- [162] Z. B. M.S. Elmaghraby, A.I.M. Ismail, “Thermal expansion, physico-mechanical properties and microstructure of cordierite synthesized from different starting materials,” *Int. Ceram. Rev.*, vol. 64, p. 209–213, 2015.
- [163] E. Bajraktarova Valjakova, V. Korunoska-Stevkovska, B. Kapusevska, N. Gigovski, C. Bajraktarova Misevska, and A. Grozdanov, “Contemporary dental ceramic materials, a review: Chemical composition, physical and mechanical properties, indications for use,” *Open Access Macedonian Journal of Medical Sciences*, vol. 6, 2018.
- [164] E. Moustafa, “Hybridization effect of BN and Al_2O_3 nanoparticles on the physical, wear, and electrical properties of aluminum AA1060 nanocomposites,” *Applied Physics A*, vol. 127, 2021.
- [165] Q. Chen, B. Zou, Q. Lai, Y. Wang, R. Xue, H. Xing, X. Fu, C. Huang, and P. Yao, “A study on biosafety of HAP ceramic prepared by SLA-3D printing technology directly,” *Journal of the Mechanical Behavior of Biomedical Materials*, vol. 98, pp. 327–335, 2019.
- [166] H. M. Oh, Y. J. Park, H. N. Kim, J. W. Ko, and H. K. Lee, “Effect of milling ball size on the densification and optical properties of transparent Y_2O_3 ceramics,” *Ceramics International*, vol. 47, no. 4, pp. 4681–4687, 2021.
- [167] A. Solodar, R. Drevinskas, P. Kazansky, I. Abdulhalim, and

- A. Cerkauskaite, "Ultrafast laser induced nanostructured ITO for liquid crystal alignment and higher transparency electrodes," *Applied Physics Letters*, vol. 113, 2018.
- [168] T. D. Nguyen, L. P. Yeo, T. C. Kei, D. Mandler, S. Magdassi, and A. I. Y. Tok, "Efficient near infrared modulation with high visible transparency using SnO₂-WO₃ nanostructure for advanced smart windows," *Advanced Optical Materials*, vol. 7, no. 8, p. 1801389, 2019.
- [169] L. Wang, B. Lu, X. Liu, Y. Shi, J. Li, and Y. Liu, "Fabrication and upconversion luminescence of novel transparent Er₂O₃ ceramics," *Journal of the European Ceramic Society*, vol. 40, no. 4, pp. 1767-1772, 2020.
- [170] K. Hashimoto, H. Irie, and A. Fujishima, "TiO₂ photocatalysis: A historical overview and future prospects," vol. 44, no. 12, pp. 8269-8285, 2005.
- [171] H. Yin, A. Akey, and R. Jaramillo, "Large and persistent photoconductivity due to hole-hole correlation in CdS," *Phys. Rev. Materials*, vol. 2, p. 084602, 2018.
- [172] Y. Yao, D. Sang, L. Zou, Q. Wang, and C. Liu, "A review on the properties and applications of WO₃ nanostructurebased optical and electronic devices," *Nanomaterials*, vol. 11, no. 8, 2021.
- [173] S. Trolier-McKinstry, S. Zhang, A. J. Bell, and X. Tan, "High-performance piezoelectric crystals, ceramics, and films," *Annual Review of Materials Research*, vol. 48, no. 1, pp. 191-217, 2018.
- [174] B. Szafraniak, Fušnik, J. Xu, F. Gao, A. Brudnik, and A. Rydosz, "Semiconducting metal oxides: SrTiO₃, BaTiO₃ and BaSrTiO₃ in gas-sensing applications: A review," *Coatings*, vol. 11, no. 2, 2021.
- [175] D. Mendes, D. Sousa, A. C. Cerdeira, L. C. Pereira, A. Marques, J. Murta-Pina, A. Pronto, and I. Ferreira, "Low-cost and high-performance 3D printed YBCO superconductors," *Ceramics International*, vol. 47, no. 1, pp. 381-387, 2021.
- [176] Z. Chen, Z. Li, J. Li, C. Liu, C. Lao, Y. Fu, C. Liu, Y. Li, P. Wang, and Y. He, "3D printing of ceramics: A review," *Journal of the European Ceramic Society*, vol. 39, no. 4, pp. 661-687, 2019.
- [177] K. Watari, "High thermal conductivity non-oxide ceramics," *Journal of the Ceramic Society of Japan*, vol. 109, no. 1265, pp. S7-S16, 2001.
- [178] S. Thapliyal, *Manufacturing and characterization of a 3D-printable, antibacterial, magnesium oxide nanoparticles reinforced ABS filament*. PhD thesis, 04 2017.
- [179] B. Leukers, H. Gülkan, S. Irsen, S. Milz, C. Tille, H. Seitz, and M. Schieker, "Biocompatibility of ceramic scaffolds for bone replacement made by 3D printing," *Materialwissenschaft und Werkstofftechnik*, vol. 36, pp. 781 - 787, 12 2005.
- [180] X. Du, S. Fu, and Y. Zhu, "3D printing of ceramic-based scaffolds for

- bone tissue engineering: An overview," *Journal of Materials Chemistry B*, vol. 6, 06 2018.
- [181] K. Weber, D. Werdehausen, P. König, S. Thiele, M. Schmid, M. Decker, P. W. D. Oliveira, A. Herkommer, and H. Giessen, "Tailored nanocomposites for 3D printed micro-optics," *Opt. Mater. Express*, vol. 10, pp. 2345–2355, Oct 2020.
- [182] T. Shimazu, H. Maeda, E. H. Ishida, M. Miura, N. Isu, A. Ichikawa, and K. Ota, "High-damping and high-rigidity composites of Al_2TiO_5 – MgTi_2O_5 ceramics and acrylic resin," *Journal of Materials Science*, vol. 44, pp. 93–101, 2009.
- [183] J. Wang, "Extrusion-based 3D printing of macro/microstructures for advanced lithium/sodium batteries," 2019.
- [184] Z. Liu, J. Yu, P. Li, W. Xiaolong, Z. Yusong, X. Chu, X. Wang, H. Li, and Z. Wu, "Band alignments of $-\text{Ga}_2\text{O}_3$ with MgO , Al_2O_3 and MgAl_2O_4 measured by X-ray photoelectron spectroscopy," *Journal of Physics D Applied Physics*, vol. 52, p. 295104, 05 2019.
- [185] C. Han, R. Babicheva, J. D. Q. Chua, U. Ramamurty, S. B. Tor, C. N. Sun, and K. Zhou, "Microstructure and mechanical properties of $(\text{TiB}+\text{TiC})/\text{Ti}$ composites fabricated in situ via selective laser melting of Ti and B_4C powders," *Additive Manufacturing*, vol. 36, p. 101466, 2020.
- [186] K. A. Hamzah, C. K. Yeoh, M. M. Noor, P. L. Teh, Y. Y. Aw, S. A. Sazali, and W. M. A. W. Ibrahim, "Mechanical properties and thermal and electrical conductivity of 3D printed ABS-copper ferrite composites via 3D printing technique," *Journal of Thermoplastic Composite Materials*, vol. 35, no. 1, pp. 3–16, 2022.
- [187] R. Venkatkarthick and J. Qin, "A new 3D composite of V_2O_5 -based biodegradable ceramic material prepared by an environmentally friendly thermal method for supercapacitor applications," *Environmental Technology Innovation*, vol. 22, p. 101474, 2021.
- [188] C. Liu, X. Cheng, B. Li, Z. Chen, S. Mi, and C. Lao, "Fabrication and characterization of 3D-printed highly-porous 3D LiFePO_4 electrodes by low temperature direct writing process," *Materials*, vol. 8, p. 934, 2017.
- [189] M. Väättäjä, H. Kähäri, K. Ohenoja, M. Sobocinski, J. Juuti, and H. Jantunen, "3D printed dielectric ceramic without a sintering stage," *Scientific Reports*, vol. 8, 10 2018.
- [190] J. Kopfler, T. Frenzel, J. Schamljan, and M. Wegener, "Fused-silica 3D chiral metamaterials via helium-assisted microcasting supporting topologically protected twist edge resonances with high mechanical quality factors," *Adv. Mater.*, vol. 33, p. 2103205.
- [191] S. Rekstyte, E. Kaziulionyte, E. Balciunas, D. Kaskelyte, and M. Malinauskas, "Direct laser fabrication of composite material 3D microstructured scaffoldings," *J. Laser Micro. Nanoen.*, vol. 9, pp. 25–30, 2014.

- [192] S. Grauzeliene, A. Navaruckiene, E. Skliutas, M. Malinauskas, A. Serra, and J. Ostrauskaite, "Vegetable oil-based thiol-ene/thiol-epoxy resins for laser direct writing 3D micro-/nano-lithography," *Polymers*, vol. 13, p. 872, 2021.
- [193] E. Skliutas, M. Lebedevaite, S. Kasetaitė, S. Rekstyte, S. Lileikis, J. Ostrauskaite, and M. Malinauskas, "A bio-based resin for a multi-scale optical 3D printing," *Sci. Rep.*, vol. 10, p. 9758, 2020.
- [194] A. Ovsianikov, J. Viertl, B. Chichkov, M. Oubaha, B. MacCraith, I. Sakellari, A. Giakoumaki, D. Gray, M. Vamvakaki, M. Farsari, and C. Fotakis, "Ultra-low shrinkage hybrid photosensitive material for two-photon polymerization microfabrication," *ACS Nano*, vol. 2, no. 11, pp. 2257–2262, 2008.
- [195] L. Jonušauskas, T. Baravykas, D. Andriječ, T. Gadisauskas, and V. Purlys, "Stitchless support-free 3D printing of free-form micromechanical structures with feature size on-demand," *Scientific Reports*, vol. 9, 11 2019.
- [196] L. Jonušauskas, D. Andriječ, D. Andriukaitis, R. Vargalis, T. Baravykas, A. Stankevičius, G. Merkininkaitė, A. Pautienius, H. Gričius, E. Ežerskytė, E. Šimkutė, A. Butkutė, J. Grigas, and S. Šakirzanovas, "Expansion of direct laser writing DLW capabilities for usage in biomedical applications," *Proceedings of SPIE : SPIE Photonics West LASE conference 11677: Laser 3D Manufacturing VIII : Proceedings Presentation*, vol. 11677, 2021.
- [197] L. Jonušauskas, *3D laser lithography of meso-scale structures: towards applications*. PhD thesis, Vilnius university, 2021.
- [198] J. Liu and M. Ueda, "High refractive index polymers: fundamental research and practical applications," *J. Mater. Chem.*, vol. 19, pp. 8907–8919, 2009.
- [199] E. K. Macdonald and M. P. Shaver, "Intrinsic high refractive index polymers," *Polym. Intern.*, vol. 64, no. 1, pp. 6–14, 2015.
- [200] C. N. LaFratta and T. Baldacchini, "Two-photon polymerization metrology: Characterization methods of mechanisms and microstructures," *Micromachines*, vol. 8, no. 4, 2017.
- [201] Z. Shipeng, T. Sheng-nian, and F. Zhang, "Cristobalite formation from the thermal treatment of amorphous silica fume recovered from the metallurgical silicon industry," *Micro Nano Letters*, vol. 13, pp. 1465–1468, 2018.
- [202] J. Chevalier and L. Gremillard, "Zirconia ceramics. bioceramics an their clinical applications," pp. 243–265, 2008.
- [203] M. Malinauskas, P. Danilevičius, and S. Juodkazis, "Three-dimensional micro-/nano-structuring via direct write polymerization with picosecond laser pulses," *Opt. Express*, vol. 19, pp. 5602–5610, Mar 2011.
- [204] H. Zhou, Q. Li, T. Y. Lee, C. Guymon, E. S. Jönsson, and C. E. Hoyle, "Photopolymerization of acid containing monomers: real-time monitoring

- of polymerization rates," *Macromolecules*, vol. 39, no. 24, pp. 8269–8273, 2006.
- [205] I. Sakellari, E. Kabouraki, D. Gray, V. Purllys, C. Fotakis, A. Pikulin, N. Bityurin, M. Vamvakaki, and M. Farsari, "Diffusion-assisted high-resolution direct femtosecond laser writing," *ACS Nano*, vol. 6, pp. 2302–11, 02 2012.
- [206] L. Di and E. H. Kerns, "Chapter 7 - solubility," in *Drug-Like Properties (Second Edition)* (L. Di and E. H. Kerns, eds.), pp. 61–93, Boston: Academic Press, second edition ed., 2016.
- [207] M. Belmares, M. Blanco, W. A. Goddard III, R. B. Ross, G. Caldwell, S.-H. Chou, J. Pham, P. M. Olofson, and C. Thomas, "Hildebrand and Hansen solubility parameters from molecular dynamics with applications to electronic nose polymer sensors," *Journal of Computational Chemistry*, vol. 25, no. 15, pp. 1814–1826, 2004.
- [208] L. Liu, Z. Ma, Z. Yan, S. Zhu, and L. Gao, "The ZrO₂ formation in ZrB₂/SiC composite irradiated by laser," *Materials*, vol. 8, pp. 8745–8750, 12 2015.
- [209] R. A. Van Santen, "The Ostwald step rule," *J. Phys. Chem.*, vol. 88, no. 24, pp. 5768–5769, 1984.
- [210] T. Threlfall, "Structural and thermodynamic explanations of Ostwald's rule," *Org. Proc. Res. & Develop.*, vol. 7, no. 6, pp. 1017–1027, 2003.
- [211] A. Auxéméry, G. Philippot, M. R. Suchomel, D. Testemale, and C. Aymonier, "Stabilization of tetragonal zirconia nanocrystallites using an original supercritical-based synthesis route," *Chem. Mater.*, vol. 32, no. 19, pp. 8169–8181, 2020.
- [212] Y. Han, X. Huang, A. C. W. Rohrbach, and C. B. Roth, "Comparing refractive index and density changes with decreasing film thickness in thin supported films across different polymers," *The Journal of Chemical Physics*, vol. 153, no. 4, p. 044902, 2020.
- [213] T.-W. Koh, J. Spechler, K. M. Lee, C. Arnold, and B. Rand, "Enhanced outcoupling in organic light-emitting diodes via a high-index contrast scattering layer," *ACS Photonics*, vol. 2, pp. 1366–1372, 08 2015.
- [214] Y. Tang, C. Pina-Hernandez, Q. Niu, J. Nie, and S. Cabrini, "A novel high-refractive index episulfide-thiol polymer for nanoimprinting optical elements," *Journal of Materials Chemistry C*, vol. 6, no. 32, p. 8823 – 8831, 2018.
- [215] H.-Y. Ma, T.-L. Wang, P.-Y. Chang, and C.-H. Yang, "High refractive organic-inorganic hybrid films prepared by low water sol-gel and UV-irradiation processes," *Nanomaterials*, vol. 6, p. 44, 03 2016.
- [216] G. Calafiore, Q. Fillot, S. Dhuey, S. Sassolini, F. Salvadori, C. A. Mejia, K. Munechika, C. Peroz, S. Cabrini, and C. Piña-Hernandez, "Printable photonic crystals with high refractive index for applications in visible

- light," *Nanotechnology*, vol. 27, p. 115303, feb 2016.
- [217] E. Zanchetta, M. Cattaldo, G. Franchin, M. Schwentenwein, J. Homa, G. Brusatin, and P. Colombo, "Stereolithography of SiOC ceramic micro-components," *Advanced Materials*, vol. 28, no. 2, pp. 370–376, 2016.
- [218] S. Amoriello, A. Bianco, L. Eusebio, and P. Gronchi, "Evolution of two acid steps sol–gel phases by FTIR," *Journal of Sol-Gel Science and Technology*, vol. 58, no. 1, pp. 209–217, 2011.
- [219] B. Santhosh, M. Biesuz, A. Zambotti, and G. D. Sorarù, "Influence of gas-flow conditions on the evolution of thermally insulating Si_3N_4 nano-felts," *Materials*, vol. 15, no. 3, 2022.
- [220] M. Biesuz, E. Zera, M. Tomasi, P. Jana, O. Ersen, W. Baaziz, A. Lindemann, and G. D. Sorarù, "Polymer-derived Si_3N_4 nanofelts for flexible, high temperature, lightweight and easy-manufacturable super-thermal insulators," *Applied Materials Today*, vol. 20, p. 100648, 2020.
- [221] G. Zeng, X. Li, Y. Wei, T. Guo, X. Huang, X. Chen, and X.-Z. Tang, "Significantly toughened SiC foams with enhanced microwave absorption via in situ growth of Si_3N_4 nanowires," *Chemical Engineering Journal*, vol. 426, p. 131745, 2021.
- [222] E. Broitman, "Indentation hardness measurements at macro-, micro-, and nanoscale: A critical overview," *Tribology Letters*, vol. 65, p. 23, 12 2016.
- [223] M. D. Schmid, A. Toulouse, S. Thiele, S. Mangold, A. M. Herkommer, and H. Giessen, "3D direct laser writing of highly absorptive photoresist for miniature optical apertures," *Advanced Functional Materials*, p. 2211159.
- [224] G. Merkininkaite, E. Aleksandravicius, M. Malinauskas, D. Gailevicius, and S. Sakirzanovas, "Laser additive manufacturing of Si/ZrO₂ tunable crystalline phase 3D nanostructures," *Opto-Electronic Advances*, vol. 5, p. 210077, 2022.
- [225] O. Laguna, P. Lietor, F. I. Godino, and F. Corpas-Iglesias, "A review on additive manufacturing and materials for catalytic applications: Milestones, key concepts, advances and perspectives," *Materials Design*, vol. 208, p. 109927, 2021.
- [226] L. Jonusauskas and S. J. and. M. Malinauskas, "Optical 3d printing: bridging the gaps in the mesoscale," *J. Opt.*, vol. 20, no. 5, p. 053001, 2018.

APPENDIX

Volume of cubes before heating								
Sample	a ₁ (μm)	a ₂ (μm)	a ₃ (μm)	V ₁ (μm^3)	V ₂ (μm^3)	V ₃ (μm^3)	V _{avg.} (μm^3)	St. dv. (μm^3)
Si9:Zr1	23.60	23.82	22.33	13147	13517	11128	12598	1286
Si8:Zr2	25.45	24.83	24.95	16476	15303	15535	15771	621
Si7:Zr3	23.56	23.14	23.30	13078	12389	12649	12705	348
Si6:Zr4	21.03	21.98	23.54	9299	10616	13036	10984	1895
Si5:Zr5	23.38	23.37	23.27	12778	12770	12601	12717	100
Volume of cubes after heating								
Sample	a ₁ (μm)	a ₂ (μm)	a ₃ (μm)	V ₁ (μm^3)	V ₂ (μm^3)	V ₃ (μm^3)	V _{avg.} (μm^3)	St. dv. (μm^3)
Si9:Zr1	14.30	14.18	14.03	2921	2851	2763	2845	79
Si8:Zr2	15.93	15.72	15.57	4060	3885	3776	3907	143
Si7:Zr3	14.41	14.76	14.66	2992	3218	3147	3119	116
Si6:Zr4	14.58	14.07	15.88	3101	2785	4001	3296	631
Si5:Zr5	15.48	16.35	15.82	3707	4372	3956	4012	336
Volumetric shrinkage								
Sample	ΔV_1 (Shrink.) (%)		ΔV_2 (Shrink.) (%)		ΔV_3 (Shrink.) (%)		$\Delta V_{avg.}$ (%)	St. dv. (%)
Si9:Zr1	77.78		78.91		75.16		77.28	1.92
Si8:Zr2	75.36		74.6		75.69		75.69	0.56
Si7:Zr3	77.12		74.02		75.12		75.42	2.19
Si6:Zr4	66.66		73.76		69.31		75.57	3.58
Si5:Zr5	70.99		65.76		68.6		68.45	3.69

Table A.1: Volume of cubes and volumetric shrinkage after heat treatment at 1000 °C.

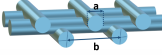
						
Si9:Zr1						
Velocity ($\mu\text{m/s}$)	Power (μW)	a_1 (nm)	a_2 (nm)	a_3 (nm)	$a_{avg.}$ (nm)	St. dv. (nm)
200	48	190	169	188	182	11.6
200	56	157	187	207	184	25.2
200	64	99	109	129	112	15.3
500	48	208	238	238	228	17.3
500	56	206	222	202	210	10.6
500	64	178	188	208	191	15.3
Si8:Zr2						
200	48	286	307	317	303	15.8
200	56	298	288	302	296	7.2
200	64	258	280	290	276	16.4
500	48	247	246	256	250	5.5
500	56	250	295	284	276	23.5
500	64	228	262	232	241	18.6
Si7:Zr3						
200	48	277	280	271	276	4.6
200	56	287	278	267	277	10.0
200	64	209	276	251	245	33.8
500	48	222	216	214	217	4.2
500	56	223	225	238	229	8.1
500	64	272	287	278	279	7.6
Si6:Zr4						
200	48	208	206	199	204	4.7
200	56	251	249	233	244	9.9
200	64	208	219	188	205	15.7
500	48	234	252	266	251	16.0
500	56	178	192	201	190	11.6
500	64	258	277	264	266	9.7
Si5:Zr5						
200	48	263	279	279	274	9.2
200	56	316	343	317	325	15.3
200	64	278	265	286	276	10.6
500	48	207	206	191	201	9.0
500	56	239	223	230	231	8.0
500	64	222	262	246	243	20.1

Table A.2: Width of woodpile lines before heating.

Si9:Zr1						
Velocity ($\mu\text{m/s}$)	Power (μW)	b_1 (nm)	b_2 (nm)	b_3 (nm)	$b_{avg.}$ (nm)	St. dv. (nm)
200	48	818	858	839	838	20.0
200	56	915	905	876	899	20.3
200	64	881	882	906	890	14.2
500	48	891	931	891	904	23.1
500	56	921	913	929	921	8.0
500	64	937	923	947	936	12.1
Si8:Zr2						
200	48	971	990	961	974	14.7
200	56	949	960	969	959	10.0
200	64	1011	961	991	988	25.2
500	48	980	901	970	950	43.0
500	56	1000	1040	1003	1014	22.3
500	64	956	975	956	962	11.0
Si7:Zr3						
200	48	961	951	980	964	14.7
200	56	951	921	970	947	24.7
200	64	941	936	941	939	2.9
500	48	953	959	982	965	15.3
500	56	921	948	961	943	20.4
500	64	870	871	817	853	30.9
Si6:Zr4						
200	48	822	852	832	835	15.3
200	56	847	858	821	842	19.0
200	64	862	852	832	849	15.3
500	48	840	867	841	849	15.3
500	56	892	891	861	881	17.6
500	64	856	886	857	866	17.0
Si5:Zr5						
200	48	951	931	961	948	15.3
200	56	881	861	891	878	15.3
200	64	881	905	897	894	12.2
500	48	913	900	926	913	13.0
500	56	883	873	847	868	18.6
500	64	872	842	832	849	20.8

Table A.3: Width of woodpiles periods before heating.

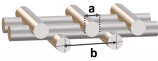
						
Si9:Zr1						
Velocity ($\mu\text{m/s}$)	Power (μW)	a_1 (nm)	a_2 (nm)	a_3 (nm)	$a_{avg.}$ (nm)	St. dv. (nm)
200	48	135	141	147	141	6.0
200	56	139	143	155	146	8.3
200	64	60	57	59	58.7	1.5
500	48	190	206	186	194	10.6
500	56	183	199	175	186	12.2
500	64	185	172	159	172	13.0
Si8:Zr2						
200	48	258	262	247	256	7.8
200	56	236	237	235	236	1.0
200	64	227	238	248	238	10.5
500	48	167	157	165	163	5.3
500	56	206	185	173	188	16.7
500	64	176	186	191	184	7.6
Si7:Zr3						
200	48	216	212	234	221	11.7
200	56	208	218	204	210	7.2
200	64	197	185	173	185	12.0
500	48	151	135	167	151	16.0
500	56	169	184	192	182	11.7
500	64	225	172	185	194	27.6
Si6:Zr4						
200	48	176	182	186	181	5.0
200	56	150	170	173	164	12.5
200	64	166	149	151	155	9.3
500	48	197	182	187	189	7.6
500	56	161	166	168	165	3.6
500	64	207	217	227	217	10.0
Si5:Zr5						
200	48	173	180	169	174	5.6
200	56	213	193	213	206	11.5
200	64	196	185	190	190	5.5
500	48	148	160	152	153	6.1
500	56	139	164	156	153	12.8
500	64	169	175	191	178	11.4

Table A.4: Width of woodpile lines after heating at 1000 °C under air atmosphere.

Si9:Zr1						
Velocity ($\mu\text{m/s}$)	Power (μW)	b_1 (nm)	b_2 (nm)	b_3 (nm)	$b_{avg.}$ (nm)	St. dv. (nm)
200	48	651	643	651	648	4.6
200	56	662	665	630	652	19.4
200	64	622	625	667	638	25.2
500	48	611	627	667	635	28.8
500	56	643	643	627	637.7	9.2
500	64	667	651	675	664	12.2
Si8:Zr2						
200	48	699	651	699	683	27.7
200	56	676	658	649	661	73.7
200	64	634	624	624	627	5.8
500	48	651	619	635	635	16.0
500	56	651	668	635	651	16.5
500	64	627	659	627	638	18.5
Si7:Zr3						
200	48	570	850	545	565	18.0
200	56	548	518	538	535	15.3
200	64	572	603	584	58	15.6
500	48	562	573	541	559	16.3
500	56	540	564	524	543	20.1
500	64	515	520	516	517	2.6
Si6:Zr4						
200	48	555	527	526	536	16.5
200	56	522	543	536	534	10.7
200	64	551	516	529	532	17.7
500	48	574	576	545	565	17.3
500	56	549	559	542	550	8.5
500	64	571	552	562	562	9.5
Si5:Zr5						
200	48	555	529	528	537	15.3
200	56	518	539	512	523	14.2
200	64	513	518	515	515	2.5
500	48	523	579	605	569	41.9
500	56	521	543	586	550	33.1
500	64	567	523	550	547	22.2

Table A.5: Width of woodpile periods after heating at 1000 °C under air atmosphere.

Wavelength, nm	SOLS			GELS			POLYMERS		
	9:1	8:2	7:3	9:1	8:2	7:3	9:1	8:2	7:3
	436.5	1.38056	1.38411	1.39028	1.44011	1.44392	1.45397	1.44281	1.45079
468	1.37782	1.38090	1.3872	1.43650	1.44017	1.44991	1.43936	1.44714	1.45183
513.5	1.37566	1.37859	1.38487	1.43396	1.43756	1.44719	1.43688	1.44457	1.44911
546.3	1.37430	1.37711	1.38316	1.43217	1.43572	1.44523	1.43515	1.44277	1.44714
589.3	1.37273	1.37477	1.38133	1.43025	1.43373	1.44313	1.43327	1.44081	1.44504
643.3	1.37116	1.37392	1.37938	1.42833	1.43175	1.44105	1.43139	1.43888	1.44296

Table A.6: Refractive indices of MTMS:MAPTMS + 1% PI sols, gels and polymers at 25 °C temperature at different wavelengths.

Temperature, °C	9:1			8:2			7:3		
	Hardness, GPa	St. dev., GPa	Hardness, GPa	St. dev., GPa	Hardness, GPa	St. dev., GPa	Hardness, GPa	St. dev., GPa	
	1000	12.2988	0.1670	13.1271	0.3496	10.8921	0.3341	13.1670	0.7897
1100	13.1869	0.8577	13.3532	0.9723	13.1670	0.7897	13.9930	0.7284	
1200	13.9453	0.7872	14.3282	1.1792	13.9930	0.7284	13.8882	0.8373	
1300	13.8625	0.8067	13.4257	0.7171	13.8882	0.8373	11.9859	0.9615	
1400	11.4543	3.8186	11.8883	1.0034	11.9859	0.9615	2.2566	1.2362	
1500	10.3297	1.9381	6.3965	4.2822	2.2566	1.2362			

Table A.7: Average hardness of prepared MTMS:MAPTMS (9:1, 8:2 and 7:3) glass and ceramic samples at various sintering temperatures.

Temperature, °C	9:1		8:2		7:3	
	Elastic m., GPa	St. dev., GPa	Elastic m., GPa	St. dev., GPa	Elastic m., GPa	St. dev., GPa
1000	88.4686	4.1506	88.3280	5.2960	55.8364	11.7997
1100	100.2660	2.7130	98.4380	2.0560	98.1904	2.7417
1200	104.5952	1.6143	104.9917	1.8061	102.7657	0.9586
1300	102.7715	1.1273	96.0586	1.7794	100.5296	1.4393
1400	97.7796	9.8725	94.1003	3.2555	89.6162	3.1480
1500	84.8109	4.2222	80.1691	19.5649	47.1418	11.5407

Table A.8: Average reduced elastic modulus (Young modulus) of prepared MTMS:MAPTMS (9:1, 8:2 and 7:3) glass and ceramic samples at various sintering temperatures.

Temperature, °C	9:1		8:2		7:3	
	Shrinkage, %	St. dev., %	Shrinkage, %	St. dev., %	Shrinkage, %	St. dev., %
1000	19.73	0.71	20.34	0.25	22.37	0.13
1100	21.70	0.37	22.24	0.52	23.88	0.63
1200	22.29	0.35	22.97	0.61	24.56	0.62
1300	22.36	0.49	23.30	0.49	25.04	0.63
1400	22.41	0.31	23.57	0.63	25.38	0.39
1500	22.62	1.13	23.67	0.35	25.50	0.90

Table A.9: Linear shrinkages of prepared MTMS:MAPTMS (9:1, 8:2 and 7:3) glass and ceramic samples at various sintering temperatures.

Temperature, °C	9:1		8:2		7:3	
	Density, g/cm ³	St. dev., g/cm ³	Density, g/cm ³	St. dev., g/cm ³	Density, g/cm ³	St. dev., g/cm ³
Polymers	1.3200	0.0035	1.3049	0.0065	1.3029	0.0035
1000	2.1490	0.1026	2.0465	0.0299	2.0112	0.0947
1100	2.1988	0.0397	2.1491	0.0549	2.0617	0.1177
1200	2.2348	0.0416	2.2064	0.0930	2.1402	0.1190
1300	2.2722	0.1669	2.2175	0.0636	2.1613	0.1415
1400	2.2905	0.0402	2.2521	0.0839	2.2142	0.1211
1500	2.3303	0.0267	2.2815	0.1209	2.2365	0.1152

Table A.10: Bulk densities of prepared MTMS:MAPTMS (9:1, 8:2 and 7:3) polymeric, glass and ceramic samples at various sintering temperatures.

Table A.11: Current achievements of 3D inorganic structure resolution in 3D lithography [B1].

Nr.	Ref. Year	Final material	Post processing	Laser parameters and setup	Feat. size, nm	Applications
1.	[224] 2022	SiO ₂ , ZrSiO ₄ , t-ZrO ₂ , m-ZrO ₂	Heating. Air, 1h at 1000 °C, heating rate 5 °C/min.	Direct laser writing, $\tau = 300$ fs, $\lambda = 515$ nm, $f = 200$ kHz, $P_{avg} = 64 \mu\text{W}$, 100x 1.4 NA objective, $v = 200 \mu\text{m/s}$, $h = 0.1 \mu\text{m}$ (in both, x and y axes).	60	3D ceramic nano-structures that are resistant to extreme low and high temperatures and aggressive chemicals.
2.	[97] 2021	Metal oxide semiconductors (e.g., ZnO and Co ₃ O ₄)	Heating. O ₂ , 550 °C for 30 min, heating rate 20 °C/s	Homemade TPP system. A Ti: sapphire fs laser, $\lambda = 780$ nm, $\tau = 100$ fs, $f = 80$ MHz, 40x 1.3 NA objective, $P_{avg} = 7 \sim 20$ mW, $v = 0.5 \sim 5$ mm/s.	170	Optoelectronic and semiconductor devices.
3.	[7] 2021	SiO ₂ , ZrO ₂	Heating. Air, raising the temperature for 12 h until reaching 1100 °C and maintaining it for 3 h.	$\lambda = 515$ nm of a Yb:KGW laser Pharos (Light Conversion Ltd.), $\tau = 300$ fs, $f = 200$ kHz, 63x 1.4 NA objective.	500	Micro-optics that are resistant to: high intensity radiation, temperature, acidic environment, pressure variations.

Nr.	Ref. Year	Final material	Post processing	Laser parameters and setup	Feat. size, nm	Applications
4.	[157] 2021	SiO ₂ doped with Er ³⁺ , Eu ³⁺ , Tm ³⁺ , Nd ³⁺ and Yb ³⁺	Heating. Nitrogen, 1300 °C for 240 min, heating rate 1 °C/s.	Commercial 2PP AM system Nanoscribe Photonic Professional GT, 63x 1.4 NA or 25x 0.8 NA objectives, $\lambda = 780$ nm, $\tau = 100$ fs, $P_{\text{avg}} = 15\text{--}20$ mW, $v = 4\text{--}5$ mm/s.	200	Optical applications: active photonics, non-Hermitian photonics and quantum devices.
5.	[156] 2021	Fused silica	Heating: samples sintered in vacuum at a pressure of 5×10^{-2} mbar, 2h at 1300 °C. The heating and cooling rate was 3 K/min.	Commercial lithography system Photonic Professional GT2 (Nanoscribe GmbH, Germany), 10×0.3 NA objective, $\lambda = 780$ nm, slicing 5 μm , $h = 1$ μm , $v = 100$ mm/s, and laser power 80%.	10000	High-resolution glass components: optics, photonics, functional and engineered surfaces, lab-on-a-chip, life sciences, and biomedical engineering.
6.	[152] 2020	Zr-DMAEMA	Laser extreme pyrolysis. Lighthouse Sprout-C 4 W, $\lambda = 532$ nm, $P_{\text{avg}} = 5\text{--}10$ mW.	FemtoFiber pro NIR laser, $\lambda = 780$ nm, $\tau = 100$ fs, $f = 80$ MHz, 100×1.4 NA objective.	250	Scaffolds for artificial tissue and 3D patterning of local hierarchical nanostructures for 3D complex biomimetic materials and structures.

Nr.	Ref. Year	Final material	Post processing	Laser parameters and setup	Feat. size, nm	Applications
7.	[148] 2020	SiOC	Heating. Argon, the temperature was increased to 200 °C with a hold time of 2h and 1000 °C for 1h, 5 °C/min.	Nanoscribe Professional GT. The laser source is an ultrafast Er:doped fiber laser system from Topica Photonics AG, $\lambda = 780$ nm, $\tau = 100$ fs, $f = 80$ MHz, 63×1.4 NA objective, $P_{avg} = 15$ mW, $v = 6$ μ m/s.	349	Ceramic-based micro-nozzle for micro-droplets delivery or micro-manipulation which can be realized and provide high robustness and chemical resistance.
8.	[122] 2020	Rutile TiO ₂	Heating. Air, 750-900 °C for 1h, 3 °C/min.	A commercially available two-photon lithography system- Photonic Professional GT, Nanoscribe GmbH. $P_{avg} = 12.5 - 20$ mW and $t_{ex} = 0.5 - 10$ ms.	150	Fabrication of components for micro-optics or 3D MEMS.
9.	[145] 2020	YAG, Nd:YAG	Heating. Air, 200 °C for 2h, 520 °C for 2h, 620 °C for 2h, 920-1500 °C 5h for polycrystalline, 0.6 °C/min.	Photonic Professional GT printer (Nanoscribe GmbH, Germany). 25x objective.	2000	Optical components in high-intensity laser systems, which require heat resistance, or light sources in optical circuits.

Nr.	Ref. Year	Final material	Post processing	Laser parameters and setup	Feat. size, nm	Applications
10.	[154] 2019	IP-Dip	Heating. Argon, 450 °C for 12, 17 or 21 min, 10 °C/min.	Photonic Professional GT, $\lambda = 780$ nm, 63x 1.4 NA objective, $P_{\text{avg}} = 16 - 27$ mW, $v = 15$ mm/s.	100	Integrated optical components, 3D photonic integrated circuitry, anti-counterfeiting security labels, dye-free structural color printing.
11.	[153] 2019	SU-8	Heating. Nitrogen, 300 °C 1h, 900 °C 1h, 5 °C/min.	Coherent Mira 900D, $\lambda = 800$ nm, $\tau = 150$ fs, $f = 76$ MHz, 100 x 1.4 NA objective.	300	Carbon nanowires: label-free impedance-based nanobiosensors, nanoparticle-based gas sensors, and electrochemical immunosensors.
12.	[123] 2019	IP-S template, Fused silica	Heating. Air, 600 °C, 0.5 °C/min thermal debinding, 1300 °C, 3 °C/min sintering.	Photonic Professional GT, 0.8 NA objective.	7000	Microfluidics, flow-through synthesis, photonics or waveguiding applications in optics, and photonics.

Nr.	Ref. Year	Final material	Post processing	Laser parameters and setup	Feat. size, nm	Applications
13.	[125] 2019	SiOC	Heating. Vacuum, 1000 °C for 1h. Heating at 1 °C/min. Cooling at 3 °C/min.	Photonic Professional GT, FemtoFiber pro NIR laser, $\lambda = 780$ nm, $\tau = 100$ fs, $f = 80$ MHz, 63×1.4 NA objective, $v = 10$ $\mu\text{m}/\text{s}$, $P_{\text{avg}} = 16 - 36$ mW for octet lattices (with 200 nm lines).	200	Engineering applications, ranging from automotive to aerospace and energy systems.
14.	[147] 2019	Metal oxide (ex. ZnO)	Heating. Air, 500 °C, Heating at 0.5 °C/min, Cooling at 2 °C/min.	Photonic Professional GT, 63×1.4 NA objective.	250	Nanoelectromechanical system (NEMS), desulfurization agent, UV photodetector.
15.	[111] 2018	Glass-ceramic, cristobalite SiO ₂ and tetragonal ZrO ₂ .	Heating. Air, 1000-1500 °C.	$\tau = 300$ fs, $\lambda = 515$ nm, $f = 200$ kHz objectives from 0.8 to 1.4 NA.	100	Chemically resilient and high temperature optical elements for sensors.

Nr.	Ref. Year	Final material	Post processing	Laser parameters and setup	Feat. size, nm	Applications
16.	[151] 2018	IP-Dip, PEG-DA, PETA	-	Nanoscribe Photonic Professional GT, $\lambda = 780 \text{ nm}$, $63 \times 1.4 \text{ NA}$ objective.	950	Microstructures for IR imaging or deformable microscaffolds for living cell studies.
17.	[144] 2018	IP-Dip, SZ2080	Heating. Nitrogen flow 100 sccm , $250 \text{ }^\circ\text{C}$ 1 h , $350 \text{ }^\circ\text{C}$ 1 h , $690 \text{ }^\circ\text{C}$ 1 h , Heating rate $5 \text{ }^\circ\text{C}/\text{min}$. Plasma etching.	Photonic Professional GT, Femtolasers Fusion, $\lambda = 800 \text{ nm}$, $f = 75 \text{ MHz}$, $\tau = 20 \text{ fs}$, $100 \times 1.4 \text{ NA}$ objective.	25	Micro-optical elements and 3D templates or micro-scaffolds for cell studies.
18.	[146] 2018	Glassy carbon	Pyrolysis by rapid thermal processing.	Nanoscribe direct-write laser lithography system.	1000	Carbon microelectrodes.

Nr.	Ref. Year	Final material	Post processing	Laser parameters and setup	Feat. size, nm	Applications
19.	[149] 2017	Glassy carbon	Heating. Vacuum, 900 °C.	Nanoscribe 2PP set-up, $P_{avg} = 30 - 33.6 \text{ mW}$, $v = 25 \text{ mm/s}$.	60	Carbon-microelectromechanical systems (Carbon-MEMS) and nanoelectromechanical systems (Carbon-NEMS).
20.	[150] 2007	Anatase, rutile TiO ₂	Heating. 450 °C anatase. 650 °C rutile.	Spectra Physics Tsunami, $\lambda = 780 \text{ nm}$, $\tau = 120 \text{ fs}$, $f = 80 \text{ MHz}$, 100x 1.35 NA objective.	400	3D inorganic photonic crystals.
21.	[155] 2006	SiCN	Heating. Nitrogen, 600 °C for 2h, temperature rate 2 °C/min.	Ti:sapphire laser, $\lambda = 780 \text{ nm}$, $\tau = 100 \text{ fs}$, $f = 80 \text{ MHz}$, 1.4 NA objective, $P_{avg} = 100 \text{ mW}$, $t_{ex} = 1 \text{ ms}$.	210	3D ceramic structures such as: tribological MEMS and chemical-resistant microfluidics.

SANTRAUKA

Įvadas

Pastaraisiais dešimtmečiais keraminės medžiagos ir iš jų pagamintos 3D struktūros susilaukia vis daugiau dėmesio dėl išskirtinių mechaninių, cheminių ir terminių savybių [1]. Didėjant susidomėjimui 3D keraminėmis mikro/nano struktūromis, didėja naujų medžiagų ir 3D darinių gamybos procesų paklausa. Iki šiol tiksliausia ir universaliausia adityvi neorganinių laisvos formos struktūrų formavimo technologija yra femtosekundinė lazerinė 3D fotopolimerizacija (spausdinimas) kombinuojama kartu su pirolize [2–4]. Femtosekundiniais lazeriais galima ypač tiksliai lokalizuoti ir kontroliuoti šviesos ir medžiagos sąveiką, pasiekiant minimalų šiluminį efektą bei labai aukštą fabrikavimo preciziškumą (iki šimtų nanometrų) [225, 226]. Atkaitinus tokias struktūras aukštoje temperatūroje jos tampa neorganinėmis ir susitraukia, todėl matmenys tampa dar mažesni.

Multifotoninė fotopolimerizacija yra puiki technologija gaminant įvairius mikromechaninius [5], medicininius [6], optinius [7] ir fotoninius darinius [8], tačiau iki šiol reikšmingas ir pramonėje pritaikomas struktūras realizuoti pavyksta tik naudojant organinius arba birių neorganinių dalelių ir skystų organinių rezistų suspensijas.

Vis dėlto grynai organiniai rezistai nėra pakankamai atsparūs agresyviems chemikalams, ekstremalioms temperatūroms ir aplinkos sąlygoms bei nepasižymi patraukliomis fizikinėmis ir mechaninėmis savybėmis. Iš neorganinių–organinių suspensijų pagamintos struktūros neprilygsta grynomis keraminėms ar kristalinėms medžiagoms, tačiau yra kur kas mechaniškai ir chemiškai atsparesnės už organines. Vis dėlto iš tokių suspensijų (neorganinių dalelių ir organinio monomero mišinio) pagamintų struktūrų formos ir raiškos preciziškumą apriboja dalelių dydis, jų sedimentacija laike ir šviesos sklaidos nuo dalelių paviršiaus efektas fotopolimerizacijos metu. Todėl disertacijoje pateikiu iki šiol buvusių keraminių 3D struktūrų formavimo problemų sprendimus.

Disertacija apima naujų fotoaktyvių vienalyčių pažangių metalorganinių junginių sintezes, medžiagų pritaikymą lazerinėje litografijoje ir gautų struktūrų terminį ir/ar cheminį apdirbimą. Pasitelkus šiuos metodus pavyko išspręsti

neorganinių struktūrų deformacijos, raiškos (pasiekta iki šiol didžiausia net iki 60 nm neorganinės 3D formos raiška) ir fazės grynumo iššūkius. Be to struktūros pasižymėjo itin dideliu kietumu (kietumas ≈ 15 GPa, tamprumo modulis ≈ 105 GPa), stabilumu agresyviuose chemikaluose ir atsparumu ekstremalioms temperatūroms (nuo -200 °C iki 1400 °C). Pasiiekti rezultatai suteikia konkurencingus pranašumus turimų spausdinimo medžiagų srityje ir atveria naujas galimybes sukurtas medžiagas ir iš jų pagamintas 3D keramines struktūras vystyti iki komercinių produktų.

Tikslas ir uždaviniai

Disertacijos tikslas buvo zolių-gelių metodu susintetinti įvairius metalo organinius junginius ir pagaminti keramines/kristalines 3D mikro/nanostruktūras kombinuojant fotopolimerizaciją femtosekundiniais lazeriais ir pirolizę. Šiam tikslui įgyvendinti buvo suformuluoti šie uždaviniai:

1. Zolių-gelių metodu susintetinti hibridinius silicio/cirkonio ir silicio organinius junginius, tinkamus fotopolimerizacijai.
2. Įvertinti susintetintų medžiagų tinkamumą fotopolimerizacijai naudojant femtosekundinius lazerius bei ištirti skirtingų parametrų ir medžiagų sudėties įtaką pagamintų 3D struktūrų kokybei.
3. Ištirti pirolizės/kalcinavimo parametrų, tokių kaip temperatūra, kaitinimo trukmė ir atmosfera, poveikį gaunamų keraminių 3D mikro/nanoobjektų deformacijai, susitraukimui, cheminėms, fizinėms ir mechaninėms savybėms.

Darbo naujumas

Šioje disertacijoje pademonstruoti didelės raiškos ir kietų 3D keraminių struktūrų gamybos būdai, apimantys naujų medžiagų sintezes, jų pritaikymą 3D daugiafotoninėje litografijoje ir struktūrų kristalinių fazių pokyčius po terminio apdirbimo. Pirmą kartą pademonstruotas tiesioginis 3D mikrostruktūrų kristalinės fazės matavimo metodas, bei pasiektas raiškos rekordas. Keraminės $\text{SiO}_2/\text{ZrO}_2$ periodinės 3D struktūros linijos plotis buvo mažesnis nei 60 nm. Taip pat buvo sukurta nauja unikaliomis mechaninėmis savybėmis pasižyminti silicio-organinė medžiaga. Pritaikius šią medžiagą 3D litografijoje ir atlikus gautų struktūrų pirolizę, buvo nustatyta, kad susiformuoja amorfinė SiOC arba

kristalinės SiC ir/arba α, β -Si₃N₄ struktūros, kurios nesideformuoja ir neturi jokių defektų, o kietumas ir tamprumo modulis yra net ≈ 15 GPa ir ≈ 105 GPa.

Šie pasiekimai išsprendė kietų ir preciziškų 3D struktūrų gamybos iššūkius ir praplėtė technologijos pritaikymo galimybes komercijoje.

Ginamieji teiginiai

1. Zolių-gelių metodas yra tinkamas sintezės būdas gaminti skaidrius silicio ir cirkonio metalo organinius junginius, skirtus lazerinei 3D litografijai. Keičiant pradinių medžiagų (3-metakriloksipropiltrimetoksisilanas ir cirkonio propoksidas) molinį santykį nuo 9:1 iki 5:5 galima efektyviai kontroliuoti medžiagų savybes.
2. 3D keraminių objektų skiriamoji geba priklauso nuo pradinės fotoaktyvios medžiagos sudėties, lazerio parametrų fotopolimerizacijos metu ir kaitinimo protokolo. Naudojant 9:1 molinio santykio 3-metakriloksipropiltrimetoksisilano ir cirkonio propoksido medžiagą, naudojant 300 fs impulsų trukmę, 200 kHz pasikartojimo dažnį, pasirinkus 200 $\mu\text{m/s}$ fotopolimerizacijos greitį ir 64 μW lazerio galią (apšvita 0.22 TW/cm²) bei atkaitinus 3D objektus 1000 °C laipsnių temperatūroje oro atmosferoje galima pasiekti iki 60 nm keraminės struktūros raišką.
3. Miltelių ir 3D objektų, turinčių identišką sudėtį, kristalinės fazės pasižymi struktūriniais skirtumais. Keičiant pradinių pirmtakų 3-metakriloksipropiltrimetoksisilano ir cirkonio propoksido molinius santykius nuo 9:1 iki 5:5 ir kaitinimo temperatūrą nuo 1000 °C iki 1400 °C gaunamos skirtingos 3D objektų ir miltelių kristalinės fazės.
4. Zolių-gelių sintezės metodu galima sintetinti stabilias ir skaidrias silicio organines medžiagas, tinkamas 3D lazerinei litografijai. Galima kontroliuoti silicio organinių medžiagų savybes keičiant pradinių reagentų trimetoksimetilsilano ir 3-metakril-oksipropiltrimetoksisilano molinius santykius (9:1, 8:2 ir 7:3).
5. Keraminių 3D objektų mechaninės savybės priklauso nuo cheminės pradinių medžiagų sudėties ir kaitinimo protokolo. Fotopolimerizacijoje naudojant 8:2 (trimetoksimetilsilanas : 3-metakril-oksipropiltrimetoksisilanas) pradinę medžiagą ir atkaitinus pagamintą objektą 1200 °C temperatūroje azoto atmosferoje, galima gauti itin kietus 3D keraminius

objektus (kietumas iki ≈ 15 GPA, tamprumo modulis iki ≈ 105 GPa).

Rezultatų apžvalga

Disertacija yra paremta knygos skyriumi ir trimis moksliniais straipsniais, išleistais užsienyje leidžiamuosiuose periodiniuose mokslo leidiniuose, turinčiuose cituojamumo rodiklį *Claritive* duomenų bazėje *Web of Science* bei Lietuvoje registruota patentine paraiška.

Pirmojoje disertacijos tyrimų dalyje pademonstruota metalorganinių silicio ir cirkonio junginių sintezė, jų pritaikymas lazerinėje fotopolimerizacijoje, gautų struktūrų kalcinacija ir fizikinių bei cheminių savybių tyrimai. SiX:ZrY metalorganinių foto aktyvių medžiagų serija buvo pagaminta zolių-gelių metodu, varijuojant silicio ir cirkonio pirmtakų molinius santykius (nuo 9:1 iki 5:5).

Visų pirma nustatyta visų junginių zolių ir gelių lūžio rodiklių (angl. RI) priklausomybė nuo bangos ilgio. Rezultatai parodė, kad RI didėja didinant cirkonio kiekį medžiagose ir matavimus atliekant mažesniuose bangos ilgiuose. RI vertės varijuoja nuo 1,422 iki 1,448 zoliuose ir nuo 1,487 iki 1,550 geliuose. Visų gelių, išskyrus Si9:Zr1, RI vertės didesnės nei 1,5, todėl tokios medžiagos gali būti priskirtos didelio lūžio rodiklio polimerams (angl. HRIP), o tai lemia galimą jų pritaikomumą įvairiose srityse.

Furjė transformacijos infraraudonųjų spindulių (angl. FTIR) spektroskopijos analizė atlikta norint įvertinti silicio ir cirkonio metalorganinių junginių cheminės sudėties pokyčius zoliuose, geliuose ir polimeruose. Gauti rezultatai ir charakteringos sugerties smailės leido kokybiškai nustatyti hidrolizės, kondensacijos ir polimerizacijos procesus medžiagose. Zolių spektruose dominuoja plačios -OH grupių sugerties juostos ties $\approx 3330 \text{ cm}^{-1}$ bangos ilgiais, patvirtinančios gausų tirpiklių ir metalorganinių hidroksidų kiekį medžiagose. Geliuose Si-O-Si, Si-O-Zr ir Zr-O-Zr ryšių charakteringos sugerties juostos tampa platesnės ir sudėtingesnės, reiškiančios siloksanų ir cirkoksanų grandinių padidėjusį šakotumą ir ilgumą, o tai patvirtina įvykusią kondensaciją. Gelius paveikus 140 °C temperatūra, pastebėtas žymus dvigubų ryšių tarp anglies atomų sugerties smailių intensyvumo sumažėjimas. Šis sumažėjimas patvirtina vykstančią terminę junginių polimerizaciją.

Atlikus SiX:ZrY medžiagų termogravimetrinę analizę nustatyta, kad visa organinė dalis medžiagose pilnai suskyla pasiekus 700 °C temperatūrą. Taip pat pastebėta, kad didėjant silicio kiekiui junginiuose, masės netektis didėja ir varijuoja nuo 51% iki 62%. Palyginus medžiagų masės netektį ir mikro kubų, pagamintų iš skirtingų SiX:ZrY medžiagų, tūrių susitraukimą po atkaitinimo 1000 °C temperatūroje, bei padarius prielaidą, kad susiformuoja kristobalitas ir tetragoninis cirkonio dioksidas, galima teigti, kad tankesnės mikro struktūros gaunamos, kai yra gaminamos iš medžiagų, turinčių didesnę silicio kiekį.

Siekiant nustatyti pagamintų mišinių fabrikavimo galimybes, keičiant lazerio galią ir fabrikavimo greitį, buvo pagamintos periodinės rastrinės struktūros,

kurios vėliau atkaitintos 1000 °C temperatūroje ore. Buvo nustatyta, kad didžiausia skiriamoji geba yra gaunama naudojant Si9:Zr1 medžiagą, pasirinkus 64 μW lazerio galią ir 200 μm/s fabrikavimo greitį. Po atkaitinimo tokios struktūros linijos plotis siekia 58,7 ± 1,5 nm ir tai yra didžiausia iki šiol pademonstruota laisvos formos 3D neorganinės struktūros raiška.

Pasinaudojus monokristalo Rentgeno difraktometru pirmą kartą tiesiogiai įvertintos 3D mikrostruktūrų kristalinės fazės. Iš SiX:ZrY serijos medžiagų lazeriu sufabrikuotos 3D skeletinės mikrostruktūros, kurios vėliau atkaitintos 1000-1400 °C temperatūrose ore. Visų struktūrų Rentgeno difraktogramos buvo palygintos su atitinkamų medžiagų miltelių difraktogramomis ir įvertinti susidariusių kristalinių fazių panašumai bei skirtumai. Po atkaitinimo 1000 °C temperatūroje visuose mėginiuose susiformuoja kristalinės kristobalito (COD 96-900-8226) ir tetragoninio cirkonio dioksido (COD 96-152-5706) fazės. Keliant temperatūrą, galima stebėti, kaip mažėja amorfinių medžiagų kiekis mėginiuose, o kristalinių fazių smailių intensyvumai didėja. Po atkaitinimo 1400 °C temperatūroje susiformuoja kristalinė ZrSiO₄ (COD 96-900-0692) fazė Si9:Zr1 mikrostruktūroje bei Si7:Zr3 ir Si6:Zr4 medžiagų milteliuose. Taip pat atsiranda monoklininė cirkonio dioksido (COD 96-230-0204) fazė Si5:Zr5 miltelių medžiagoje ir visų medžiagų struktūrose. Įdomu tai, kad visos struktūros išlaikė savo formą net po 1400 °C atkaitinimo, išskyrus struktūrą, pagamintą iš Si9:Zr1 medžiagos, kuri jau po poveikio 1200 °C temperatūra pradėjo lydėtis.

Atlikus atsparumo tyrimus buvo nustatyta, kad keraminės/kristalinės struktūros yra kur kas atsparesnės agresyviems chemikalams, nei polimerinės ir atlaiko didelius temperatūrinius šokus (nuo -200 °C iki 1400 °C).

Antroje disertacijos tyrimų dalyje pademonstruota naujų silicio-organinių junginių sintezė, jų pritaikymas lazerinėje fotopolimerizacijoje, gautų struktūrų pirolizė ir fizikinių bei cheminių savybių tyrimai. Zolių-gelių metodu buvo pagaminta silicio-organinių fotoaktyvių junginių serija, varijuojant trimetoksimetolsilano (angl. MTMS) ir 3-(trimetoksi)propil metakrilato (angl. MAPTMS) prekursorių molinius santykius (nuo 9:1 iki 7:3).

Atlikus medžiagų zolių, gelių ir polimerų lūžio rodiklių (RI) priklausomybių nuo bangos ilgio matavimus nustatyta, kad didėjant komponento MTMS kiekiui, RI didėja ir varijuoja tarp: 1,371 - 1,390, 1,428 - 1,454 ir 1,431 - 1,456 zoliuose, geliuose ir polimeruose regimajame bangų ilgių ruože.

Susintetinta MTMS:MAPTMS mėginių serija yra nauja, todėl norint išsiaiškinti šių medžiagų cheminės struktūros pokyčius zoliuose, geliuose, polimeruose ir keraminuose mėginiuose buvo atlikta FTIR analizė. Nustatyta, kad po hidrolizės medžiagose gausu hidroksi grupių turinčių tirpiklių. Medžiagas pakaitinus 50 °C laipsnių temperatūroje 7 valandas, Si-O-Si charakteringų sugerties smailių intensyvumas padidėjo, o tai patvirtina kondensacinių ryšių susidarymą. Vis dėlto dvigubų ryšių tarp anglies atomų smailės intensyvumas

po poveikio UV diodu nepakito, todėl galime daryti išvadą, kad UV diodo energijos nepakanka tokių medžiagų fotopolimerizacijai. Didžiausi pokyčiai ivyko medžiagų FTIR spektruose po pirolizės 1000 °C temperatūroje azoto atmosferoje. Pirolizuotų medžiagų FTIR spektruose matyti trys neorganiniams ryšiams būdingos sugerties smailės, patvirtinančios SiO_xC_y keramikos sudarymą (800 cm^{-1} priskiriama Si-C; $\approx 440 \text{ cm}^{-1}$ ir $\approx 1010 \text{ cm}^{-1}$ priskiriami vibraciniams ir tempiamiesiems Si-O-Si ryšiams).

Atlikus termogravimetrinę analizę buvo nustatyta, kad MTMS:MAPTMS polimeriniai mėginiai yra visiškai stabilūs iki 150 °C temperatūros, o ryškiausia masės netektis yra tarp 350 ir 600 °C. Šis procesas yra priskiriamas organinių medžiagų skilimui. Temperatūrų intervale tarp 650 ir 950 °C formuojasi amorfinė SiO_xC_y keramika. Taip pat buvo nustatyta, kad didėjant MTMS komponento kiekiui, masės netektis mažėja. Termogravimetrinė analizė parodė, kad yra būtina atlikti hidrolizę ir kondensaciją medžiagų sintezėje, kitu atveju atliekant pirolizę prekursoriai beveik visiškai suskiltų nepasiekę 300 °C temperatūros.

Rentgeno spindulių difrakcinė analizė parodė, kad visi bandiniai, atkaitinti iki 1300 °C temperatūros inertinėje atmosferoje ar vakuume yra amorfiniai. Atkaitinus MTMS:MAPTMS mėginius 1400 °C temperatūroje vakuume, gaunama visiškai gryna SiC (COD 96-154-1662) kristalinė fazė. Taip pat atkaitinus MTMS:MAPTMS mėginius 1500 °C temperatūroje azoto atmosferoje, susiformuoja alpha ir beta Si_3N_4 kristalinių fazių mišinys (COD 96-100-1239 ir COD 96-100-1245).

3D lazerinei fotopolimerizacijai buvo pasirinkta MTMS 8:2 MAPTMS medžiaga. Nustačius optimaliausius fotopolimerizacijos lazeriu parametrus buvo pagaminti 3D mikro giroidai ir fullereno tipo 3D mikro struktūros su mažesne fullereno tipo struktūra viduje. Visi dariniai buvo atkaitinti 1000-1500 °C temperatūroje azoto atmosferoje. Skenuojančiu elektroniniu mikroskopu įvertinus struktūrų paviršiaus kokybę, buvo nustatyta, kad mikro giroidai išlaiko savo formą visame temperatūrų intervale, net pasiekus Si_3N_4 kristalinę fazę. Vis dėlto nuo 1200 °C temperatūros paviršiuje matomi įtrūkimai. Fullerenų tipo struktūros savo formą išlaikė ir neturėjo jokių defektų net iki 1400 °C temperatūros, o aukštesnėje temperatūroje pradėjo skilinėti ir lydėtis.

Pastebėjus, jog atkaitintos struktūros pasižymi itin dideliu tvirtumu, buvo įvertintos jų mechaninės savybės, tokios kaip: Berkovičiaus kietumas ir tamprumo modulis. Didžiausias kietumas ($14,33 \pm 1,17 \text{ GPa}$) ir tamprumo modulis ($104,99 \pm 1,81 \text{ GPa}$) buvo keraminio disko, pagaminto iš MTMS 8:2 MAPTMS medžiagos ir atkaitinto 1200 °C temperatūroje, azoto atmosferoje. Beveik visos medžiagos pasižymėjo puikiomis mechaninėmis savybėmis, kurių vertės didesnės už lydyto kvarco vertes.

Didėjant atkaitinimo temperatūrai struktūrų, pagamintų iš MTMS:MAPTMS, traukiamasis didėja. Taip pat esant didesniam MTMS kiekiui medžiagoje, struktūros traukiasi mažiausiai. Didžiausias linijinis susitraukimas buvo

pasiektas disko, pagaminto iš MTMS 7:3 MAPTMS medžiagos ir atkaitinto 1500 °C temperatūroje azote ir siekė 25,50%. Atlikus diskų tankių matavimus, buvo nustatyta, kad didėjant atkaitinimo temperatūrai, medžiagų tankis didėja. Tankiausias diskas yra pagamintas iš MTMS 9:1 MAPTMS medžiagos ir atkaitintas 1500 °C temperatūroje azote ir yra 2,33 g/cm³. Toks mažas keramikos tankis praplečia šių medžiagų panaudojimo galimybes technologijose, kuriose yra reikalingos lengvos keraminės struktūros.

Pastaruoju metu mikro-optikos srityje didėja poreikis kombinuoti skaidrių ir neperšviečiamų struktūrų gamybą. Skaidri medžiaga naudojama lešių gamyboje, o neskaidri- apertūroms, kurios padidina kontrastą ir mikro-lęšių efektyvumą. Pagamintų silicio-organinių MTMS 8:2 MAPTMS diskų regimojo spektro šviesos pralaidumas siekė net iki 70,6%, kai atitinkami neorganiniai diskai pasižymėjo visiškai regimojo spektro sugertimi. Todėl toks gamybos būdas gali būti naudojamas gaminant mechaniškai atsparią mikrooptiką.

Išvados

1. Zolių- gelių sintezės metodas yra tinkamas būdas gaminti skaidrius metalų organinius (3-metakril-oksipropiltrimetoksisilanas ir cirkonio propoksidą nuo 9:1 iki 5:5) ir silicio organinius (trimetoksimetilsilanas ir 3-metakriloksipropiltrimetoksisilanas nuo 9:1 iki 7:3) junginius, skirtus lazerinei 3D fotopolimerizacijai.
2. Neorganinių 3D struktūrų skiriamoji geba priklauso nuo pradinės fotoaktyvios medžiagos sudėties (3-metakriloksipropiltrimetoksisilanas ir cirkonio propoksidą nuo 9:1 iki 5:5), lazerio parametrų fotopolimerizacijos metu (gamybos greičiai $200 \mu\text{m/s}$ ir $500 \mu\text{m/s}$, galios $48 \mu\text{W}$, $56 \mu\text{W}$, $64 \mu\text{W}$) ir kaitinimo protokolo. Pasirinkus 9:1 (3-metakriloksipropiltrimetoksisilanas : cirkonio propoksidą) medžiagą, $200 \mu\text{m/s}$ gamybos greitį ir $64 \mu\text{W}$ lazerio galią galima gauti iki 60 nm keraminio objekto raišką.
3. 3D objektų ir atitinkamos sudėties miltelių kristalinės fazės pasižymi struktūriniais skirtumais keičiant pradinių medžiagų (3-metakriloksipropiltrimetoksisilanas ir cirkonio propoksidą) sudėtį nuo 9:5 iki 5:5 ir kaitinimo protokolą nuo 1000°C iki 1400°C temperatūros ore. ZrSiO_4 (COD 96-900-0692) kristalinė fazė buvo gauta 9:1 3D objektui ir 7:3, 6:4 milteliams, atkaitintiems 1400°C temperatūroje ore.
4. Neorganinių 3D objektų mechaninės savybės priklauso nuo pradinės fotoaktyvios medžiagos sudėties (trimetoksimetilsilanas ir 3-metakriloksipropiltrimetoksisilanas nuo 9:1 iki 7:3) ir kaitinimo protokolo (nuo 1000°C iki 1500°C) temperatūros azoto atmosferoje. Galima gauti už lydytą kvarcą kietesnius 3D neorganinius objektus. Naudojant 8:2 (trimetoksimetilsilanas : 3-metakril-oksipropiltrimetoksisilanas) medžiagą buvo gautas net $14,33 \pm 1,77 \text{ GPa}$ Berkovičiaus kietumas ir $104,99 \pm 1,81 \text{ GPa}$ tamprumo modulis.
5. Susintetinta 8:2 (trimetoksimetilsilanas : 3-metakriloksipropiltrimetoksisilanas) medžiaga yra tinkama mikro-optikos gamyboje dėl polimerinės medžiagos pralaidumo (iki 70,6%) regimajai šviesai (nuo $\approx 350 \text{ nm}$ iki 700 nm) (optinui elementui gaminti) ir nepralaidžių keraminių struktūrų (apertūroms).

PADEKA

Visų pirma dėkoju doktorantūros vadovui prof. dr. Simui Šakirzanovui. Ačiū už pasitikėjimą ir suteiktą galimybę studijuoti doktorantūrą, už neįkainojamos patirties ir žinių perdavimą bei galimybę mokytis iš Jūsų. Ačiū, kad visada galėjau kreiptis pagalbos, Jūs padėjot įgyvendinti tikslus ir įveikti visus iškilusius iššūkius. Jūsų pamokos, konstruktyvios išvalgos ir patarimai padėjo man tapti tuo, kuo esu dabar. Labai tai vertinu.

Ačiū moksliniam konsultantui prof. dr. Mangirdui Malinauskui už konstruktyvias diskusijas tyrinėjant lazerių pasaulį, už motyvaciją siekti daugiau ir pavyzdį, kaip reikia degti aistra mokslui.

Ačiū prof. dr. Artūriui Katelnikovui už vadovavimą bakalauro ir magistro studijų metu. Jūs supažindinot su įdomiu moksliniu pasauliu. Ačiū už pirmąsias vertingas pamokas ir perduotas žinias.

Ačiū dr. Dariui Gailevičiui ypatingai už gyvenimiškus patarimus, pasidalintą išmintį ir mokslines pamokas. Tavo entuziazmas mokslui įkvepia.

Ačiū Chemijos ir geomokslų fakulteto dėstytojams ir administracijai už žinias, patirtis ir pagalbą.

Ačiū Fentikos kolektyvui už galimybes tobulėti.

Dėkoju kolegoms, bendraautoriams ir draugams: Nadeždai, Artūriui, Lukui, Rokui, Eglei, dr. Julijai, dr. Vaidui, dr. Matui, dr. Andriui, dr. Mindaugui, dr. Linui. Jūsų dėka laikas doktorantūroje buvo ne tik įdomus, bet ir linksmas.

Ačiū tėvams, Vilmai ir Vitui, bei broliui Ryčiui ir jo šeimai už padrašinimą, rūpestį ir palaikymą studijų metu. Didžiausias ačiū Žilvinui už kantrybę, meilę ir buvimą šalia visą šį laikotarpį.

"You are going to meet people who will change your life forever. Some will be there for years, a few for a lifetime, and many for what seems like just a moment. But everyone changes you in some way. They are all pieces of who you are and who you will become."

CURRICULUM VITAE

Personal information	
Name, Surname	Greta Merkininkaitė
Date and place of birth	1993/12/30, Lithuania
E-mail addresses	greta.merkininkaite@chgf.vu.lt, greta.merkininkaite@femtika.com, greta.merkininkaite@gmail.com

Education	
2018 – 2022	PhD studies in Materials Engineering, Faculty of Chemistry and Geosciences, Vilnius University.
2016 – 2018	Master of Science in Chemistry of Nanomaterials, Faculty of Chemistry and Geosciences, Vilnius University.
2012 – 2016	Bachelor of Science in Nanotechnology and Materials, Faculty of Chemistry, Vilnius University.

Continued on next page

Work experience	
MAR 2023 – present	Engineer, Computer Process Control, Ltd.
SEP 2022 – present	Junior Assistant, Faculty of Chemistry and Geosciences, Vilnius University.
OCT 2018 – present	Researcher, Femtika Ltd.
OCT 2019 – JAN 2020	Professional Internship at FORTH, Institute of Electronic Structure and Lasers- IELS, Heraklion, Crete, Greece. Dr. M. Farsari laboratory.
JUN 2017 – OCT 2018	Technologist, Optonas Ltd.
JUN 2016 – JUN 2017	Chemist, Labtarna Ltd.
SEP 2015 – NOV 2015	Professional Practice at the Laboratory of Experimental Nuclear Physics, Department of Nuclear Research, Center for Physical Sciences and Technology.
JUL 2014 – AUG 2014	Students Scientific Practice at Faculty of Chemistry, Vilnius University.

NOTES

NOTES

NOTES

Vilnius University Press
9 Saulėtekio Ave., Building III, LT-10222 Vilnius
Email: info@leidykla.vu.lt
www.leidykla.vu.lt
bookshop.vu.lt, journals.vu.lt
Print run copies 35.